uOttawa

L'Université canadienne
Canada's university

FACULTÉ DES ÉTUDES SUPÉRIEURES ET POSTOCTORALES

uOttawa

L'Université canadienne
Canada's university

FACULTY OF GRADUATE AND POSDOCTORAL STUDIES

Howard Rideout

AUTEUR DE LA THÈSE / AUTHOR OF THESIS

M.A.Sc. (Electrical Engineering)

GRADE / DEGREE

School of Information Technology and Engineering

FACULTÉ, ÉCOLE, DÉPARTEMENT / FACULTY, SCHOOL, DEPARTMENT

A True-time Delay Beamforming System Incorporating a Wavelength Tunable Optical Phase-Lock Loop

TITRE DE LA THÈSE / TITLE OF THESIS

J. Yao

DIRECTEUR (DIRECTRICE) DE LA THÈSE / THESIS SUPERVISOR

CO-DIRECTEUR (CO-DIRECTRICE) DE LA THÈSE / THESIS CO-SUPERVISOR

EXAMINATEURS (EXAMINATRICES) DE LA THÈSE / THESIS EXAMINERS

T. Hall

L. Roy

Gary W. Slater

Le Doyen de la Faculté des études supérieures et postdoctorales / Dean of the Faculty of Graduate and Postdoctoral Studies

A True-Time Delay Beamforming System Incorporating a Wavelength Tunable Optical Phase-Lock Loop

Howard Rideout

Thesis submitted to the
Faculty of Graduate and Postdoctoral Studies
in partial fulfillment of the requirements
for the degree of

Master of Applied Science in Electrical Engineering

School of Information Technology and Engineering
Faculty of Engineering
University of Ottawa

September 2006

Library and Archives Canada

Published Heritage Branch

395 Wellington Street
Ottawa ON K1A 0N4
Canada

Bibliothèque et Archives Canada

Direction du Patrimoine de l'édition

395, rue Wellington
Ottawa ON K1A 0N4
Canada

Your file Votre référence
ISBN: 978-0-494-34104-9
Our file Notre référence
ISBN: 978-0-494-34104-9

NOTICE:
The author has granted a non-exclusive license allowing Library and Archives Canada to reproduce, publish, archive, preserve, conserve, communicate to the public by telecommunication or on the Internet, loan, distribute and sell theses worldwide, for commercial or non-commercial purposes, in microform, paper, electronic and/or any other formats.

The author retains copyright ownership and moral rights in this thesis. Neither the thesis nor substantial extracts from it may be printed or otherwise reproduced without the author's permission.

AVIS:
L'auteur a accordé une licence non exclusive permettant à la Bibliothèque et Archives Canada de reproduire, publier, archiver, sauvegarder, conserver, transmettre au public par télécommunication ou par l'Internet, prêter, distribuer et vendre des thèses partout dans le monde, à des fins commerciales ou autres, sur support microforme, papier, électronique et/ou autres formats.

L'auteur conserve la propriété du droit d'auteur et des droits moraux qui protège cette thèse. Ni la thèse ni des extraits substantiels de celle-ci ne doivent être imprimés ou autrement reproduits sans son autorisation.

In compliance with the Canadian Privacy Act some supporting forms may have been removed from this thesis.

While these forms may be included in the document page count, their removal does not represent any loss of content from the thesis.

Conformément à la loi canadienne sur la protection de la vie privée, quelques formulaires secondaires ont été enlevés de cette thèse.

Bien que ces formulaires aient inclus dans la pagination, il n'y aura aucun contenu manquant.

Canada

© Howard Rideout, Ottawa, Canada, 2007

ABSTRACT

This thesis presents the study of a frequency-discriminator-aided optical phase-lock loop (OPLL) and its application to a fiber-Bragg-grating-based true-time delay (TTD) module for the purpose of phased-array antenna (PAA) beamforming. The TTD module uses uniform fiber Bragg gratings (FBGs) to form the delay lines of an FBG prism. The wavelengths from two external cavity laser diodes are phase-locked by the OPLL and applied to the FBG prism to achieve tunable time delays.

The performance of the system is evaluated using a time-delay measurement experiment. The experimental time delays generated are compared with the theoretically designed values and are found to be in close agreement. Simulations of the radiation patterns generated from the measured time delays are found to closely match the steering angle designed for the system. To the best of our knowledge, this is the first time an OPLL has been used in conjunction with an FBG-based TTD beamforming module.

ACKNOWLEDGEMENT

I would like to thank my supervisor, Dr. Jianping Yao, for his support throughout this research project. I thank him for his helpful discussion and direction during my research.

I would like to recognize the Natural Sciences and Engineering Research Council of Canada (NSERC) for helping fund this work through the Canada Graduate Scholarship (Master's).

This research has also been carried out in collaboration with the Communications Research Centre (CRC). I am very thankful for the help of Mr. Joe Seregelyi whose expertise and discussion helped greatly in the completion of this work. I would also like to thank John Oldham and Dave Barlow, also from CRC, who were invaluable in carrying out the practical components of this project.

I would also like to extend appreciation to the following people who have supported me with numerous discussions and brainstorming sessions: Mr. Fei Zeng, Mr. Wang Qing and, especially, Mr. Sebastien Blais.

I would like to thank my family who has always encouraged me in any goal I have ever pursued. Finally, I want to thank the person who is always there for me, Nancy. She is the one who has put up with all the long hours and even relocating to a new city. Without her support and encouragement this would have been a much more difficult process.

TABLE OF CONTENTS

LIST OF FIGURES

LIST OF TABLES

LIST OF ACRONYMS

AF	Array Factor
CRC	Communications Research Centre
ECL	External Cavity Laser
FBG	Fiber Bragg Grating
IM	Intensity Modulation
IM-DD	Intensity Modulation – Direct Detection
MZM	Mach-Zehnder Modulator
OIL	Optical Injection Locking
OIPLL	Optical Injection Phase-Lock Loop
OPLL	Optical Phase-Lock Loop
OSA	Optical Spectrum Analyzer
PAA	Phased-Array Antenna
PD	Photodetector
PLL	Phase-Lock Loop
RF	Radio Frequency
RHD	Remote Heterodyne Detection
RoF	Radio-over-Fiber
SA	Spectrum Analyzer
TCA	Transconductance Amplifier
TEC	Thermoelectric Cooler
TMM	Transfer Matrix Method

TTD	True-Time Delay
UV	Ultraviolet
VCO	Voltage-Controlled Oscillator

LIST OF PUBLICATIONS

1. H. R. Rideout, J. S. Seregelyi, and J. P. Yao, "A true-time delay beamforming system incorporating a wavelength tunable optical phase-lock loop," *IEEE J. Lightwave Technol.*, submitted for publication, Sept. 2006.
2. H. R. Rideout, J. S. Seregelyi, S. Paquet, and J. P. Yao, "Discriminator-aided optical phase-lock loop incorporating a frequency down-conversion module," *IEEE Photon. Technol. Lett.*, vol. 18, no. 22, pp. 2344-2346, Nov. 2006.
3. Q. Wang, H. Rideout, F. Zeng, and J. P. Yao, "Millimeter-wave frequency tripling based on four-wave mixing in a semiconductor optical amplifier," *IEEE Photon. Technol, Lett.*, vol. 18, no. 23, pp. 2460-2462, Dec. 2006.
4. H. Rideout, J. Seregelyi, and J. P. Yao, "Wavelength tunable phase-locked laser diodes for true-time delay beamforming," Oral presentation at Photonics North 2006, Quebec City, Canada, *Proc. of SPIE*, vol. 6343, 63432D (2006).

Chapter 1

INTRODUCTION

1.1 Background

Photonic true-time delay (TTD) beamforming has been extensively investigated as a promising technique for wideband phased-array antenna (PAA) systems [1]-[11]. High performance radar and broadband wireless access systems place ever increasing demands on the sensitivity, portability, resolution, bandwidth and degree of angular scan that these antenna systems can achieve [4], [5], [12], [13]. Array antennas are an attractive solution to meet these demands because they offer high directivity, low visibility, beam pointing agility and dynamic beam patterning capabilities [3], [14].

Steering the mainlobe of the radiation pattern of a PAA can be achieved by applying a linear phase shift to the drive signals feeding each antenna element. Since an array antenna is composed of electrical radiating elements, the most intuitive means of phase-shifting the drive signals is to use electrical microwave phase shifters. However, such methods suffer from some notable disadvantages: high loss associated with distributing high-frequency electrical signals, unavoidable cross-coupling of feed signals associated with electrical transmission lines, limited bandwidth and relatively heavy weight [1]. Another important disadvantage of an electrical phase-shifting scheme is the beam-squint problem that corrupts the radiation pattern for broadband operation, leading to significant

signal degradation and broadening of the overall antenna beam. This effect is the result of maintaining a fixed phase shift regardless of the output frequency [1], [6]. Electrical true-time delay techniques based on microwave delay-line systems, that avoid the beam-squint phenomenon, are possible. However, they still suffer from the other disadvantages listed above.

The generation of a linear phase shift can also be done in the optical domain through the use of an optical delay-line arrangement [1]. This solution has the advantage of avoiding the beam-squint problem by making the phase shift proportional to the output frequency. In addition, an optical solution offers other advantages, such as small size, light weight, immunity to electromagnetic interference between optical feed lines, and, perhaps the most important, the low-loss distribution of signals over optical fiber to remote antenna sites [4], [5].

The implementation of a photonics-based module to control PAAs also has difficulties associated with the higher cost involved and the technical challenges of implementation. Due to the relative immaturity of the field of photonic TTD beamforming, fabricating a precise and reliable photonic TTD module is more difficult technologically, leading to higher costs than electrical implementations. As the technology develops, however, the limiting factors of photonic implementation will become less significant and the advantages can be more fully exploited [15].

Many optical architectures have been investigated to generate the required electrical phase shift for PAA beamforming. Early implementations were based on bulk optics [12], [16], [17], however, these systems are highly sensitive to mechanical vibration and temperature change. Another method involves the use of serial or parallel delay lines of varying lengths [7], [13], [18]. However, this type of architecture can lead to high losses and interchannel interference due to cross-coupling within optical switching devices, degrading the performance of the system. A more recent implementation is to use fiber Bragg grating (FBG) delay lines to achieve the required time delays [2], [6], [19]-[23]. Several different FBG configurations are possible, some allowing continuous beam steering [20]-[23] and others allowing only discrete steering angles [2], [6]. The method to be studied here uses discrete, uniform FBG delay lines. On each delay line, FBGs are written at different physical locations with different center wavelengths. By tuning the wavelength applied to the FBG delay lines, the reflection position along the delay lines is changed, varying the time delay of the optical signals, and thus, the phase of the recovered electrical signals at the array elements.

The TTD beamforming system can be fed optically in a variety of ways depending on the architecture. FBG-based approaches are usually fed by a single wavelength optical source that is externally modulated by an RF signal [6]. For some applications, TTD beamforming systems have to operate at higher frequencies, which require expensive high-speed external modulators. In addition, conventional intensity modulation generates a signal with two sidebands plus a carrier, which suffers from chromatic dispersion,

leading to a power penalty. An alternative optical technique for generating this high frequency output is to use optical heterodyning.

Optical heterodyning involves the beating of two wavelengths at a photodetector (PD) producing a microwave output with a frequency determined by the wavelength spacing. This technique offers the advantages of very high frequency generation (limited only by the bandwidth of the PD), large tuning range [24], high output power, and minimization of the chromatic-dispersion-induced power penalty [25].

The major disadvantage of this method is that the two optical wavelengths must be phase correlated in order to generate a microwave output with low phase noise. The individual phase noise of each optical source contributes directly to the phase noise in the generated microwave signal, so some technique must be used to reduce this output phase noise and produce a high-quality microwave signal. One such technique is an optical phase-lock loop (OPLL) that uses an electrical feedback circuit to phase-lock the two laser diodes, to help reduce the phase noise of the beat signal.

This research project investigates a novel approach to achieve tunable time delays using a frequency discriminator-aided OPLL in combination with a uniform FBG-delay line TTD beamforming module.

1.2 Objectives

In an effort to economically increase operating frequency and minimize the chromatic-dispersion-induced power penalty associated with double-sideband modulation, an optical-heterodyne microwave source, for input to a photonic TTD beamforming system, will be developed. The microwave output signal quality will be characterized on the basis of its 3-dB bandwidth and frequency stability.

A TTD delay beamforming module incorporating FBG-based delay lines will be designed and fabricated to the proper specifications relating to spectral width, reflection strength, and FBG spectral spacing. These delay lines will be characterized on the basis of these parameters.

Finally, an experiment will be developed to investigate the accuracy of the time delays generated by applying the optical-heterodyne source to the FBG-based TTD beamforming module.

1.3 Major Contributions

1. An optical-heterodyne source based on a frequency-discriminator-aided optical phase-lock loop is implemented in collaboration with the Microwave Photonics Group at the Communications Research Centre (CRC). A previously developed system is modified by the addition of a frequency down-conversion module, and the frequency discriminator is redesigned to accommodate this modification. The effects of these changes are studied and the source is characterized on the basis of microwave signal quality and frequency stability.

2. A uniform FBG-based TTD beamforming module is designed and fabricated. The module consists of four FBG delay lines. The FBGs are fabricated by the phase mask technique, using a frequency-doubled argon ion laser operating at 244 nm. The fibers are hydrogen-loaded to increase the photosensitivity and tension is applied during the exposure process to control the FBG center wavelength. The delay lines are characterized on the basis of spectral width, reflection strength, and spectral spacing.

3. The discriminator-aided OPLL is applied to the FBG-based TTD module. A time delay measurement setup is devised and the relative time delays, generated from the reflection of the OPLL signal by each delay line FBG, are recorded. These results are compared with the theoretically designed time delays and a simulation of the generated radiation pattern is carried out. To the best of our knowledge, this is the first time an OPLL has been tested in an FBG-based TTD beamforming module.

1.4 Organization

This thesis contains a total of six chapters. Chapter 1 reviews some of the background of photonic TTD techniques and presents the motivations behind using an OPLL as the input to this type of system. The objectives and the major contributions of this research project are also presented.

Chapter 2 discusses the theory associated with PAAs and FBGs, and further details the benefits of using a photonic TTD module as the feed network for a PAA. First, the theoretical model for a linear PAA is presented, beginning with a two-element linear array and extending this to the more general case of an N-element linear array. This chapter also discusses several FBG fabrication techniques and introduces the concept of photosensitivity.

Chapter 3 introduces several techniques for optically generating microwave signals and gives the theoretical derivation of optical heterodyning, along with its advantages. The theoretical operation of an OPLL is presented. The operation of a delay-line frequency discriminator, as part of an OPLL, is also explored and the effects of laser linewidth on the system performance are discussed.

The frequency down-conversion module implementation is presented in Chapter 4, along with an analysis of its contribution to the phase noise of the system. The frequency discriminator redesign and calibration are also outlined and its performance is analyzed.

This chapter also presents the performance achieved by the discriminator-aided OPLL with down-conversion.

Chapter 5 presents the TTD beamforming module. The physical spacing between adjacent FBGS on each individual delay line is calculated, the FBG fabrication is outlined and the optical delay line transmission and reflection spectra are given. Some problems encountered during this process are also presented. Finally, the measured time delays are reported, along with simulations of the generated antenna radiation patterns.

Chapter 6 draws conclusions on the results obtained in the overall project and gives recommendations for future work in this area.

Chapter 2

THEORY OVERVIEW

This chapter looks at the theory associated with PAAs and FBGs, and further describes the benefits of using a photonic TTD module as the feed network for a PAA. Several techniques of FBG fabrication are discussed, along with the concept of photosensitivity.

2.1 Phased Array Antennas

An array antenna is a group of simple antennas linked together in a special electrical or geometrical configuration. These simple antennas, termed the array's elements, can be one of many types including dipole, loop, or microstrip patch antennas. In many applications, such as point-to-point terrestrial links, satellite communications or air-borne radar, there is a need to have a highly focused radiation pattern. Array antennas offer this capability through the control of several of the array's parameters. The number of elements, their geometrical layout, their relative spacing, and their excitation amplitudes and phases can all be adjusted to allow the designer to shape the radiation pattern of the overall array [26]. This allows versatility in the design of antenna arrays since these parameters can be used to control the location of the main radiation lobe, the maximum sidelobe levels and the location of the nulls [27].

The fact that the excitation signal parameters can be used to dynamically control the radiation pattern shape and direction is of particular importance. This property means that, through simple electronic control, the mainlobe of the radiation pattern can be steered without physically moving the antenna. This is the main concept behind phased array antennas (PAAs).

2.1.1 Two-Element Array – Free Space Analysis

Let us first consider the case of a two-element array consisting of two infinitesimal dipoles oriented along the z-axis as shown in Fig. 2.1. To simplify the analysis, it is assumed that there is no coupling between the two elements [26].

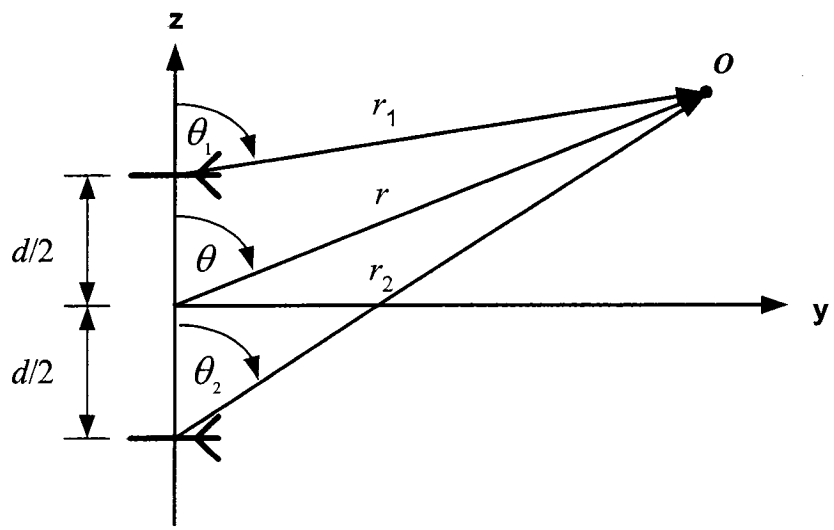

Fig. 2.1. Two-element antenna array.

It can be shown that for an infinitesimal dipole in the far-field, i.e. when $r >> \ell$, the electric field can be expressed as

$$\vec{E} = \left[\frac{j\eta k \mathrm{I} \ell e^{-jkr}}{4\pi r} \right] \vec{E}_0(\theta, \phi) \tag{2.1}$$

where η is the intrinsic impedance of the medium, $k = \frac{2\pi}{\lambda}$ is the wave number, ℓ is the length of the dipole, I is the excitation current, and $\vec{E}_0(\theta, \phi)$ is a direction-dependent factor.

For the two-element array considered in Fig. 2.1, the total electric field in the far-field region is the sum of the two individual array elements. Each element has an excitation current of equal magnitude, I_0, and a relative phase difference of β.

$$\vec{E}_T = \vec{E}_1 + \vec{E}_2 = \frac{j\eta k I_0 \ell}{4\pi} \left[\frac{e^{-j(kr_1 - \beta/2)}}{r_1} \vec{E}_{01}(\theta_1, \phi) + \frac{e^{-j(kr_2 + \beta/2)}}{r_2} \vec{E}_{02}(\theta_2, \phi) \right]. \tag{2.2}$$

At the observation point, O, the vectors from the elements appear virtually parallel. This allows the following approximations to be made:

$$\theta_1 \approx \theta_2 \approx \theta \tag{2.3a}$$

$$r_1 \approx r_2 \approx r \qquad \text{for the amplitude terms} \tag{2.3b}$$

and

$$r_1 \approx r - \frac{d}{2}\cos\theta \tag{2.4a}$$

$$r_2 \approx r + \frac{d}{2}\cos\theta \quad \text{for the phase terms.} \tag{2.4b}$$

Using these approximations, (2.2) becomes

$$\begin{aligned}\vec{E}_T &= \frac{j\eta k I_0 \ell}{4\pi r}\vec{E}_0(\theta,\phi)\left[e^{-j(k(r-\frac{d}{2}\cos\theta)-\beta/2)} + e^{-j(k(r+\frac{d}{2}\cos\theta)+\beta/2)}\right] \\ &= \frac{j\eta k I_0 \ell e^{-jkr}}{4\pi r}\vec{E}_0(\theta,\phi)\left(2\cos\left(\frac{kd\cos\theta+\beta}{2}\right)\right)\end{aligned} \tag{2.5}$$

Comparing this result to (2.1), it is apparent that the first part of the expression is simply the pattern of a single radiating element and is known as the *element pattern*. The second part of the expression is dependent on the array geometry and is known as the *array factor*. Therefore, the far-field pattern is a product of the individual element pattern and an overall pattern determined by the array of elements:

Array Pattern = (Element Pattern) x (Array Factor).

2.1.2 The *N*-Element Linear Array

The array factor derivation for a two-element linear array can be extended to the more general case of N identical elements. Fig. 2.2 shows a linear array of N uniformly-spaced elements located at positions $(n-1)d$ for $n = 1, 2, 3, \ldots, N$ along the z-axis.

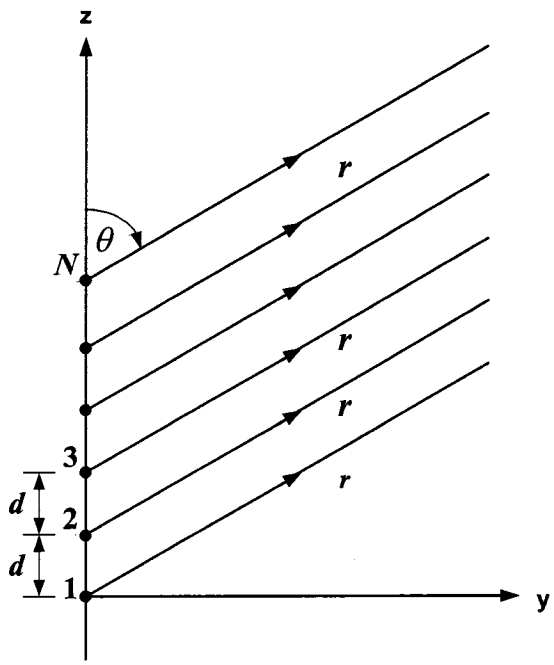

Fig. 2.2. N-element antenna array with uniform spacing.

For a constant spacing of d, and an excitation current of I_n, then, in the far field the contribution of a single element to the total field at the observation point can be written as

$$\vec{E}_n(\theta) = \frac{j\eta k \mathrm{I}_n e^{-jkr_n}}{r_n} \vec{E}_0(\theta,\phi). \tag{2.6}$$

As before, some simplifying assumptions can be made. First, for the amplitude in the far field,

$$r_n \approx r \tag{2.7a}$$

and, secondly, for the phase in the far field,

$$r_n \approx r-(n-1)d\cos\theta\,. \tag{2.7b}$$

Also, assume the elements are driven by currents with equal magnitude and a linear phase progression, $\beta_n = (n-1)\beta$, such that

$$\mathrm{I}_n = I_0 e^{j\beta_n}\,. \tag{2.8}$$

Therefore, using (2.7a), (2.7b), and (2.8) in (2.6), the total field is, again, the summation of the contributions of all the individual elements. This can be expressed as

$$\vec{E}_T(\theta) = \sum_{n=1}^{N} \frac{j\eta k I_0 e^{-jkr}}{r} \vec{E}_0(\theta,\phi) e^{j(n-1)(kd\cos\theta+\beta)} \tag{2.9}$$

Again, this resultant pattern consists of an element pattern multiplied by an array factor. Extracting the array factor (AF) we have

$$AF(\Psi) = \sum_{n=1}^{N} e^{j(n-1)\Psi} \tag{2.10}$$

where Ψ is defined as $\Psi = kd\cos\theta + \beta$.

The right hand side of (2.10) can be seen to be a geometric progression whose first term is one and whose constant ratio is $e^{j\Psi}$. Therefore, the magnitude of the array factor can be shown to be

$$|AF(\Psi)| = \left|\frac{\sin(N\Psi/2)}{\sin(\Psi/2)}\right| \tag{2.11}$$

The maximum value of this expression is N and is obtained when $\Psi = 0$. Therefore, a normalized expression for the array factor can be written as

$$|af(\Psi)| = \frac{|AF(\Psi)|}{|AF(\Psi = 0)|} = \left|\frac{\sin(N\Psi/2)}{N\sin(\Psi/2)}\right| \tag{2.12}$$

By controlling the parameters of the array, the radiation direction of the antenna array can be steered. The array concept may also be extended to the case of planar arrays, where the elements are arranged in some geometric pattern, e.g. rectangular or circular. However, this thesis will focus only on the theory and behaviour of linear array antennas.

2.1.3 Array Radiation Patterns

The normalized array factor for a linear phased array antenna was given in (2.12) where

$$\Psi = kd\cos\theta + \beta. \tag{2.13}$$

Based on these equations, the shape and direction of the main beam of the antenna can be controlled by changing the distance between elements, d, the number of elements in the array, N, or the phase progression, β. The following figures show the effects of changing each of these parameters while the others are held constant.

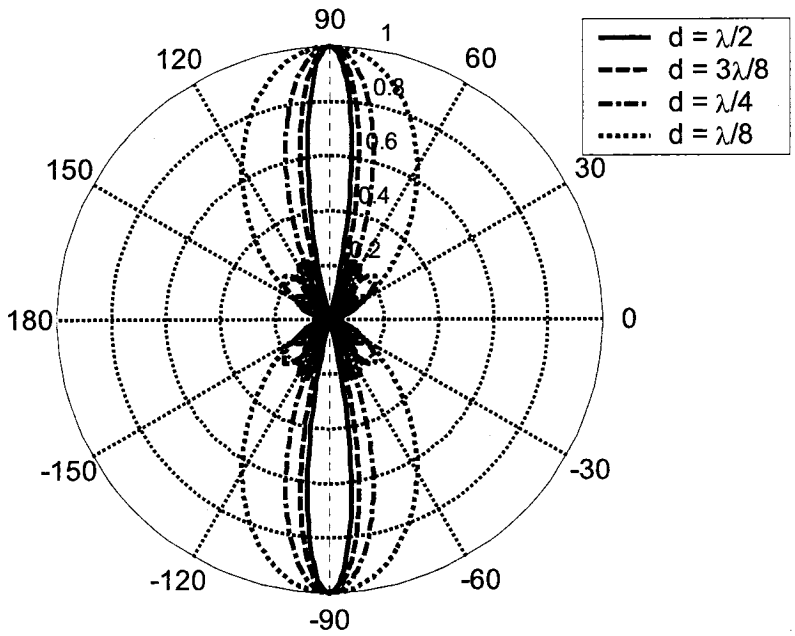

Fig. 2.3. Radiation pattern for various element spacings ($\beta = 0°$, $N = 8$ elements). Shown in the y-z plane.

This illustration shows the effect of changing the element spacing while holding the other parameters constant. Varying the spacing affects the width of the radiation pattern lobes. A wider spacing results in a narrower, more direct beam.

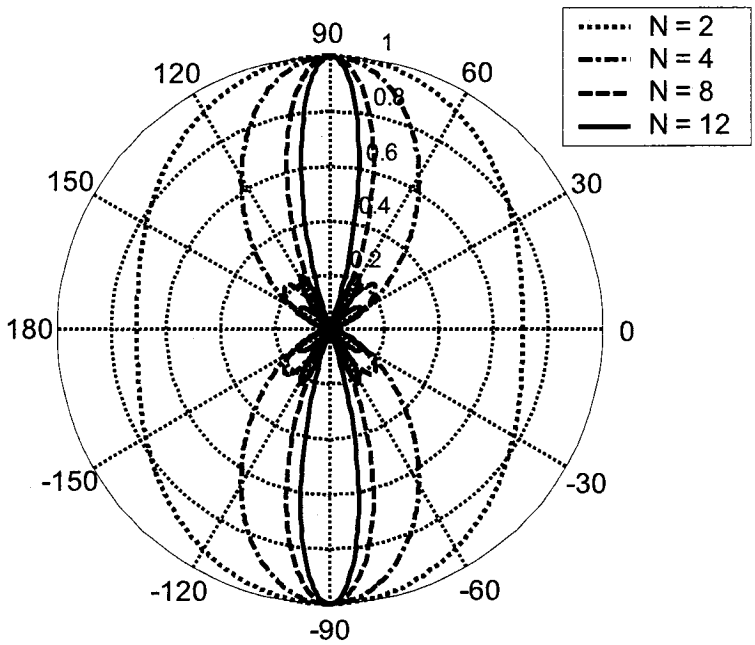

Fig. 2.4. Radiation pattern for different numbers of array elements (β = 0°, d = λ/4). Shown in the y-z plane.

Fig. 2.4 shows the effect of using different numbers of array elements. The number of elements affects the shape of the radiation pattern, including the number of sidelobes present, as well as the width of the main beam.

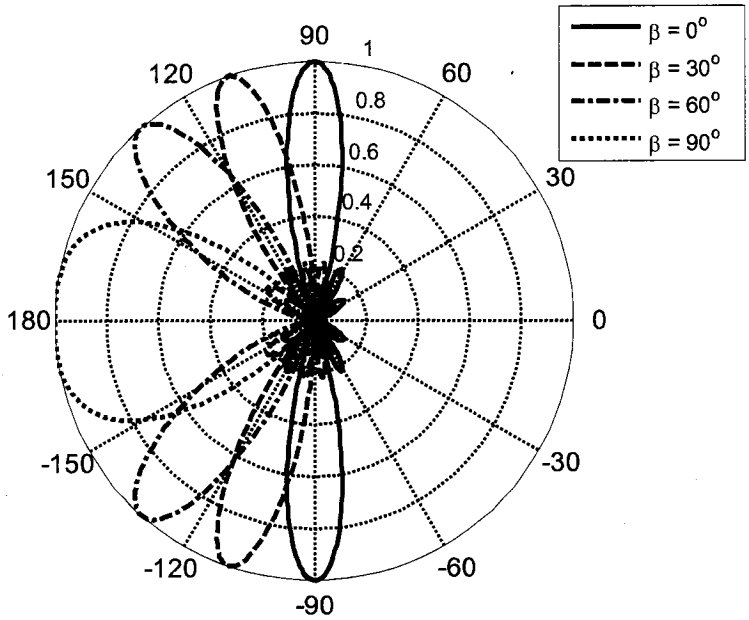

Fig. 2.5. Radiation pattern for different phase progressions (N = 12, d = λ/4). Shown in the y-z plane.

This figure illustrates that the phase progression directly influences the radiation direction of the array. Thus, by varying the phase progression of the feed signal to the array the direction of the radiation pattern can be steered.

2.1.4 The Beam Squint Effect

The most intuitive method of varying the phase progression, β, for a PAA is to use an electrical phase shifter, since an array antenna is composed of electrical radiating elements. However, it is possible for an array antenna system to contain thousands of

antenna elements, with a feed system requiring thousands of phase shifters, connection cables, power splitters, and so on. This would make the system so bulky, heavy, and expensive that it is practically infeasible for many applications [1].

Another important problem arises when we consider wideband PAAs. In many cases it is desirable to tune the output frequency of the array. However, if phase shifters, that provide a constant phase shift from element to element, are used, the beam pointing direction will actually be different for different signal frequencies [1]. This phenomenon is known as "beam squint", and means the steering angle, θ, of the mainlobe of the array pattern will be oriented in different directions for different signal frequencies.

Recall from Section 2.1.3 that the principal maximum of the array factor is obtained when $\Psi = 0$. Therefore, by setting (2.13) equal to zero, the expression for a particular beam pointing direction, θ_0, becomes

$$\theta_0 = \cos^{-1}\left(\frac{\lambda\beta}{2\pi d}\right) \tag{2.14}$$

where the expression for k has been substituted into the equation. The frequency dependent nature of the steering angle becomes evident when we substitute frequency for wavelength in (2.14)

$$\theta_0 = \cos^{-1}\left(\frac{c\beta}{d\,2\pi f}\right) \tag{2.15}$$

where c and f are the propagation velocity and frequency of the signal, respectively.

The following figure illustrates the beam squinting phenomenon for a wideband phased array of 6 elements with a bandwidth of 10 GHz. The center frequency is taken as f_0 = 15 GHz, and the simulation is carried out for a frequency range from 10 to 20 GHz.

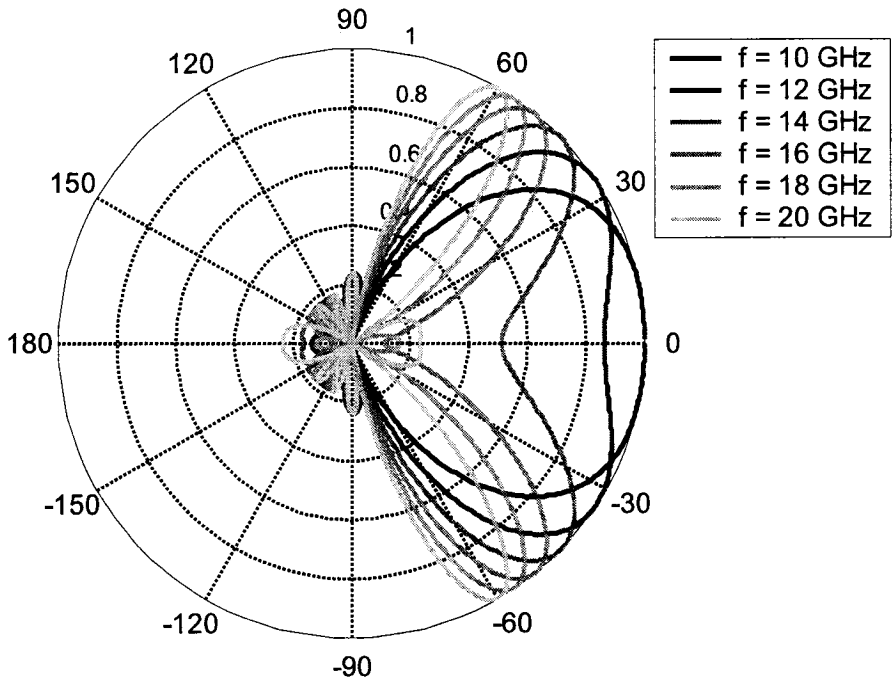

Fig. 2.6. Beam squinting of a PAA operating from 10 - 20 GHz (d = 0.75 cm, N = 6). Shown in the y-z plane.

Fig. 2.6 clearly illustrates that the direction of the radiation pattern varies with the operating frequency. This undesirable effect greatly degrades the performance of the antenna for wideband operation.

(2.15) illustrates that a change in frequency will result in a change in θ_0, however, it also provides the solution to this problem: make the phase-shift proportional to the frequency, i.e. use a time delay rather than a phase shift between individual array elements. This method is known as true-time delay and provides a constant time delay, ΔT, for all frequencies, which translates into a variable phase progression with respect to frequency. This phase shift can be expressed as

$$\beta = 2\pi f \Delta T \tag{2.16}$$

and illustrates that, for a fixed time delay ΔT, the phase progression will change as the frequency is changed.

The following figure shows the simulation of the same phased array example used to illustrate the constant phase shift effect ($N = 6$ elements, $d = 0.75$ cm, $f_0 = 15$ GHz). This time, however, TTD components are used instead of electrical phase shifters. Again, the frequency is varied from 10 - 20 GHz. The TTD elements introduce a time delay progression of ΔT = 16.67 ps which corresponds to the same phase shift of $\frac{\pi}{2}$ at the center frequency of 15 GHz.

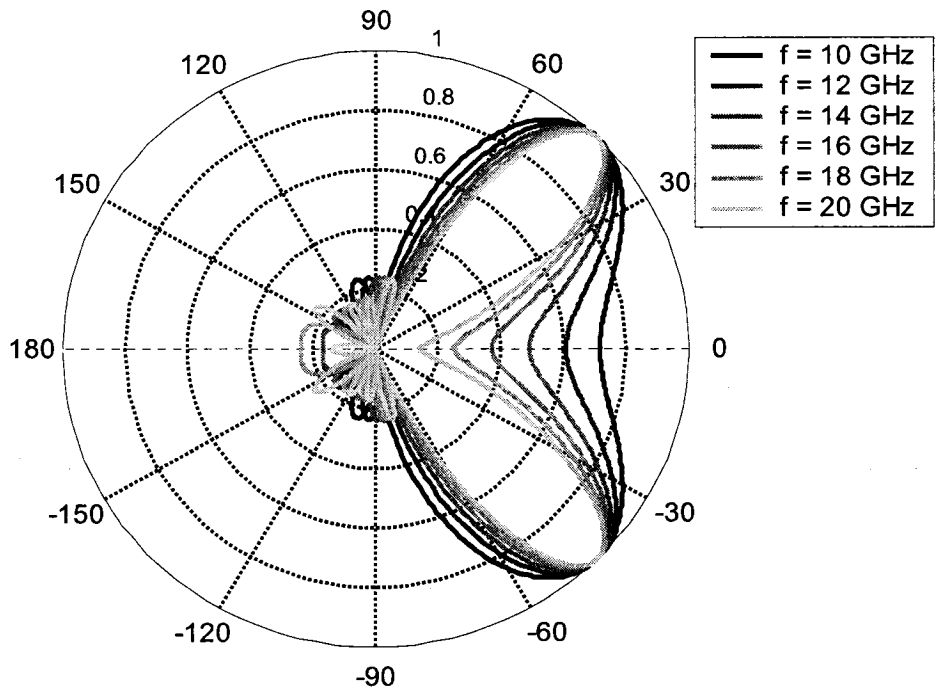

Fig. 2.7. Beam squint-free operation of PAA with TTD operating from 10-20 GHz (N = 6, d = 0.75 cm). Shown in the y-z plane.

Fig. 2.7 clearly shows that the orientation of the antenna pattern does not change with the operating frequency. Thus, TTD can be used to improve the performance of the antenna for wideband operation. The slight variation in shape of the pattern with frequency is due to the relative change in the electrical spacing of the elements as the wavelength changes.

In this arrangement, the direction of the beam pattern can be steered by varying the time delay appropriately. The magnitude of this time delay can be expressed as [1]

$$\Delta T = \frac{d}{c}\cos\theta_0 . \tag{2.17}$$

2.1.5 Photonic True-Time Delay

As discussed, the feed networks and phase shifters for PAAs have traditionally been implemented in the electrical domain using microwave components. These systems are limited by the high loss associated with electrical distribution lines, such as coaxial cable, as well as the large size and heavy weight of the electrical feed network. These constraints limit their usefulness, especially in applications such as airborne radar where weight and size are critical parameters.

A photonic solution offers the possibility of alleviating the key disadvantages of electrical implementations. The size and weight of an optical component feed network is orders of magnitude less than that of the microwave equivalent. The low loss of optical fiber places virtually no restriction on the length of feed cables. In fact, an optical system introduces the possibility of centrally locating the signal generation equipment and optically distributing the signal to a remote antenna site. This would greatly reduce the cost and complexity associated with the remote site. Another benefit is the immunity to electromagnetic interference of optical fiber. This is a key drawback in electrical networks where care must be taken to reduce all signal coupling effects.

One of the current disadvantages, however, of an optics-based system is the photodetector used to convert a signal from the optical domain to the electrical domain. This component can have issues with linearity over its entire operation range and it can also impose power restrictions on the input signal to avoid saturation of the device.

The TTD beamforming module studied in this research project uses optical delay lines consisting of uniform FBGs to achieve the variable time delay progression required to steer the antenna beam pattern. The following section describes FBGs in more detail and introduces the theoretical model used in their design and fabrication, while the TTD module itself will be discussed in Chapter 5.

2.2 Fiber Bragg Gratings

2.2.1 Background

An FBG can be defined as a periodic perturbation of the refractive index along a section of optical fiber, which is formed by exposure of the core to an intense optical interference pattern [28]. Hill and his coworkers at the Communications Research Centre, Ottawa, Canada first demonstrated the formation of gratings in an optical fiber in 1978. These first gratings were formed by launching intense argon ion laser radiation, at 488 nm, into a germanium-doped fiber, which, after several minutes, showed an increase in the reflected light intensity. This reflected light intensity grew until almost all the light was reflected from the fiber [28]. While demonstrating the potential for exploiting the photosensitivity of Ge-doped fiber, these first experiments had an important limitation: the grating reflection only functioned at wavelengths close to that of the writing light.

About ten years later, in 1989, this limitation was overcome by Meltz [29] who showed that UV radiation, at 244 nm, could be used to form gratings that would reflect any wavelength, by illuminating the fiber through the side of the cladding with two intersecting beams of UV light. This technique, known as the transverse holographic technique, can be seen in Fig. 2.8.

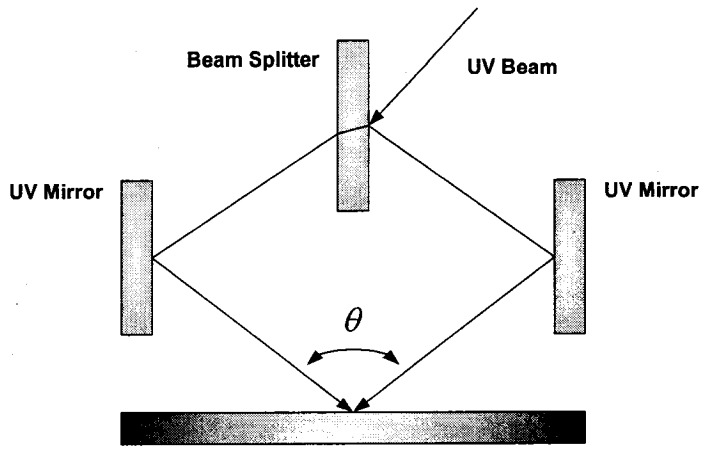

Fig. 2.8. Transverse holographic method of writing fiber Bragg gratings.

This technique allows the period of the grating and the index change to be set by the angle between the beams and the UV wavelength, and produces gratings that have a much higher reflection efficiency [28]. Thus, even though UV light is used to fabricate the grating, they can be made to function at any wavelength, and in spectral regions of interest for devices in optical communications and fiber sensors.

Some advantages of FBGs over competing technologies include an all-fiber geometry, low insertion loss, high return loss, and potentially low cost [30]. The greatest advantage

of FBGs though, is the flexibility they offer for achieving desired spectral characteristics. Physical parameters, including induced index change, length, apodization, period chirp, and fringe tilt, can all be changed. Varying these parameters can produce grating spectrums with widely ranging bandwidths, sharp cut-offs, low sidelobe levels, and specifically designed dispersive characteristics [30].

2.2.2 Mathematical Model

FBGs are formed by exposing the fiber core to a spatially varying pattern of UV light that creates a periodic perturbation of the refractive index along a section of optical fiber. Each individual corrugation of the grating reflects a small amount of light which all add up in-phase to produce a strong back-reflected wave. Only those wavelengths which satisfy a specific requirement will be reflected, all others will be transmitted through the grating. This requirement is known as the Bragg condition, and is defined as [31]

$$\lambda_B = 2n_{eff}\Lambda \tag{2.18}$$

where λ_B is the Bragg reflection wavelength, n_{eff} is the effective refractive index of the fiber, and Λ is the period of the grating perturbation.

The perturbation to the effective refractive index itself can be described by [30]

$$\delta n_{eff}(z) = \overline{\delta n}_{eff}(z)\left\{1 + v\cos\left[\frac{2\pi}{\Lambda}z + \phi(z)\right]\right\} \tag{2.19}$$

where $\overline{\delta n}_{eff}$ is the "DC" index change averaged over a grating period, v is the fringe visibility of the index change, and ϕ describes the grating chirp.

Coupled-mode theory [30], [32], [33] is a good tool for obtaining quantitative information on the spectral and dispersive characteristics of an FBG. For an FBG, interaction near the Bragg wavelength will see a mode of amplitude $A(z)$ coupled into a counter-propagating mode of amplitude $B(z)$. The coupled-mode theory equations may be simplified by retaining only terms that are related to the amplitudes of the two counter-propagating modes and neglecting terms that contribute little to the growth and decay of the amplitudes [30].

The resulting equations can be written as

$$\frac{dR}{dz} = j\hat{\sigma}R(z) + j\kappa S(z) \tag{2.20a}$$

$$\frac{dS}{dz} = -j\hat{\sigma}S(z) - j\kappa^* R(z) \tag{2.20b}$$

where $R(z) = A(z)e^{j\delta z - \phi/2}$ and $S(z) = B(z)e^{-j\delta z + \phi/2}$, κ is the "AC" coupling coefficient, and $\hat{\sigma}$ is a general "DC" self-coupling coefficient defined as

$$\hat{\sigma} \equiv \delta(\omega) + \sigma - \frac{1}{2}\frac{d\phi}{dz} \tag{2.21}$$

where the derivative $-\frac{1}{2}\frac{d\phi}{dz}$ describes possible chirp in the grating.

$\delta(\omega)$ is the detuning away from the Bragg frequency and is defined as

$$\delta(\omega) \equiv \beta(\omega) - \beta_B . \tag{2.22}$$

Since
$$\beta(\omega) = \frac{2\pi n_{eff}}{\lambda} \tag{2.23}$$

and
$$\beta_B = \frac{\pi}{\Lambda} \tag{2.24}$$

(2.22) becomes

$$\delta(\omega) = 2\pi n_{eff}\left(\frac{1}{\lambda} - \frac{1}{\lambda_B}\right). \tag{2.25}$$

The simplified "DC" and "AC" coupling coefficients are given by

$$\sigma = \frac{2\pi}{\lambda}\overline{\delta n}_{eff} \tag{2.26a}$$

$$\kappa = \kappa^* = \frac{\pi}{\lambda} v\overline{\delta n}_{eff}\,. \tag{2.26b}$$

For a uniform grating along z, $\overline{\delta n}_{eff}$ is a constant and $\frac{d\phi}{dz} = 0$, therefore, σ and κ are constants. Thus, (2.20a) and (2.20b) are coupled first-order ordinary differential equations with constant coefficients, for which closed-form solutions are readily attainable when appropriate boundary conditions are applied. The amplitude reflection coefficient, ρ, of a uniform grating of length L can then be shown to be [30]

$$\rho = \frac{-\kappa \sinh\left(\sqrt{\kappa^2 - \hat{\sigma}^2}L\right)}{\hat{\sigma}^2 \sinh\left(\sqrt{\kappa^2 - \hat{\sigma}^2}L\right) + j\sqrt{\kappa^2 - \hat{\sigma}^2}\cosh\left(\sqrt{\kappa^2 - \hat{\sigma}^2}L\right)}. \tag{2.27}$$

The following figures illustrate the effect of the length of a uniform, non-apodized grating on its reflectivity and group delay.

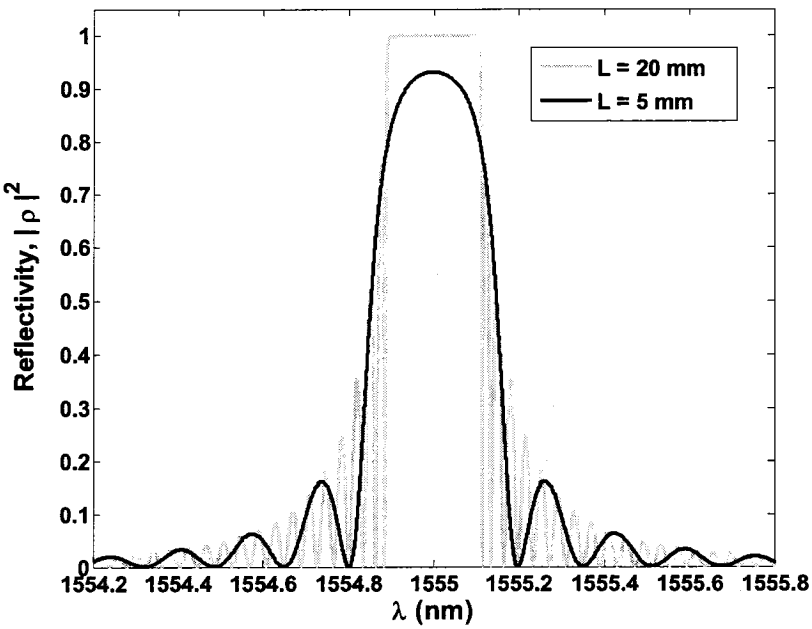

(a)

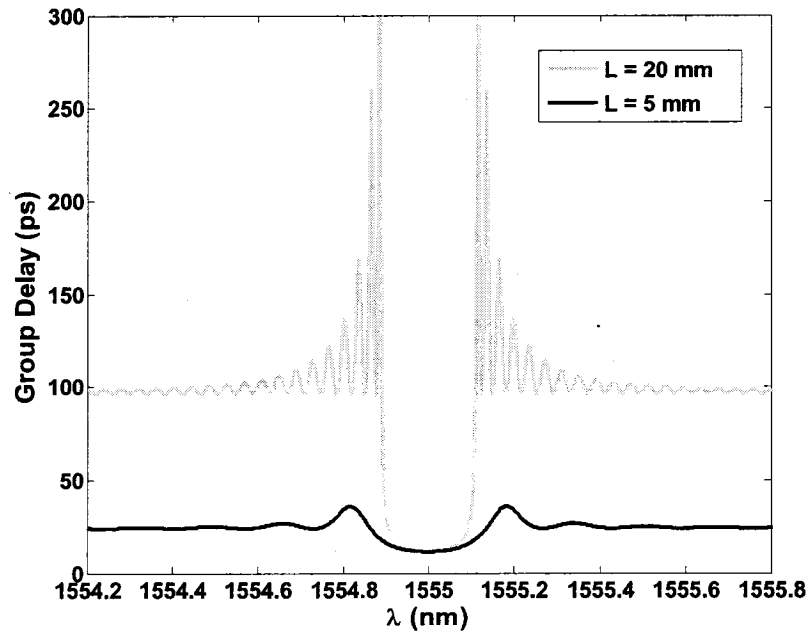

(b)

Fig. 2.9. Simulation of two uniform, non-apodized FBGs with different lengths. (a) Reflectivity, $|\rho|^2$; (b) Group Delay.

Looking at the reflectivity plot in Fig. 2.9(a), the longer grating achieves full reflection around 1550 nm while the shorter grating's reflection is less than 100%. In addition, the shape of the longer grating's reflection spectrum closely matches an ideal box-like shape, whereas the shorter grating's spectrum is more rounded. The longer FBG also exhibits a substantially greater amount of group delay, as shown in Fig. 2.9(b). The appearance of sidelobes, in both the reflection spectrum and the group delay, is also more prominent in the case of the longer grating.

Most FBGs designed for practical applications are actually apodized gratings. Apodization is a technique that can be used to shape the spectral characteristics of an FBG. This technique consists of profiling the refractive index modulation in an optical fiber [28], [34]-[37]. Usually, the main reason for choosing a particular apodization profile is to reduce the undesirable sidelobes prevalent in non-apodized grating spectra. The index modulation of a non-apodized FBG begins and ends abruptly forming an approximately rectangular function of space. Since the Fourier transform of a rectangular function is a *sinc* function, a non-apodized grating exhibits substantial sidelobes in its reflection spectrum with a distinct *sinc*-like pattern.

Many apodization profiles, e.g. Gaussian, raised-cosine, or *sinc*, can be used to reduce the sidelobes on either side of the main reflection peak of the grating spectral response. The Fourier transforms of these apodized profiles do not exhibit substantial sidelobes, and, thus, this characteristic can be used to produce FBGs with suppressed sidelobes.

Another consideration when using apodization is the average refractive index over the length of the grating. If the refractive index modulation amplitude is simply changed without considering the average refractive index, a noticeable effect becomes present on the short wavelength side of the spectral response. Specifically, substantial sidelobes are formed that can be attributed to a Fabry-Perot effect [38]. In order to prevent this problem, the average refractive index should be kept constant over the entire length of the FBG. The following figure shows examples of the refractive index modulation profiles of a non-apodized FBG, a Gaussian-apodized FBG and a "constant average-dc index" FBG.

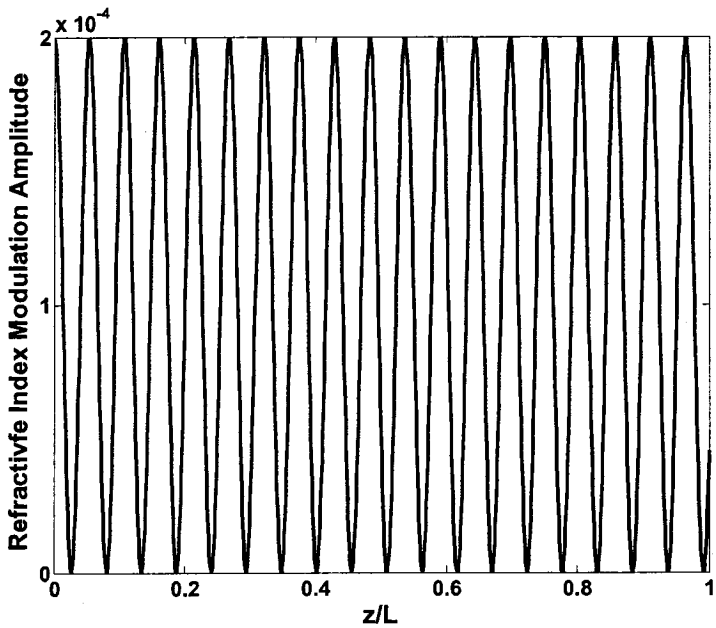

Fig. 2.10 (a). Refractive index modulation profile for a non-apodized FBG.

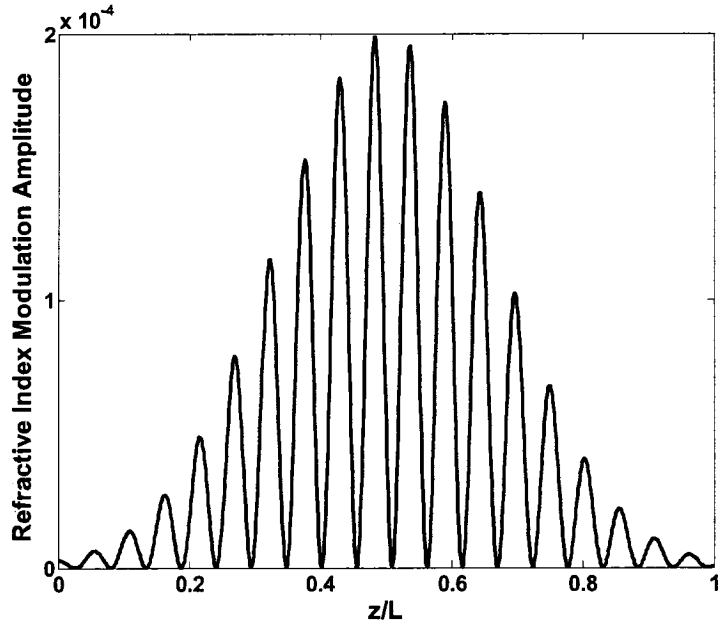

(b)

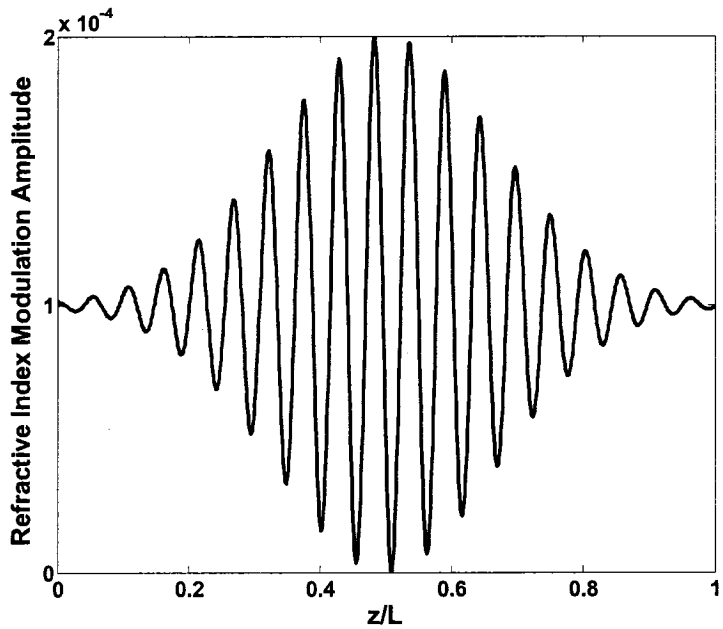

(c)

Fig. 2.10. Refractive index modulation profile for (b) a Gaussian-apodized FBG; and (c) a Gaussian-apodized FBG with a constant average refractive index.

When simulating gratings that have arbitrary apodization profiles or that are chirped, a closed form solution to the coupled-mode equations does not exist. There are, however, two standard approaches for calculating the reflection and transmission spectra for these types of FBGs. The first is direct numerical integration of the coupled-mode equations. Although this approach is straightforward, it is usually not the fastest method and will not be considered further. The second approach, and the one used in the simulation of FBGs in this project, is a piecewise-uniform approach, or the transfer matrix method (TMM). In this method, the grating is divided into a number of uniform sections and the closed-form solutions for each uniform section are combined using matrix multiplication [30]. This method is sufficiently accurate, simple to implement, and usually the fastest.

In the TMM, the grating is divided into M uniform sections of length δL and a 2 x 2 matrix is identified for each of these sections. Over this short section of grating, the period, $\Lambda(z)$, and the coupling coefficients, $\sigma(z)$ and $\kappa(z)$, are assumed to be constant. Thus, this short section of the grating can be considered to be uniform.

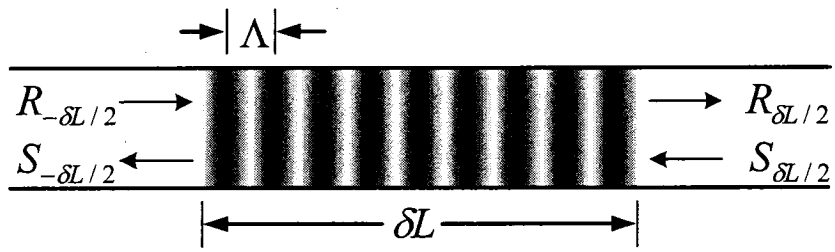

Fig. 2.11. Diagram illustrating the transfer matrix method for a uniform grating.

The propagation through each uniform section is represented by a transfer matrix, T_i, defined such that

$$\begin{bmatrix} R_{\delta L/2} \\ S_{\delta L/2} \end{bmatrix} = T_i \begin{bmatrix} R_{-\delta L/2} \\ S_{-\delta L/2} \end{bmatrix} \tag{2.28}$$

where the transfer matrix, T_i, for the uniform section of length δL can be expressed as

$$T_i = \begin{bmatrix} \cosh(\Omega\delta L) - j\frac{\hat{\sigma}}{\Omega}\sinh(\Omega\delta L) & -j\frac{\kappa}{\Omega}\sinh(\Omega\delta L) \\ j\frac{\kappa}{\Omega}\sinh(\Omega\delta L) & \cosh(\Omega\delta L) + j\frac{\hat{\sigma}}{\Omega}\sinh(\Omega\delta L) \end{bmatrix} \tag{2.29}$$

where $\Omega = \sqrt{\kappa^2 - \hat{\sigma}^2}$.

The transfer matrices for each uniform section are then multiplied together to obtain the overall transfer matrix for the entire non-uniform Bragg grating of length L.

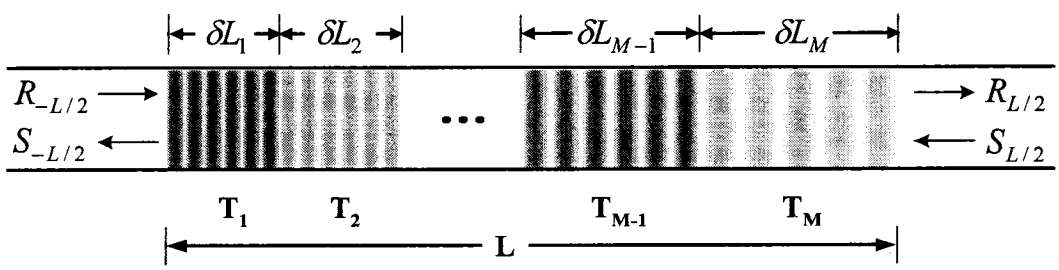

Fig. 2.12. Diagram illustrating transfer matrix method for a non-uniform grating.

This overall transfer matrix can be expressed as

$$\begin{bmatrix} R_{L/2} \\ S_{L/2} \end{bmatrix} = T_M \cdot T_{M-1} \cdot \ldots \cdot T_2 \cdot T_1 \cdot \begin{bmatrix} R_{-L/2} \\ S_{-L/2} \end{bmatrix}. \tag{2.30}$$

When using the TMM, the number of sections used, M, is determined by the required accuracy. Usually, $M \approx 100$ sections is sufficient. It is also important to note that M cannot be arbitrarily large, since the slowly varying approximation requires that the amplitude of the mode change slowly over the distance of a wavelength of the light. Thus, the derived coupled-mode equations are not valid when a uniform section is only a few grating periods long [30]. Therefore, it must be ensured that $\delta L >> \Lambda$, which leads to the condition on M that

$$M << \frac{2n_{eff}L}{\lambda_B}. \tag{2.31}$$

The following figures show examples of the reflection spectra of a uniform, non-apodized FBG, a Gaussian-apodized FBG and a "constant average-dc index" FBG.

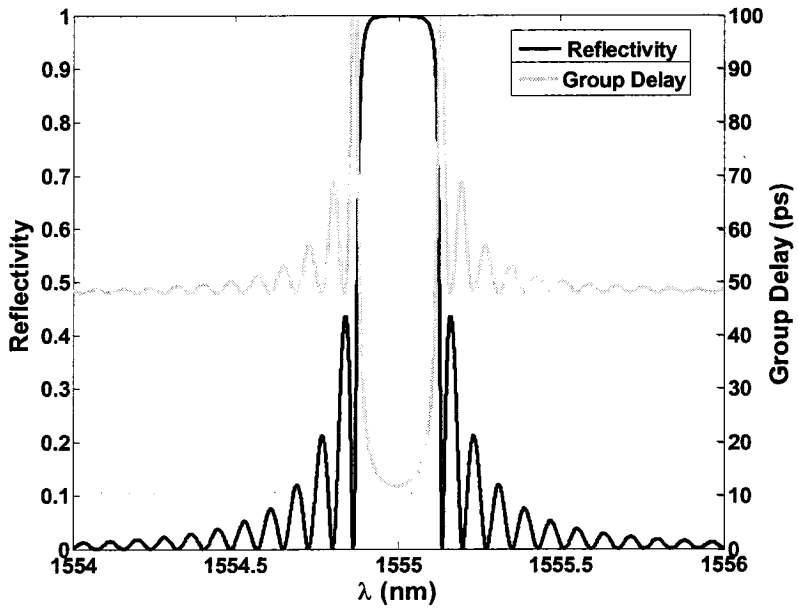

(a)

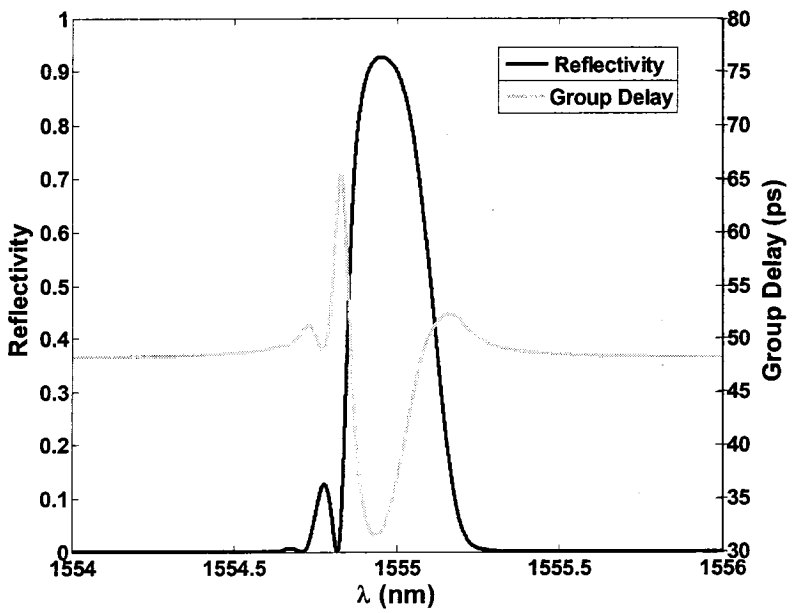

(b)

Fig. 2.13. Reflection spectra and group delay of (a) a uniform, non-apodized FBG; and (b) a Gaussian-apodized FBG with a varying average refractive index.

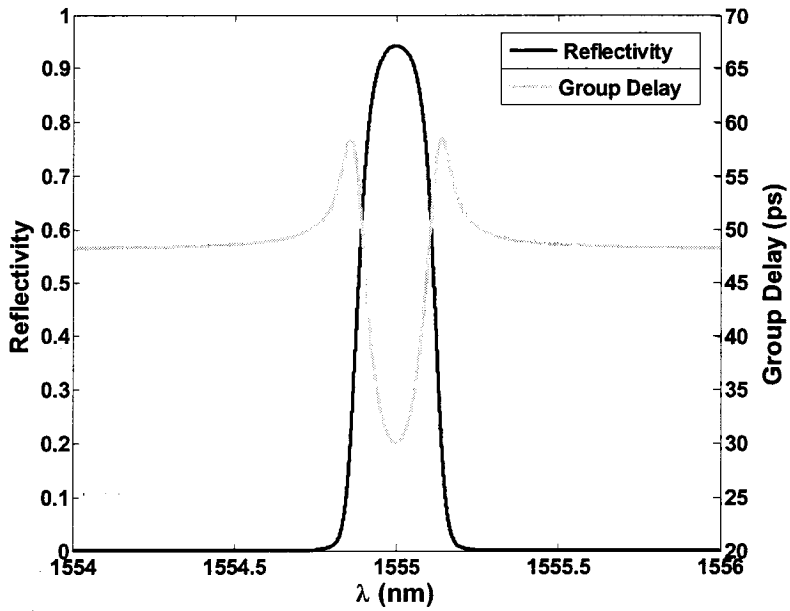

Fig. 2.13(c). Reflection spectra and group delay of a Gaussian-apodized FBG with a constant average refractive index.

2.2.3 Fabrication of Fiber Bragg Gratings

The two earliest techniques of fiber Bragg grating fabrication – internal writing and the holographic technique – have been described in Section 2.2.1. These have largely been superseded by the phase mask technique [28].

This technique uses a phase mask to "imprint" the grating into the fiber core. The phase mask is fabricated on a flat slab of silica glass which is transparent to UV light. On one surface, a one dimensional periodic relief pattern is etched using photolithographic techniques [28]. The optical fiber is placed almost in contact with one side of the mask

and UV light, incident normal to the phase mask, passes through and is diffracted by the periodic corrugations of the phase mask. Most of the diffracted light is contained in the 0, +1 and -1 diffracted orders and the phase mask is designed such that minimum radiation is transmitted in the 0^{th} order and maximum radiation is transmitted into the two first-order beams [39], [40]. This arrangement can be seen in Fig. 2.14.

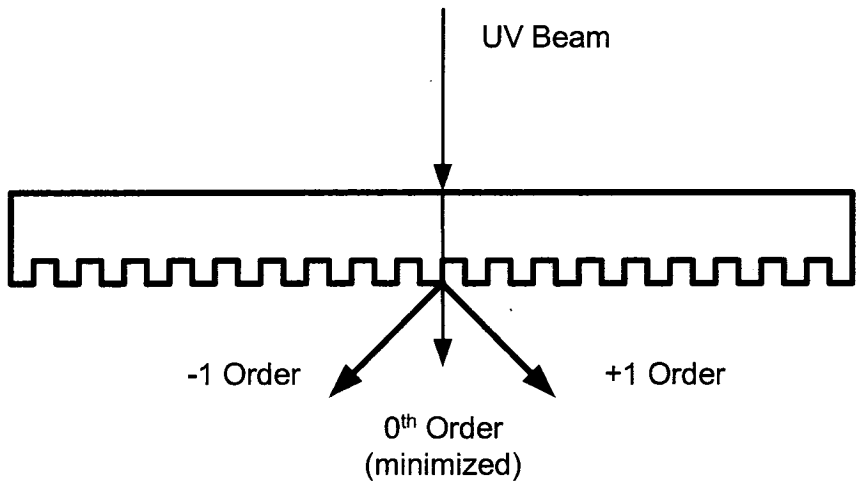

Fig. 2.14. Zero-order-nulled phase mask technique using a UV beam.

The period of the FBG is related to the Bragg wavelength by the following relation

$$\lambda_B = n_{eff}\Lambda_{PM} \tag{2.32}$$

where Λ_{PM} is the period of the corrugation etched into the phase mask. Thus, the period of the grating is exactly one half the period of the phase mask corrugation and this period is independent of the ultraviolet wavelength used to expose the grating.

The phase mask technique has the advantage of simplifying the exposure process while still yielding gratings with a high performance. It offers easier alignment, higher stability and lower coherence requirements for the exposure beam in comparison to the holographic technique [28]. A drawback of the phase mask technique is that it requires a separate phase mask for each different Bragg wavelength. However, some wavelength tuning is possible by applying tension to the fiber during the exposure process. This technique will be discussed further in Section 5.1.5.

2.2.4 Photosensitivity

Photosensitivity refers to a permanent change in the refractive index of a material induced by exposure to light radiation [31]. Many techniques exist to photosensitize optical fibers, including the use of codopants, hot hydrogenation, and high-pressure, cold hydrogenation.

High-pressure, cold hydrogen-loading (or hydrogenation) can be used to make a standard single-mode fiber more photosensitive. Hydrogen in-diffuses into the fiber core until an equilibrium state is reached. After hydrogen-loading, exposure to UV radiation leads to the formation of defects within the fiber that increase the refractive index. Loading the fiber requires only a suitable high-pressure chamber to store the fibers for a period of time. Normally, storing the fiber in a hydrogen environment at 200 atm at room temperature for a period of two weeks is sufficient to load a standard diameter fiber [31].

Exposure of hydrogen-loaded fibers using this technique has yielded refractive index changes of 0.011 in standard single-mode fiber [31], [41].

This research project uses a high-pressure, cold hydrogen-loading process to photosensitize all fibers used in the fabrication of FBGs.

2.3 Summary

This chapter introduced the theory associated with phased-array antennas and presented the theoretical model for an *N*-element linear array, including the derivation of its normalized array factor. Simulation results were presented highlighting the effects of changing certain physical parameters of the array, such as element spacing, number of elements and magnitude of the phase progression. The beam squint effect was also illustrated, along with the benefits of using a photonic TTD module as the feed network for a PAA. The FBG theoretical model, based on coupled mode theory, was also introduced in this chapter. Several methods of apodization were presented, along with three FBG fabrication techniques, including the phase mask technique used in this project. The concept of photosensitizing an optical fiber through hydrogen-loading was also discussed.

Chapter 3

THE OPTICAL PHASE-LOCK LOOP

This chapter introduces several techniques for the optical generation of microwave signals in radio-over-fiber (RoF) systems. It describes the principle of optical heterodyning and presents the transfer function equations of an optical phase-lock loop. The function of a delay-line frequency discriminator, as part of an OPLL, is explored, as well as the effects of laser linewidth on system performance.

3.1 Radio-over-Fiber

Radio-over-fiber is a technology in which microwave and millimeter-wave (mm-wave) signals are distributed over optical fiber. RoF is a cost effective method for distributing these signals since it allows expensive, high-frequency signal generation equipment to be centrally located and the generated microwave/mm-wave signals to be distributed over optical fiber to remote antenna sites. This greatly reduces the cost and complexity of the equipment required, since now a high precision microwave oscillator is no longer required at each remote location [42], [43].

Many advantages come with the use of such an arrangement. They include the following:

1) Low loss – Electrical distribution of high frequency microwave signals in free space or via transmission lines, such as coaxial cable, is difficult and expensive due to the prohibitively high transmission losses. An alternative is to exploit the low transmission loss associated with standard single-mode optical fibers. Losses on the order of 0.2 dB/km in the 1.5 μm transmission window allow optical signals to be transmitted over long distances with low loss, enabling the high-frequency microwave signals to be economically distributed to remote sites.

2) Immunity to electromagnetic interference – This is also a very attractive property of optical fiber, especially in PAA applications which involve the close proximity of many connections in an antenna feed network. Since the optical signals are transmitted in the form of light, electromagnetic cross-talk is non-existent.

3) Ease of installation and reduced power consumption – By centrally locating the complex, expensive signal generation equipment, remote sites are much simpler. This leads to reduced installation and maintenance cost and also much lower power consumption, as now most components at the remote site can be operated in a virtually passive configuration.

4) Other benefits – Some other benefits include advanced radio system functions in the optical domain, such as filtering, and signal processing at high frequencies; and large available bandwidth.

3.2 Optical Techniques for Generating Microwave Signals

The techniques for optically generating microwave signals generally fall into two main categories: Intensity Modulation – Direct Detection (IM-DD) and Remote Heterodyne Detection (RHD) [24].

3.2.1 Intensity Modulation – Direct Detection

This technique involves modulating the intensity of an optical source with the desired microwave signal. There are two ways to accomplish this intensity modulation (IM). The first involves directly modulating the laser bias current with the microwave signal. The second uses an external modulator such as a Mach-Zehnder modulator (MZM) to modulate the laser output with the microwave signal. In each case the RF signal is intensity modulated onto a single optical carrier, which is then transmitted through an optical fiber. The RF signal is recovered at the other end by direct detection. Fig. 3.1 shows the two IM schemes.

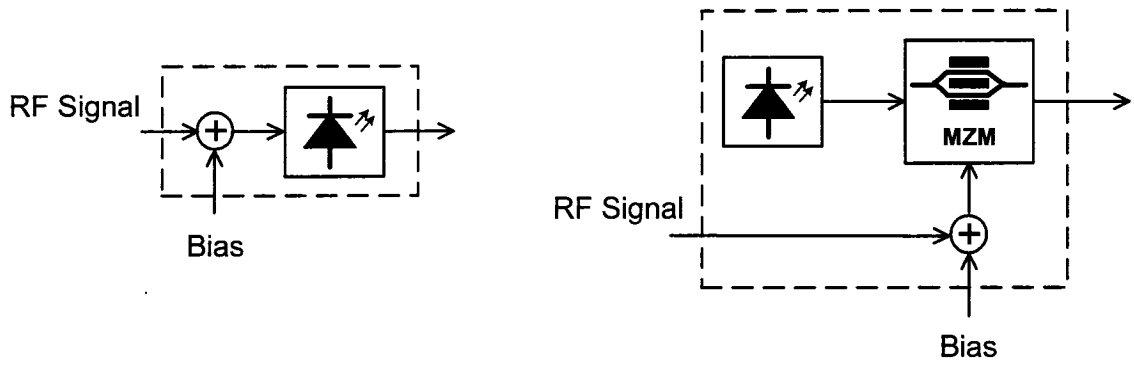

(a) (b)

Fig. 3.1. IM-DD signal generation by (a) direct modulation of a laser diode; and (b) external modulation.

Any data that has been modulated onto the microwave signal will also be recovered by this scheme. The advantages of this type of link are its simplicity and its transparency to the modulation format used. The disadvantages of these techniques are that they are limited to relatively low microwave frequencies since the modulating signal must be as high as the microwave output frequency. Direct laser modulation is simply not possible at higher microwave frequencies due to lack of bandwidth. External modulators exist for frequencies up to about 100 GHz but the drive voltage at those levels is very high, leading to costly drive amplifiers, and linearity issues.

3.2.2 Remote Heterodyne Detection

Remote heterodyne techniques are based on the principle of optical heterodyning – the coherent mixing of two frequency-offset optical carriers on a photodiode to produce a microwave output.

The optical carrier electric fields can be represented as

$$e_1(t) = E_1 \cos(\omega_1 t + \phi_1) \tag{3.1a}$$

$$e_2(t) = E_2 \cos(\omega_2 t + \phi_2) \tag{3.1b}$$

where E_1 and E_2 are the amplitudes (V/m), ω_1 and ω_2 are the angular frequencies (rad/s) and ϕ_1 and ϕ_2 are the instantaneous phases (rad) of the two optical carriers, respectively. When both fields impinge on the surface of a PIN photodiode the resulting photocurrent is given by the following expression:

$$\begin{aligned} i_{PIN}(t) &= \left|e_1(t) + e_2(t)\right|^2 \\ &= \tfrac{1}{2}\left(\left|E_1\right|^2 + \left|E_2\right|^2\right) + \left|E_1 E_2\right| \cos[(\omega_1 - \omega_2)t + \phi_1 - \phi_2] + \left|E_1 E_2\right| \cos[(\omega_1 + \omega_2)t + \phi_1 + \phi_2] \end{aligned} \tag{3.2}$$

where the first term on the right hand side is a DC term and the last term is a very high frequency term that is outside the bandwidth of the PD. The term of interest then, is the

middle term, $|E_1E_2|\cos[(\omega_1-\omega_2)t+\phi_1-\phi_2]$, which indicates that a microwave output can be generated simply by controlling the spacing between the two optical carriers.

The advantages of this technique include:

1) Very high frequency generation – limited only by the PD bandwidth.
2) High output power – almost all the power in the two optical carriers contributes to the power of the generated microwave signal.
3) Minimization of the chromatic dispersion-induced power penalty [25]
4) Low-frequency data modulation – the microwave signal is generated by the optical wavelength spacing, so the data can be modulated at a baseband or intermediate frequency. Thus, modulation can be done at lower cost and at a lower drive voltage, ensuring the process is within the modulator's linear region.

The main disadvantage of this optical heterodyning technique is the requirement for the two optical carriers to be phase-correlated. As indicated by (3.2), any phase noise in the optical sources will translate directly into phase noise in the generated microwave signal. Therefore, some technique must be used to reduce the phase noise normally present in semiconductor lasers if they are to be used as the optical sources.

Several techniques exist for implementing RHD. They include both single and dual laser methods.

3.2.2.1 Single Laser Methods

a) Single-Laser Heterodyne

The first method is a single-laser technique that involves modulating the optical source with an electrical signal of frequency, f_0, to generate a series of optical spectral lines (sidebands around the carrier) spaced by the applied frequency. Two sidebands of interest are then selected, spaced by the desired microwave frequency, and the others are filtered out by some type of optical filtering technique. The microwave signal is recovered by heterodyning the two remaining sidebands on a PD. This configuration is shown in Fig. 3.2. The advantage of this configuration is that the two sidebands are already phase-correlated since they are produced by the same optical source. Therefore, very narrow linewidth microwave signals can be produced using very large linewidth optical sources. The disadvantage, however, is that the sideband filtering system must be very selective, due to the narrowly spaced sidebands.

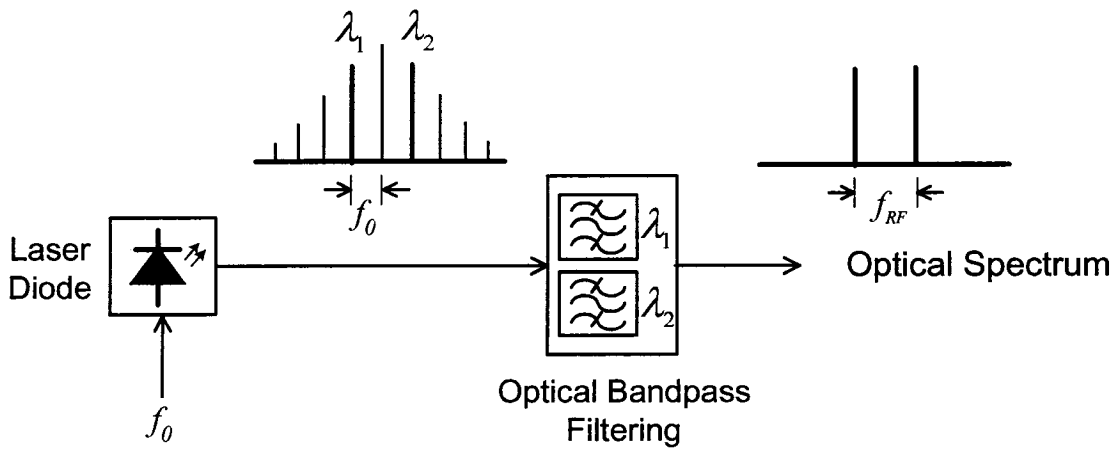

Fig. 3.2. Single-laser heterodyne technique.

b) Dual-Wavelength Laser

Another single-laser technique is the dual-wavelength laser. In this technique two separate wavelengths are generated within the same laser cavity with a certain frequency offset between the two wavelengths [44], [45]. They are then heterodyned on a PD to produce a microwave output. Phase-locking of the two wavelengths is accomplished by electrical sub-harmonic injection [46], and can be used to produce a high-quality, low-phase noise output. The main advantage of this technique is that it does not require a complex feedback setup to phase-lock the two wavelengths. It is, however, difficult to tune the frequency.

3.2.2.2 Dual Laser Methods

In dual-laser techniques two optical sources emit light at frequencies separated by the desired microwave frequency. Due to the very high frequencies (THz) of the optical signals any small variations in drive current or temperature can result in a very large change in the microwave output frequency since the two sources are not phase-correlated. Therefore, efforts must be made to track the frequency and phase fluctuations that occur in each optical source.

a) Optical Injection Locking (OIL)

This technique involves modulating a master laser with a low frequency electrical signal, f_0, which is a sub-harmonic of the round trip cavity length of a slave laser. As in the

single-laser heterodyne technique, this produces a spectrum of sidebands around the master laser frequency. Part of this output spectrum is then fed directly into the cavity of the slave laser and, since f_0 is a harmonic of the slave laser resonant frequency, the slave laser locks onto one of the sidebands. A schematic of this setup is shown in Fig. 3.3. By keeping f_0 constant, the slave laser will track this master laser sideband and follow any frequency and phase fluctuations that take place in the master laser output [47].

The microwave output frequency will be determined by the spacing between the master laser central frequency and the sideband to which the slave laser is locked. Therefore, the output frequency will be a multiple of f_0. The ability to generate high-frequency stable microwave outputs using this technique has been demonstrated in [48]-[50].

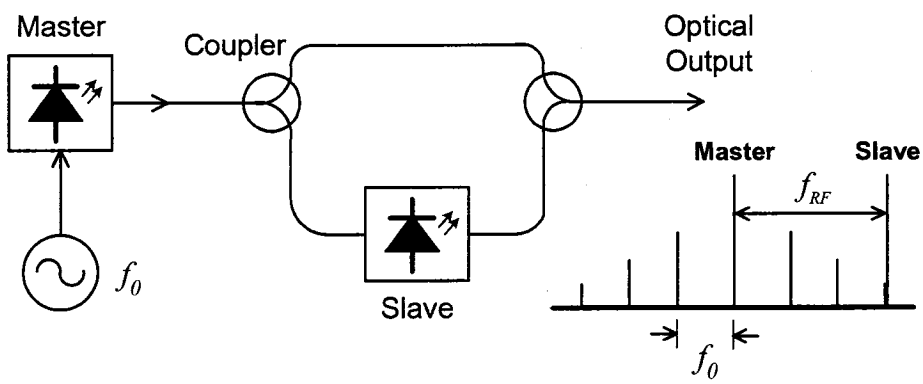

Fig. 3.3. Optical Injection Locking

One advantage of this technique is the ability to use cheaper, broad-linewidth semiconductor lasers while still producing a narrow linewidth microwave output with good phase noise performance. Another benefit comes from the fact that the slave laser

locks to a sub-harmonic of the modulating frequency. This means that a lower frequency reference signal can be used to produce a higher frequency output.

The disadvantage of this technique is its small detuning range. The microwave output cannot be tuned very far before the lasers lose the lock established by the injection.

b) Optical Phase-Lock Loop (OPLL)

The OPLL technique is another dual-laser arrangement; its schematic is shown in Fig. 3.4.

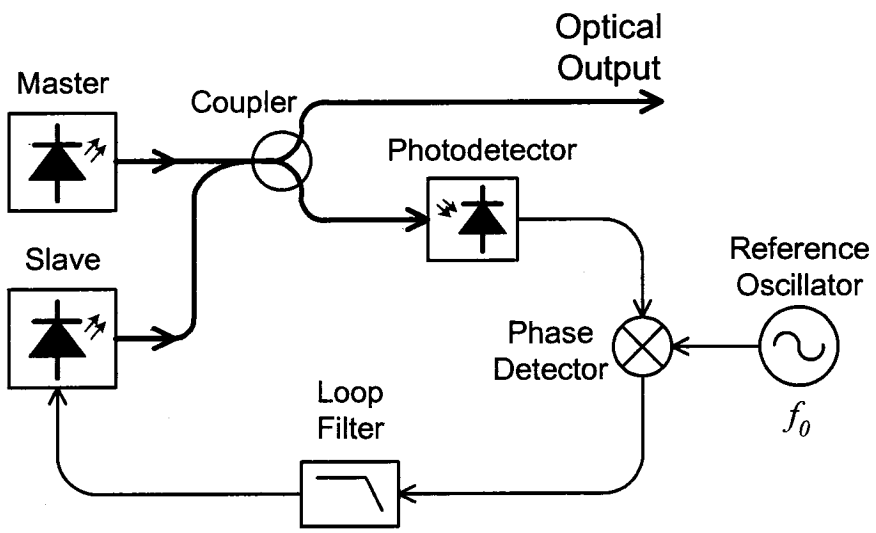

Fig. 3.4. Optical Phase-Lock Loop

The output from the master and slave laser is combined by an optical coupler with part of this signal being taken as the source output and the other being fed back into the system. The portion used for feedback is heterodyned at a PD, producing a beat signal at a frequency corresponding to the offset between the two optical wavelengths. A phase detector then compares the recovered beat signal with a microwave reference source that

is operating close to the beat frequency. This comparison produces a phase error signal that is proportional to the phase difference between the beat signal and the reference. The loop filter processes this error signal, removing any high frequency components, and produces a DC feedback to the slave laser. In this way, the feedback loop allows the slave laser to track any phase changes that occur in the master laser [47], [51], [52].

One of the advantages of this technique is the high-quality, low phase noise microwave signals that can be produced since the feedback loop tracks the small phase variations in the optical sources. Another benefit is the large detuning range that can be achieved. Simply by tuning the reference source, the microwave output of the OPLL can be widely tuned.

This technique, however, requires that the slave laser have a sufficiently high tuning rate to track the very fast phase fluctuations of the master laser. This also implies that the loop must have a sufficient feedback bandwidth. One of the parameters that determines the necessary feedback bandwidth is the summed laser linewidth. If distributed feedback semiconductor lasers are used, with typical linewidths of about 2 MHz, the feedback bandwidth must be very wide. This indicates that a short loop propagation delay (on the order of a few nanoseconds) is required. This short propagation delay is only feasible using integrated or micro-optic solutions for semiconductor lasers [53]. In the case of a fiber-based solution with discrete components, a laser with a much narrower linewidth is required, such as an external cavity laser (ECL), and careful attention must be paid to all connection lengths and component delay times.

c) Optical Injection Phase-Lock Loop (OIPLL)

As its name implies, this dual-laser method is a hybrid of the two previous techniques. The schematic is shown in Fig. 3.5.

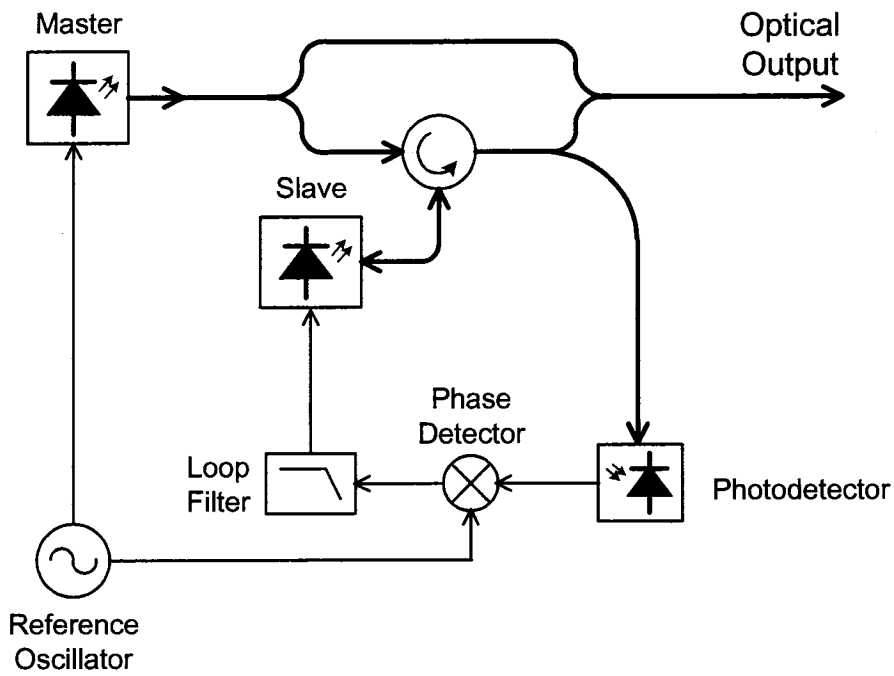

Fig. 3.5. Optical Injection Phase-Lock Loop

This OIPLL combines the advantages of both the previous arrangements. It can produce narrow linewidth signals with a wide detuning range. At the same time, the short loop propagation delay required by an OPLL is less important which allows the use of ordinary, broad linewidth semiconductor lasers [47] [54]-[58]. An obvious disadvantage, however, is the increase in complexity.

3.3 Optical Phase-Lock Loop

This research project incorporates an optical phase-lock loop into a TTD beamforming module to optically generate the microwave signals required. Therefore, the theoretical operation of this configuration will be explored in greater detail than the other implementations. Much work has been done over the last decade to further develop this technology for practical applications [59]-[72].

3.3.1 Transfer Functions of the OPLL

Consider the block diagram of the optical phase-lock loop shown below.

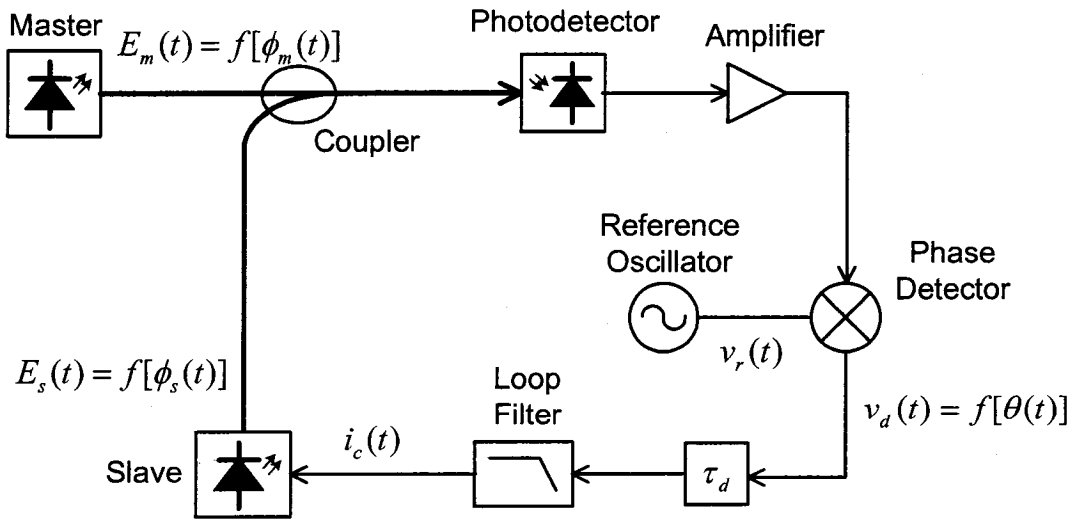

Fig. 3.6. Optical Phase-Lock Loop with signal expressions.

It consists of a master laser, a slave laser, a photodetector, a microwave amplifier, a phase detector, which, in this case, is a double-balanced mixer, a loop filter and a loop delay element. The slave laser for an OPLL is analogous to the VCO (voltage-controlled oscillator) of a conventional phase-lock loop.

Since the phase detector is a double-balanced mixer its output can be written as

$$v_d(t) = K_d \sin\theta(t) \tag{3.3}$$

where K_d is the phase detector gain factor, measured in volts per radian (V/rad), and the phase error, $\theta(t)$, is defined as

$$\theta(t) = \phi_{ms}(t) - \phi_r(t)\,. \tag{3.4}$$

We define

$$\phi_{ms}(t) = \phi_m(t) - \phi_s(t) \tag{3.5}$$

as the difference between master and slave laser phases at the output of the PD. The error voltage, $v_d(t)$, is then processed by the loop filter, whose impulse response is denoted as $f(t)$. The filter output is a control signal, $i_c(t)$, that controls the frequency output of the slave laser. In the time domain, the output of the filter is described as

$$i_c(t) = K_f v_d(t) * f(t) \tag{3.6}$$

where K_f is a transconductance term, measured in mA/V, that represents the voltage-current conversion required to provide a current feedback signal to the slave laser, and * denotes convolution.

In the Laplace transform domain, the output of the filter is described by

$$I_c(s) = K_f V_d(s) F(s) \tag{3.7}$$

where $I_c(s) = \mathrm{L}\{i_c(t)\}$ represents the Laplace transform of the signal $i_c(t)$.

This signal controls the output frequency of the slave laser and, since frequency is the derivative of phase, $f = d\phi / dt$, the control of the slave laser can be described by

$$\frac{d\phi_s(t)}{dt} = K_0 i_c(t) \tag{3.8}$$

where K_0 is the slave laser gain factor, and is measured in $\mathrm{rad/s \cdot mA}$.

Taking the Laplace transform of this expression and noting that $\mathrm{L}\{d / dt\} = s$, we obtain

$$\phi_s(s) = \frac{K_0 I_c(s)}{s}. \tag{3.9}$$

Assuming that the phase detector output can be linearized, i.e the phase error, $\theta(t)$, is assumed to be small enough to allow the approximation $\sin\theta(t) \approx \theta(t)$, the Laplace transform of (3.3) becomes

$$V_d(s) = K_d \theta(s). \tag{3.10}$$

The final component in the OPLL feedback circuit is a loop delay element $\delta(t-\tau_d)$ where τ_d represents the propagation time delay of the correction signal around the entire feedback loop. This loop delay is not negligible for OPLLs and, therefore, must be included in the transfer function derivation. Further effects of this loop delay will be presented in Section 3.5.

Combining these individual expressions, the overall control equation, in the Laplace domain, for the slave laser output phase is

$$\phi_s(s) = \frac{K_0 K_f K_d F(s)\theta(s) e^{-s\tau_d}}{s}. \tag{3.11}$$

where $e^{-s\tau_d} = \mathrm{L}\{\delta(t-\tau_d)\}$ is the Laplace transform of the loop delay component.

This can be rearranged to give the open-loop transfer function for the loop

$$G(s) = \frac{\phi_s(s)}{\theta(s)} = \frac{K_0 K_f K_d F(s) e^{-s\tau_d}}{s}. \tag{3.12}$$

This open-loop transfer function is simply the cascade of the transfer functions of the individual elements.

The system, or closed-loop, transfer function can be expressed as

$$H(s) = \frac{G(s)}{1+G(s)} = \frac{\phi_s(s)}{\theta(s)+\phi_s(s)} = \frac{K_0 K_f K_d F(s) e^{-s\tau_d}}{s + K_0 K_f K_d F(s) e^{-s\tau_d}}. \tag{3.13}$$

In addition, the error transfer function can be expressed as

$$E(s) = \frac{1}{1+G(s)} = 1 - H(s) = \frac{s}{s + K_0 K_f K_d F(s) e^{-s\tau_d}}. \tag{3.14}$$

The expression $1 + G(s) = 0$ is the characteristic equation of the OPLL. The roots of this expression, the values of s that satisfy the equation, are the poles of the closed-loop transfer function. The pole locations are important in determining properties of the loop, such as stability [73].

3.3.2 Loop Filter Design and OPLL Parameters

The loop filter implemented in this research project is a passive lead-lag filter. The schematic of this filter is shown in Fig. 3.7.

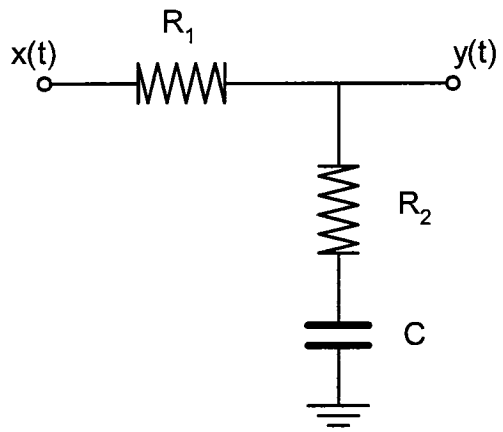

Fig. 3.7. Passive lead-lag loop filter

The transfer function, $F(s)$, of this type of loop filter is given by

$$F(s) = \frac{1 + s\tau_2}{1 + s\tau_1} \tag{3.15}$$

where the time constants of the filter can be expressed as

$$\tau_1 = (R_1 + R_2)C \tag{3.16a}$$

$$\tau_2 = R_2 C\,. \tag{3.16b}$$

Re-expressing (3.13) to include the actual filter transfer function gives

$$H(s) = \frac{K_0 K_f K_d \frac{\tau_2}{\tau_1} s + \frac{K_0 K_f K_d}{\tau_1}}{s^2 + s\left(\frac{1 + K_0 K_f K_d \tau_2}{\tau_1}\right) + \frac{K_0 K_f K_d}{\tau_1}} \tag{3.17}$$

where the loop delay component, $e^{-s\tau_d}$, has been neglected for simplicity, to highlight the other basic properties of OPLL operation.

This transfer function represents a second-order type 1 phase-lock loop (PLL). The *order* of a PLL circuit is determined by the order of the denominator polynomial of the closed-loop transfer function [73]. The loop filter has added a pole to the transfer function, giving the s^2 term in the denominator and making the OPLL second order.

The PLL *type* is determined by the number of integrators in the loop [73]. The OPLL is a type 1 circuit, since the VCO, or, in this case, the slave laser contributes the only integrator. The loop filter is a passive filter; therefore, it does not add a second integrator.

3.3.2.1 Natural Frequency and Damping Coefficient

The two most commonly used parameters to specify the operation of a second-order type 1 PLL are the natural frequency, ω_n (rad/s) and the damping factor, ς, which is

dimensionless [73], [74]. For the transfer function specified in (3.17), these parameters can be expressed as

$$\omega_n = \sqrt{\frac{K_0 K_f K_d}{\tau_1}} \tag{3.18a}$$

$$\varsigma = \frac{1 + K_0 K_f K_d \tau_2}{2\sqrt{K_0 K_f K_d \tau_1}}. \tag{3.18b}$$

They allow the simplification of the closed-loop transfer function to

$$H(s) = \frac{\tau_2 \omega_n^2 s + \omega_n^2}{s^2 + 2\varsigma\omega_n s + \omega_n^2}. \tag{3.19}$$

The error transfer function can also be re-expressed in a similar fashion as

$$E(s) = \frac{s^2 + \frac{s}{\tau_1}}{s^2 + 2\varsigma\omega_n s + \omega_n^2}. \tag{3.20}$$

3.3.2.2 Loop Gain

For the second-order loop presented above, the loop gain can be defined as

$$K = \frac{K_0 K_f K_d \tau_2}{\tau_1} \quad \text{(Hz)} \tag{3.21}$$

which can be seen to be the open loop gain around the OPLL circuit minus the $1/s$ factor contributed by the integration of the slave laser.

Using this definition of K, the closed-loop transfer function from (3.17) becomes

$$H(s) = \frac{K\left(s + \frac{1}{\tau_2}\right)}{s^2 + s\left(\frac{1}{\tau_1} + K\right) + \frac{K}{\tau_2}} \tag{3.22}$$

and the error transfer function becomes

$$E(s) = \frac{s^2 + \frac{s}{\tau_1}}{s^2 + s\left(\frac{1}{\tau_1} + K\right) + \frac{K}{\tau_2}}. \tag{3.23}$$

These expressions can be used to explore the amplitude responses of both the closed-loop transfer function and the error transfer function. Fig. 3.8 - 3.11 show the amplitude responses $|H(j\omega)|$ and $|E(j\omega)|$ for several values of ς [73].

The frequency axes of Figs. 3.8 and 3.9 have been normalized to the natural frequency, ω_n, while the frequency axes of Figs. 3.10 and 3.11 have been normalized to the loop gain, K.

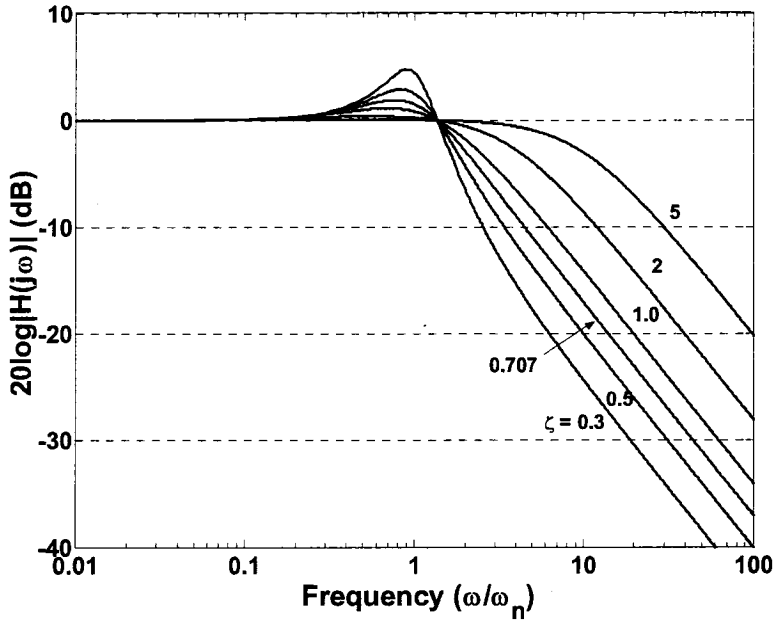

Fig. 3.8. Amplitude response, $|H(j\omega)|$, for a second-order type 1 PLL with frequency normalized to the natural frequency, ω_n.

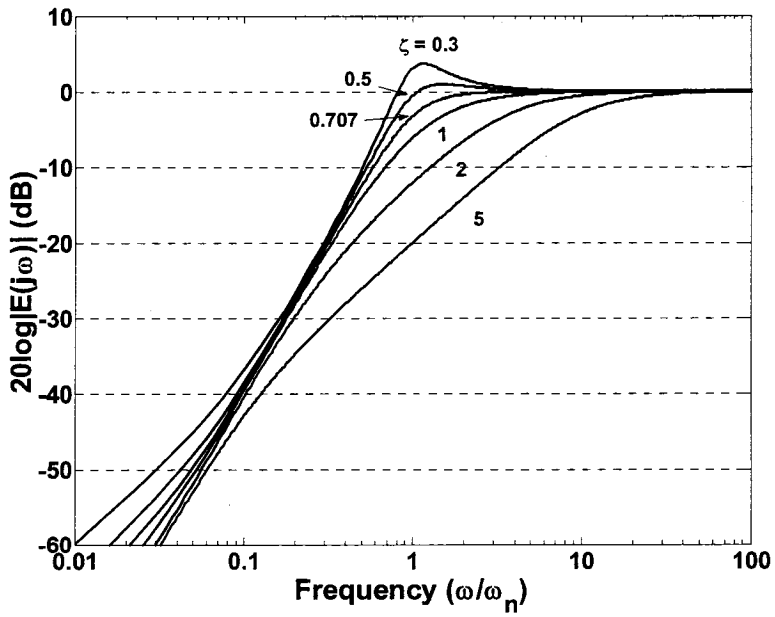

Fig. 3.9. Amplitude response, $|E(j\omega)|$, for a second-order type 1 PLL with frequency normalized to the natural frequency, ω_n.

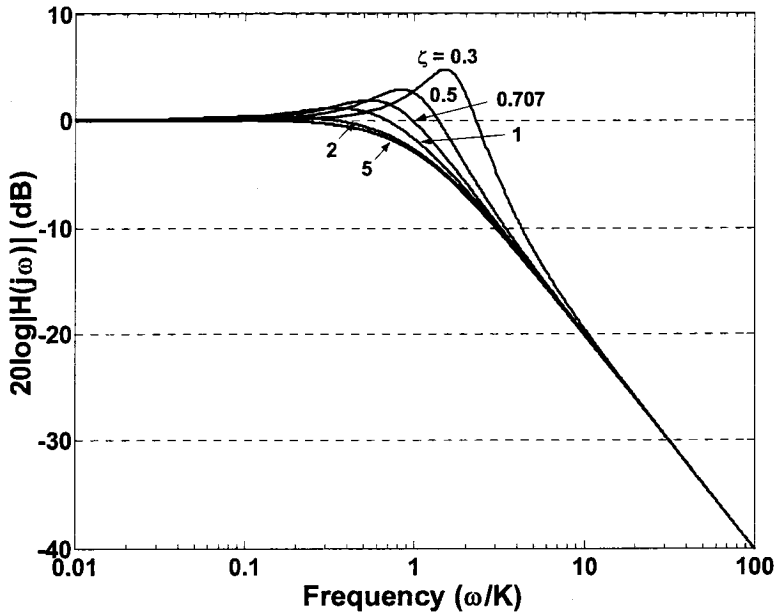

Fig. 3.10. Amplitude response, $|H(j\omega)|$, with frequency normalized to the loop gain, K.

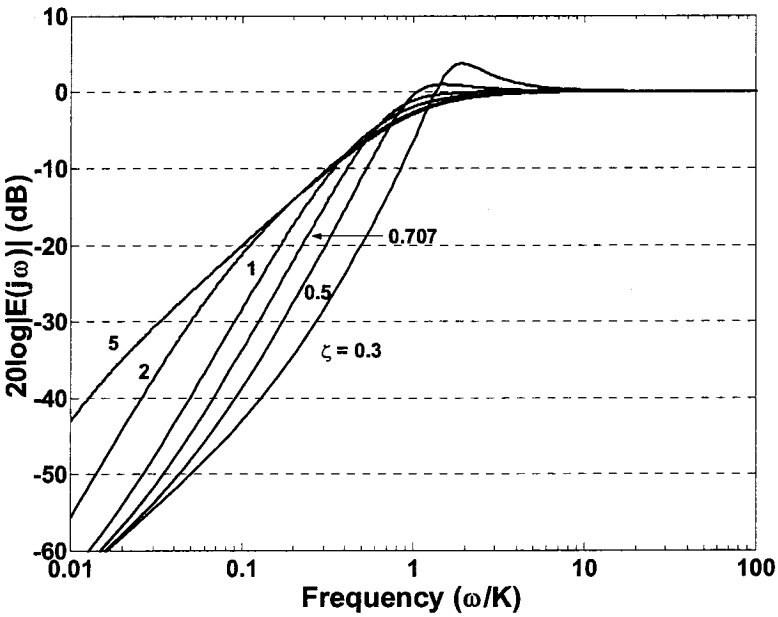

Fig. 3.11. Amplitude response, $|E(j\omega)|$, with frequency normalized to the loop gain, K.

For values of $\varsigma < 0.707$ the poles of the transfer function are near the imaginary axis of the s-plane which can lead to resonance effects and overshoot in the transient response. A value of $\varsigma > 1$ produces an overdamped loop leading to sluggish behaviour of the transient response. A value of $\varsigma = 0.707$ has been used in the loop design for this project to ensure a reasonable trade-off between overshoot and rise time of the response.

3.3.2.3 Loop Bandwidth

It can be observed from the amplitude responses that $H(s)$ performs a low-pass filtering operation on the phase modulation of the input signal and $E(s)$ performs a high-pass filtering operation. This behaviour makes sense if we consider the limitation of the OPLL circuit. The loop can only respond to phase changes up to a certain rate, i.e. it has a limited bandwidth. This means that the loop will track phase changes that occur within the loop bandwidth and adjust the slave laser accordingly, and will fail to track phase changes that occur outside the loop bandwidth, that is, changes that occur too quickly for the loop to respond. The error response is the opposite. Phase changes inside the loop bandwidth are tracked with little error, and changes outside the loop bandwidth are not tracked at all, i.e. the error is extremely large.

The bandwidth of the loop can be defined in a number of ways. The most obvious might seem to be to simply take the natural frequency, ω_n, as the loop bandwidth. However, a look at Fig. 3.8 shows that the bandwidth actually has a strong dependence on the

damping factor, ς. Fig. 3.10 shows that K is actually a good indicator of the corner frequency of $H(s)$. Therefore, K is taken as the definition of the loop bandwidth [73].

3.4 Frequency Discriminator

Achieving both a large loop bandwidth and wide capture range in an OPLL places strict requirements on the feedback loop design. If it were possible to use a simpler circuit to provide the initial pull-in of the beat signal and track the center frequency, this would greatly reduce the demands on the phase-lock circuit and allow a simplified, moderate bandwidth PLL circuit to be used [75]. One method to minimize the frequency deviations between two free-running laser diodes is to use a frequency discriminator [76].

The schematic of a delay-line frequency discriminator applied to two heterodyned lasers is shown in Fig. 3.12.

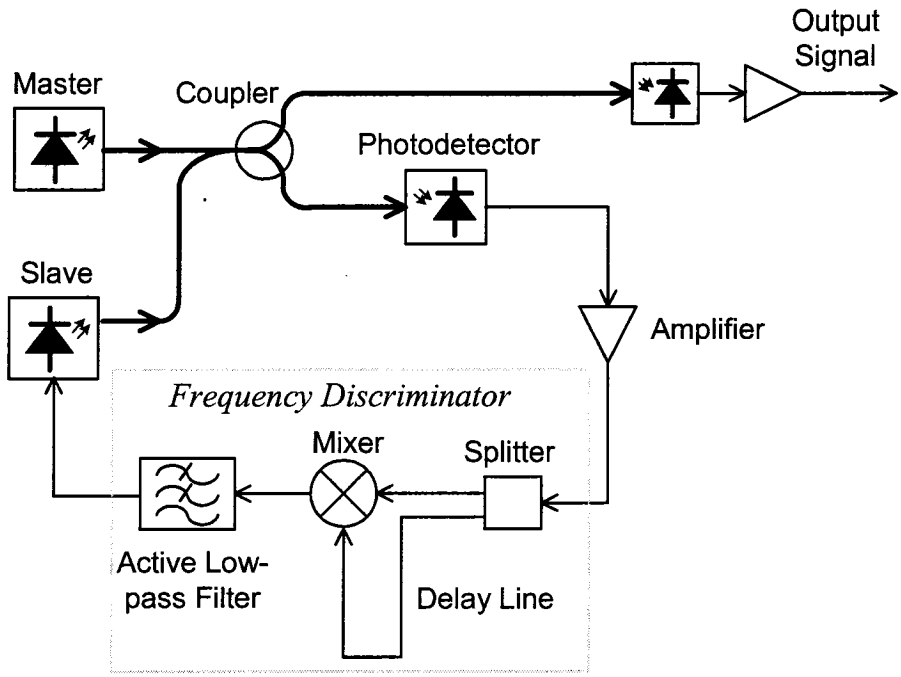

Fig. 3.12. A delay-line frequency discriminator applied to two heterodyned laser diodes.

The outputs of the master and slave laser are combined and a PD recovers the heterodyned beat signal in the feedback path of the setup. This microwave signal is then amplified and applied to the frequency discriminator which produces a DC correction signal proportional to the difference between the beat frequency and a fixed reference frequency, with the reference value being dependent on the discriminator design. This error signal is then filtered and fed back to the slave laser to adjust its output frequency and, thus, track the frequency changes that occur in the master laser.

The frequency discriminator implementation used in this research project has a microwave delay line configuration. The beat signal, v_i, after recovery by the PD and amplification, is split into two equal parts, v_1 and v_2, by a microwave power divider. The signal, v_1, is sent directly into a microwave mixer, while the other half, v_2, experiences a

time delay, τ, after propagation along a delay line, before entering the mixer. This setup is depicted in Fig. 3.13.

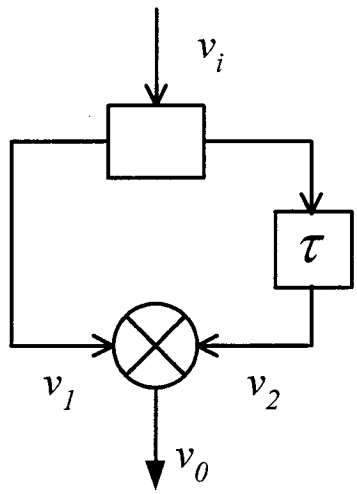

Fig. 3.13. Frequency discriminator configuration.

The signals, v_1 and v_2, can be represented as

$$v_1 = v_i \cos \omega t \tag{3.24a}$$

$$v_2 = v_i \cos \omega (t + \tau) . \tag{3.24b}$$

The output of the mixer, v_0, can be expressed as

$$v_0 = k_m v_1 v_2 = \frac{k_m}{4} v_i^2 \left(\cos \omega\tau + \cos(2\omega t + \omega\tau)\right) \tag{3.25}$$

where k_m is the mixer loss. The 2ω term in the expression is eliminated by the feedback filter, therefore, the term of interest is $\cos\omega\tau$, a sinusoidal DC feedback signal with nulls occurring as defined by

$$\omega\tau = (2i+1)\frac{\pi}{2}, \tag{3.26}$$

where i = ..., -1, 0, 1, ...

Considering any two consecutive nulls, the frequency spacing between these nulls can be shown to be

$$\begin{aligned} \omega_i - \omega_{i-1} &= \frac{2\pi}{2\tau}, \\ 2\pi(f_i - f_{i-1}) &= \frac{2\pi}{2\tau}, \\ \Delta f &= \frac{1}{2\tau}. \end{aligned} \tag{3.27}$$

(3.27) illustrates that changing the time delay, τ, i.e. changing the length of the delay line, will vary the position and spacing of the nulls. Fig. 3.14 shows the simulated shape of a delay-line discriminator response.

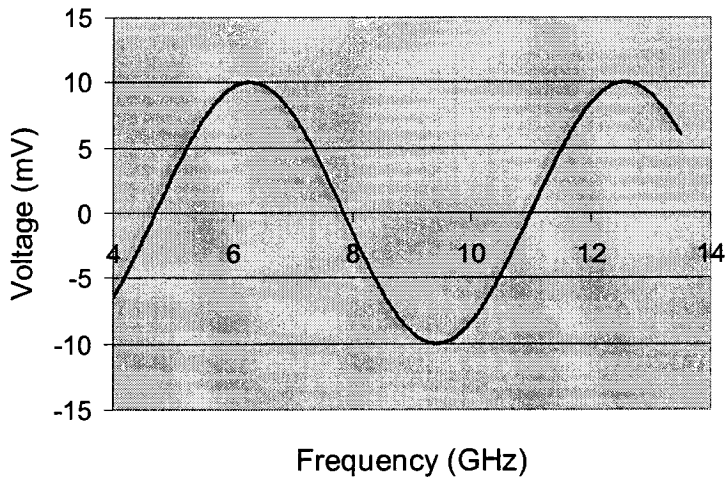

Fig. 3.14. Sinusoidal frequency discriminator response.

The operating point of the discriminator can be selected to be either of the nulls. Assuming a null on a positive-going slope is selected – if the incoming beat frequency is above the null, then a positive DC signal is produced proportional to the magnitude of the displacement from the null frequency; if the beat frequency is below the null a negative DC signal is produced. Sending this control signal back to the slave laser compensates for any master laser frequency deviations and maintains a stable microwave output. Operation on a negative-slope null simply requires a polarity change of the feedback, either by directly inverting the signal or switching the feedback to the other laser.

The null spacing of the frequency discriminator characteristic can be seen as its capture range. When the incoming signal frequency is above one of the extrema (peak or trough), the output is pulled to the higher null, if it is below an extrema, the output is pulled to the lower null. A long delay line has closely spaced nulls and many possible operating points, whereas a short delay line has widely spaced nulls and a large capture range.

3.5 Delay and Linewidth Considerations

The linewidth of an optical source used in an OPLL plays a key role in the implementation. The coherence time, τ_c, of a laser is related to its linewidth, $\Delta\nu$, by the following relation [77]

$$\tau_c \Delta\nu \geq \frac{1}{4\pi}. \tag{3.28}$$

Coherence time is, basically, the duration over which the phase of a laser does not change; the broader the linewidth, the shorter the coherence time. This directly affects the architecture of an OPLL since the loop must detect the phase difference between the lasers and propagate the corrective feedback signal through the opto-electronic path to the slave laser before a change in coherence occurs [77]. As stated earlier, this makes the loop propagation delay, τ_d, a critical parameter. As an example, consider a semiconductor laser with a linewidth of 2 MHz. Its coherence time is approximately 40 ns. The feedback loop must respond in a shorter time than this if the loop is to maintain a phase-lock.

In fact, the maximum delay allowed for reliable phase-lock loop operation is much shorter than the coherence time of the laser [47], [78]. Fig. 3.15 shows the relationship between the loop propagation delay and the summed laser linewidth. This figure indicates that to avoid degradation in loop performance with a summed laser linewidth of 2 MHz, the maximum delay time allowed is approximately 1 ns.

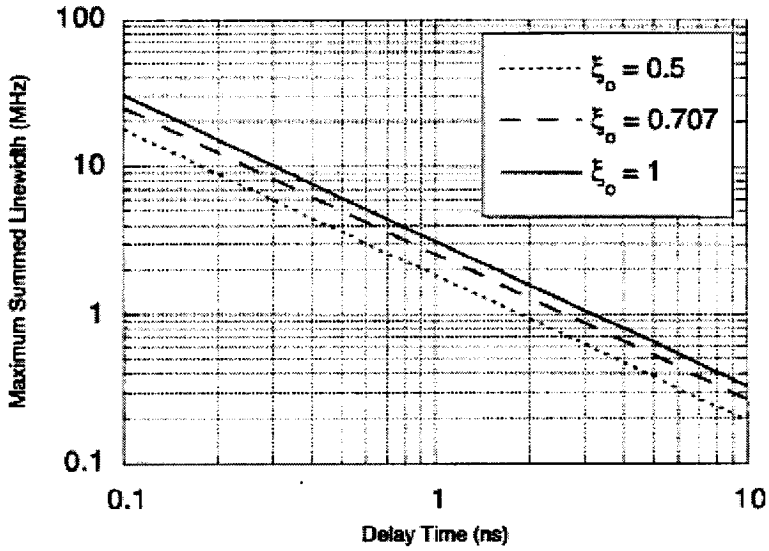

Fig. 3.15. Maximum summed linewidth versus time delay for a second-order type 2 OPLL [47].

3.5.1 External Cavity Lasers

One way to ease this very stringent requirement on the loop delay then, is to use laser diodes with very narrow linewidths. An ECL, which has an inherently narrow linewidth, is one possible light source that can be used.

An ECL is a laser that has an inline grating placed outside the cavity of a conventional laser diode. An anti-reflection coating is applied to the laser output face to suppress the normal cavity resonance. A longer cavity is now formed between the gain medium and the grating. The longer cavity and frequency selective nature of the grating form a laser diode with significantly narrower linewidth than a conventional laser diode [79]-[81].

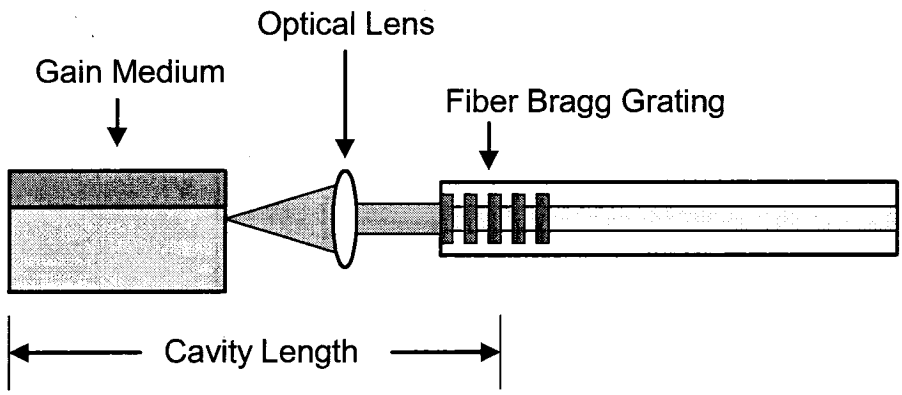

Fig. 3.16. External cavity laser with an inline fiber Bragg grating.

3.6 Summary

This chapter introduced several techniques of optically generating microwave signals for RoF applications, including direct detection and remote heterodyning techniques. It also presented a theoretical overview of the concept of optical heterodyning. The transfer functions of an OPLL were derived, along with its operating parameters. This chapter also introduced the operation of a delay-line frequency discriminator. It discussed the effects of laser linewidth on OPLL performance and the use of an ECL to ease the restrictions that loop delay places on OPLL operation.

Chapter 4

OPLL DESIGN AND PERFORMANCE

The frequency down-conversion module implemented in the discriminator-aided OPLL is presented in this chapter, along with an analysis of its contribution to the phase noise of the system. The frequency discriminator redesign and calibration are outlined and the performance is analyzed. This chapter also presents the performance achieved by the discriminator-aided OPLL with down-conversion.

4.1 Frequency Discriminator-aided Optical Phase-Lock Loop

The modules discussed in Chapter 3 – the OPLL, the frequency discriminator and the external cavity lasers – are the constituent components of the frequency discriminator-aided OPLL implemented in this research project. The original system was developed at CRC by the Microwave Photonics Group. Its performance was presented in [77].

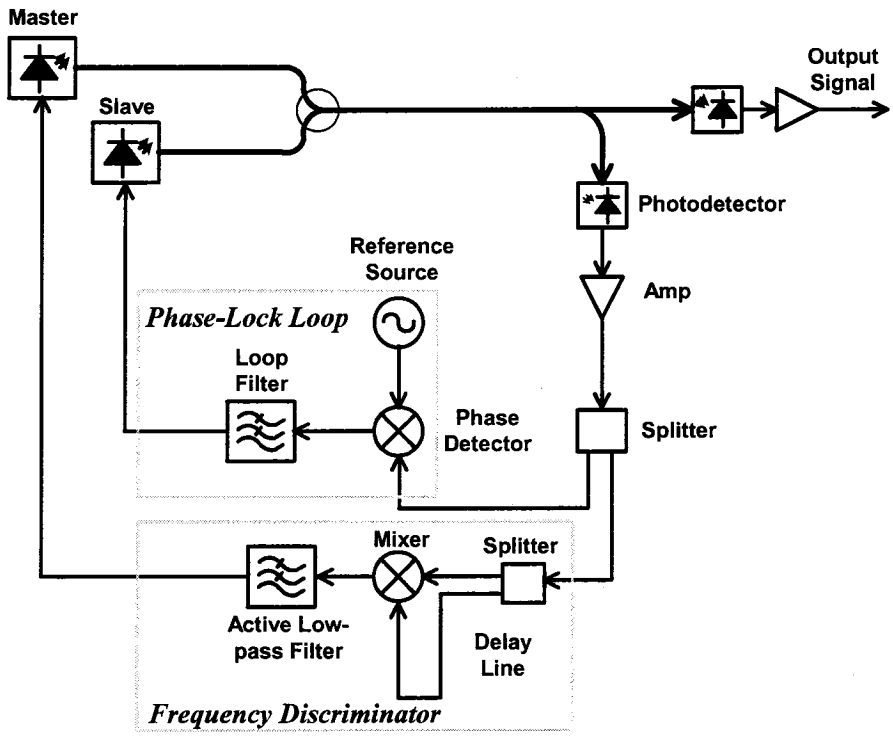

Fig. 4.1. OPLL implemented at CRC.

The goal of this system is to maintain a specific frequency difference between the master and slave lasers, a function provided by the delay-line discriminator, as well as narrow the inherent linewidth of the laser diodes, a function realized by the phase-lock portion of the circuit. A graphical illustration of this is shown in Fig. 4.2.

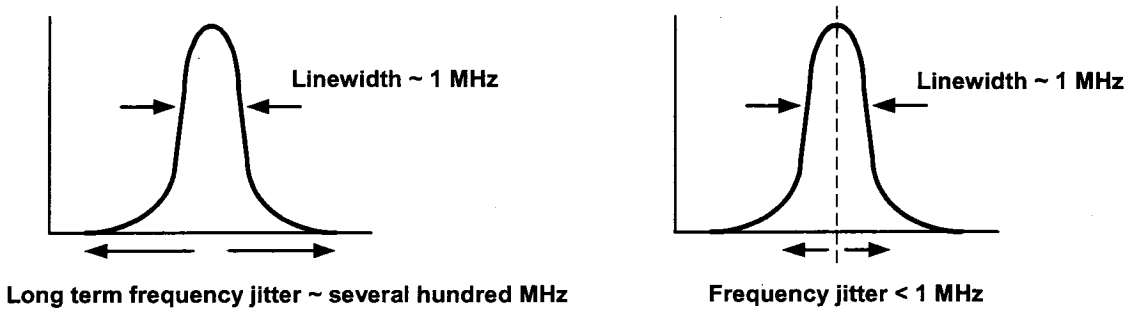

(a) Free-running lasers

(b) Discriminator-locked lasers

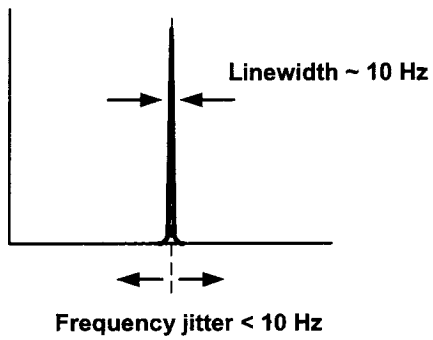

(c) Discriminator-aided phase-locked lasers

Fig. 4.2. Frequency stabilization and linewidth reduction by a discriminator-aided OPLL.

Several factors led to the eventual redesign of the original system configuration. The first was the desire to further integrate the feedback electronics. The original system was built using mainly discrete components, as can be seen in Fig. 4.3.

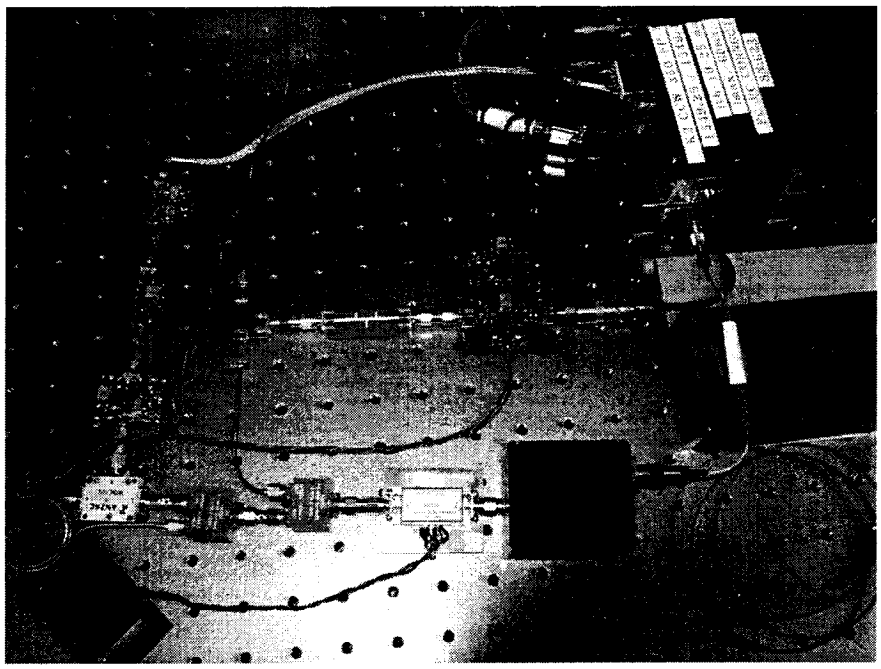

Fig. 4.3. Original OPLL configuration using discrete components.

The only components that had been integrated on a dielectric circuit board were the loop filters and the transconductance amplifiers (whose operation will be discussed in Section 4.1.3.4). One of the reasons for this was the fact that the operating frequency of the loop was 11.2 GHz. At this frequency it is difficult to find the surface mount microwave mixers, power splitters and amplifiers required. It is also difficult, at this frequency, to properly implement the microwave delay line required by the delay-line discriminator on a circuit board. For these reasons, discrete components, including a coaxial delay line, were used. A method for operating these components at a lower frequency would allow them to be integrated onto a single circuit board, as well as reduce the cost of the system.

Another factor that led to the changes of the original OPLL system was the discrete operating nature of the frequency discriminator. As discussed in Section 3.4, the delay-

line discriminator is limited to operate at discrete points, corresponding to the nulls determined by the delay line length. The best result possible for such a system, with regard to the number of operating points available, is a series of very closely spaced nulls created by using a long delay line. However, this still excludes the possibility of true continuous tuning of the microwave output frequency. For these reasons it was decided to modify the OPLL system with the addition of a frequency down-conversion module.

4.1.1 OPLL with Frequency Down-Conversion

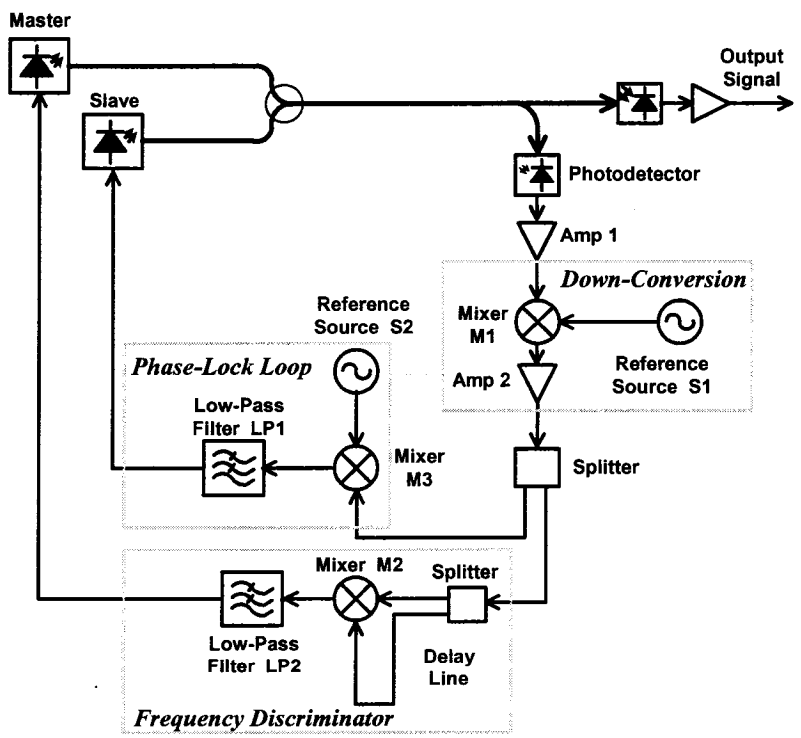

Fig. 4.4. Discriminator-aided OPLL with a frequency down-conversion module.

The frequency down-conversion module, added to the system after the photodetector, consists of a high frequency reference source S1, an electrical mixer M1 and an additional amplifier [82]. The entire circuit is shown in Fig. 4.4.

The inclusion of the down-conversion module allows both the PLL and the frequency discriminator to operate at a much lower, fixed frequency of the designer's choice. The down-conversion module mixes the input beat frequency down to a lower value determined by its offset from S1. For example, in order to generate a microwave signal at 11.2 GHz, S1 can be chosen to operate at 12 GHz, which will reduce the feedback signal down to 800 MHz. This allows the phase-lock circuit, the low-frequency reference source S2, and the frequency discriminator to operate at 800 MHz where relatively inexpensive, surface-mount components are readily available. S2 also now has the potential to be implemented on-board as a low-noise crystal oscillator.

Another benefit offered by this design is the ability to continuously tune the microwave output frequency. In the new configuration, by simply changing the frequency of S1, the frequency discriminator and the phase detector work together to change the wavelength spacing between the two laser diodes to maintain the fixed frequency of 800 MHz at the output of the frequency down-conversion module. Thus, in this setup, tuning S1 will result in an equal shift in the output frequency.

One disadvantage of adding the high-frequency source is the introduction of additional phase noise to the system. Following a similar derivation as in [47], the additional phase noise contributed by S1 can be theoretically determined.

4.1.2 Phase Noise Analysis

The purpose of this analysis is to determine the nature of the contribution of the added source S1 to the overall phase noise of the system. In this analysis it is assumed that the frequency discriminator does not contribute significantly to the phase noise at the output. This assumption is justified by the fact that the discriminator is designed to act only on the frequency error between the incoming signal and its set point and does not respond to the more quickly varying phase error [83]. Also, once the system is phase-locked the frequency is highly stable, under this condition, the frequency discriminator design indicates that its output is practically zero and therefore, will not affect the beat signal.

Using the expressions derived in Section 3.3.1 and referring to Fig. 4.4, the slave laser output can be expressed, in the time domain, as

$$\frac{d\phi_s(t)}{dt} = K_o K_f K_d [\sin\theta(t) + n'(t)] * f(t) * \delta(t - \tau_d) \tag{4.1}$$

where $f(t)$ represents the impulse response of the loop filter, $\delta(t-\tau_d)$ represents the loop propagation delay, and $n'(t)$ is the photodetector shot noise [47]. K_o, K_f, and K_d are as defined in Section 3.3.1. $\theta(t)=\phi_{ms}(t)-\phi_d(t)-\phi_r(t)$ is the phase error at the output of the phase detector, and $\phi_{ms}(t)=\phi_m(t)-\phi_s(t)$.

It is assumed that the master laser electric field, $E_m(t)$, the slave laser electric field, $E_s(t)$, S2's output voltage, $v_r(t)$, and S1's output voltage, $v_d(t)$, are given by, respectively

$$E_m(t)=E_{mo}e^{j[\omega_m t+\phi_m(t)]} \tag{4.2a}$$

$$E_s(t)=E_{so}e^{j[\omega_s t+\phi_s(t)]} \tag{4.2b}$$

$$v_r(t)=A_r\cos[\omega_r t+\phi_r(t)] \tag{4.2c}$$

$$v_d(t)=A_d\cos[\omega_d t+\phi_d(t)] \tag{4.2d}$$

where E_{mo} (V/m), E_{so} (V/m), A_r (V), and A_d (V) are the amplitudes, ω_m, ω_s, ω_r, and ω_d are the angular frequencies (rad/s) and $\phi_m(t)$, $\phi_s(t)$, $\phi_r(t)$, and $\phi_d(t)$ are the phases (rad) of the master and slave lasers, and S2 and S1, respectively. The phase terms can be expressed as

$$\phi_m(t)=\phi_{mo}+\gamma_m(t) \tag{4.3a}$$

$$\phi_s(t)=\phi_{so}+\gamma_s(t) \tag{4.3b}$$

$$\phi_r(t)=\phi_{ro}+\gamma_r(t) \tag{4.3c}$$

$$\phi_d(t)=\phi_{do}+\gamma_d(t) \tag{4.3d}$$

where $\phi_{mo}, \phi_{so}, \phi_{ro}$, and ϕ_{do} are the quiescent phases and $\gamma_m(t), \gamma_s(t), \gamma_r(t)$, and $\gamma_d(t)$ are the phase fluctuations of the master laser, slave laser, and S2 and S1, respectively.

Assuming that the phase error, $\theta(t)$, is small enough to allow linearization of the system (i.e. $\sin\theta(t) \approx \theta(t)$), the closed-loop transfer function, as in (3.13), is given as

$$H(s) = \frac{\phi_s(s)}{\theta(s) + \phi_s(s)} = \frac{K_0 K_f K_d F(s) e^{-s\mathrm{T}_d}}{s + K_0 K_f K_d F(s) e^{-s\mathrm{T}_d}} \tag{4.4}$$

where the photodetector shot noise term, $n'(t)$, has been neglected.

The phase difference between the master and slave lasers and the phase error at the output of the phase detector are, respectively

$$\phi_{ms}(t) = \phi_{mo} - \phi_{so} + \gamma_m(t) - \gamma_s(t) \tag{4.5}$$

$$\theta(t) = \phi_{mo} - \phi_{so} - \phi_r(t) - \phi_d(t) + \gamma_m(t) - \gamma_s(t)\,. \tag{4.6}$$

In (4.5) and (4.6), ϕ_{so} is controlled by the loop, according to (4.1), to compensate for the phase fluctuations in the system. Therefore, using the closed-loop transfer function, *H(s)*, the Laplace transforms of $\phi_{ms}(t)$, and $\theta(t)$ are

$$\phi_{ms}(s) = [1 - H(s)][\Gamma_m(s) - \Gamma_s(s)] - H(s)[N'(s) - (\phi_d(s) + \phi_r(s))] \tag{4.7}$$

$$\theta(s) = [1 - H(s)][\Gamma_m(s) - \Gamma_s(s) - (\phi_d(s) + \phi_r(s))] - H(s)N'(s) \qquad (4.8)$$

where $\Gamma_m(s)$, $\Gamma_s(s)$, and $N'(s)$ are the Laplace transforms of $\gamma_m(t)$, $\gamma_s(t)$ and $n'(t)$, respectively.

From (4.7) and (4.8), we see that the phase term from S1 simply combines additively with the phase term of S2. Therefore, the addition of the down-conversion module results in an additive phase noise contribution by S1 to the overall phase noise in the system.

4.1.3 Frequency Discriminator Redesign

With the down-conversion module in place, the frequency discriminator can be redesigned to take advantage of the lower operating frequency and integrate more of the components onto a single circuit board. A delay-line discriminator is still used, except, instead of an external, coaxial delay line, an on-board microstrip delay line is used. Even though this discriminator design is still limited to discrete operating points, as discussed above, the down-conversion module provides the continuous tunability desired.

At the reduced operating frequency, it was possible to incorporate the power splitter, the delay line, the microwave mixer, the active low-pass filter and the transconductance amplifier onto a single circuit board.

4.1.3.1 Power Splitter

In the first iteration of the new frequency discriminator circuit design, a simple surface mount, packaged power splitter was used (Model #: LRFPX). There were indications during the initial testing of the circuit that the splitter did not interact well with the other components on the circuit board and oscillations appeared in the output. In addition, the response of the splitter rolled off very close to 1 GHz as shown in Fig. 4.5.

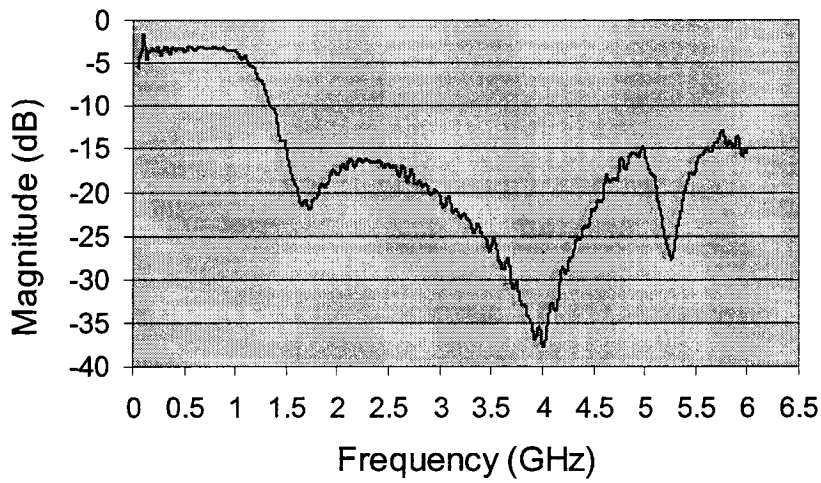

Fig. 4.5. Forward transmission response (S21) for one output port of the packaged surface-mount splitter (LRFPX).

Ideally, the design requires a splitter response with roll-off in the 1.5-2 GHz range, since the upper operating frequency limit of the mixer is 1.3 GHz. This would ensure that the splitter did not impose an additional bandwidth restriction.

A resistive splitter implementation was then considered. However, this type of design has at least 6 dB of loss – 3 dB from the power splitting itself and an additional 3 dB from the resistive nature of the network. A reactive splitter, however, has, in the ideal case, only a 3 dB splitting loss. Therefore, it was decided to implement the microwave power divider as a Wilkinson reactive power splitter using surface mount components. The schematic of this design is shown in Fig. 4.6.

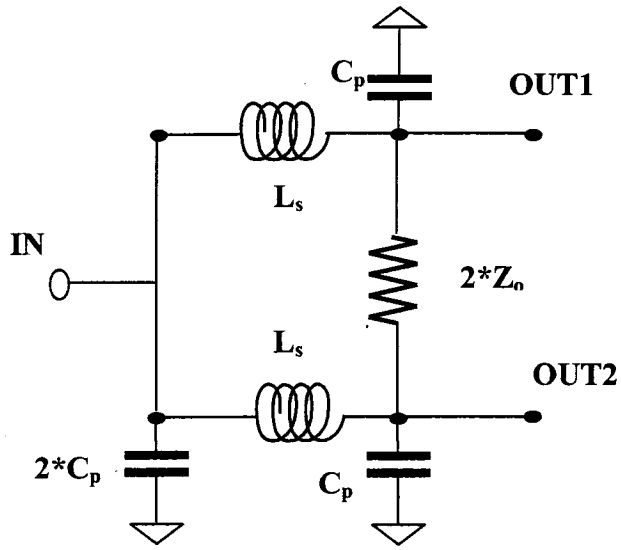

Fig. 4.6. Wilkinson reactive power splitter.

The component values can be calculated by the following relations

$$C_p = \frac{1}{2\pi f_0 Z_0} \tag{4.9a}$$

$$L_s = \frac{Z_0}{2\pi f_0} \tag{4.9b}$$

where Z_0 is the characteristic impedance at the output, and f_0 is the cut-off frequency.

In this case, the circuit is designed for a characteristic impedance of 50 Ω and a cut-off frequency of 1.5 GHz. This leads to calculated values of C_p = 2.12 pF and L_s = 5.31 nH. The actual inductor value was chosen as L_s = 5.6 nH, since this was the closest standard value available near 5.31 nH. The actual capacitor value was chosen as C_p = 1.5 pF to compensate for the slightly different inductor value and, also, to push the splitter cut-off frequency as high as possible while maintaining a smooth passband. The designed splitter's magnitude and phase responses are shown in Figs. 4.7 and 4.8.

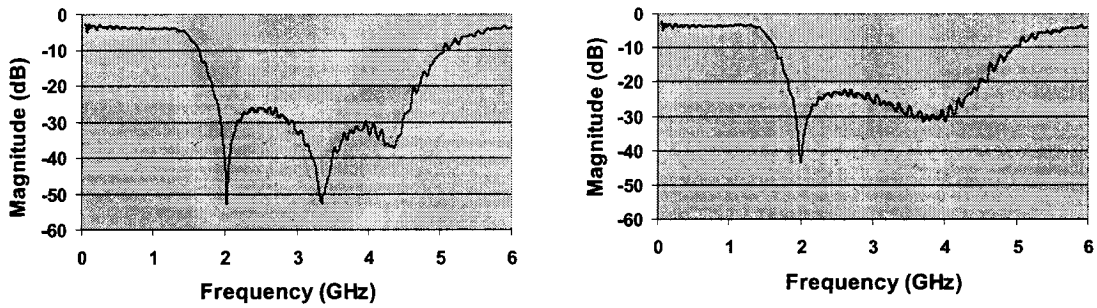

(a) Port 1 (b) Port 2

Fig. 4.7. Magnitude response of Wilkinson reactive splitter.

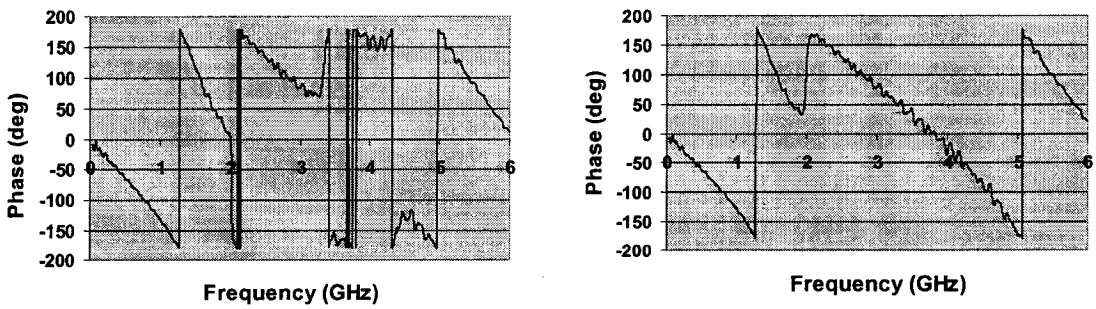

(a) Port 1 (b) Port 2

Fig. 4.8. Phase response of Wilkinson reactive splitter.

It can be seen that this power splitter performs very well. The magnitude response of each port shows little ripple with a splitting loss very close to the ideal 3 dB, and the passbands roll off smoothly at about 1.5 GHz as designed. The phase response of each port shows a linear phase within the passband region. Comparing this with Fig. 4.5, it can be seen that the Wilkinson splitter exhibits a better response than the LRFPX packaged model.

4.1.3.2 Microstrip Delay Line

The microstrip delay line is designed such that the spacing between nulls is 1 GHz. Based on the design formula from (3.27), the time delay required to give this null spacing is $\tau = \frac{1}{2\Delta f} = 0.5\,\text{ns}$. The circuit board used to implement the microstrip line is a standard FR-4 board with a dielectric constant of ε_r = 4.0 at 1 GHz. The length of microstrip required to give this amount of delay is

$$L = \tau \cdot v = (0.5\,\text{ns})(1.73 \times 10^8\ \text{m/s}) = 8.66\,\text{cm} \tag{4.10}$$

where $v = \frac{c}{\sqrt{\varepsilon_{eff}}}$ is velocity of the electromagnetic field on the FR-4 board.

The first version of the frequency discriminator board (R1) was designed with additional microstrip extensions that could be used to slightly adjust the length of the delay line. This would allow some small adjustments to be made to the position of the discriminator

null operating point, if required. A schematic of the R1 layout is shown in Fig. 4.9, which includes the surface mount LRFPX power splitter.

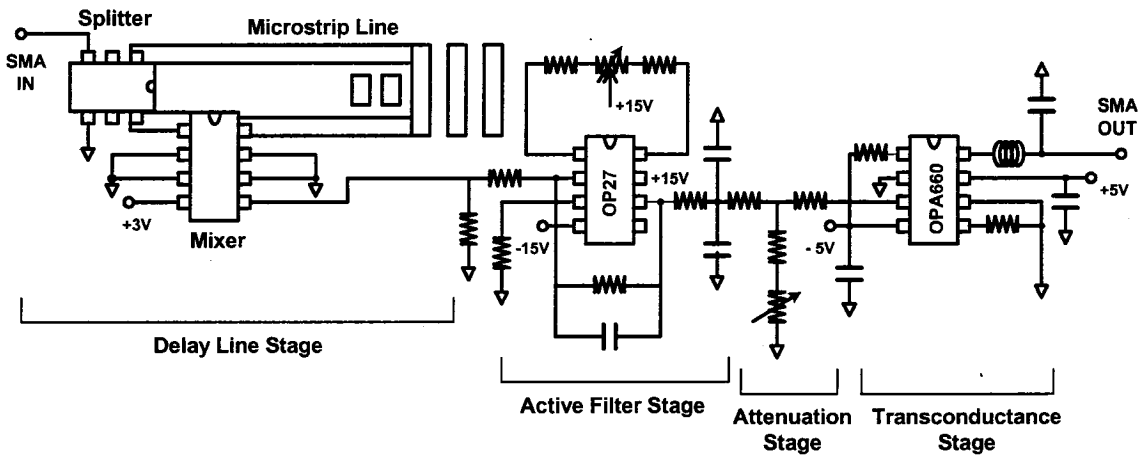

Fig. 4.9. Revision 1 layout of redesigned frequency discriminator.

This board layout also included, in addition to the splitter and microstrip line, a double-balanced mixer, an operational amplifier, and a transconductance amplifier (TCA).

As the schematic illustrates, half the input signal is fed directly into the mixer and the other half is delayed by the microstrip line. The mixer output is then fed into an active low-pass filter, with gain provided by an op-amp, and, finally, this filtered signal is sent to a TCA where the voltage feedback signal is converted to a current signal. The function of the active filter and TCA will be discussed in detail in Sections 4.1.3.3 and 4.1.3.4.

As discussed, this first iteration presented problems when attempting to obtain a stable output signal. Several attempts were made to correct the problem by varying the length of

the delay line and changing the splitter to a different surface mount model. However, tests still showed oscillatory behaviour in the output. Figs. 4.10 (a) and (b) show two results obtained at the output of the delay line stage, i.e. at the mixer output port.

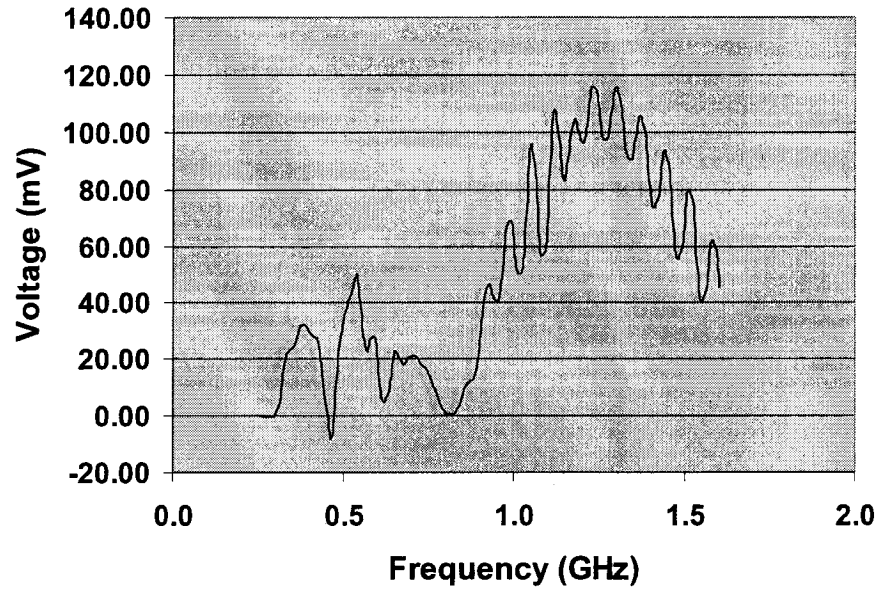

(a)

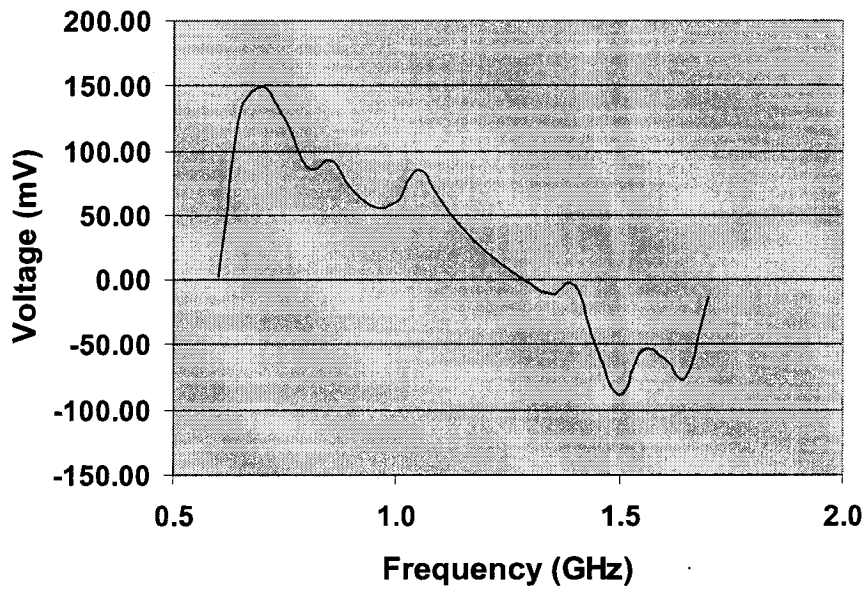

(b)

Fig. 4.10. Two examples of responses obtained with frequency discriminator R1.

Due to these poor results, testing of this circuit did not get past the delay line stage and the active filter and TCA were not implemented. It was decided to rearrange the board layout, paying particular attention to the grounding of the microstrip delay line and the mixer. The second version of the circuit (R2) is shown in Fig. 4.11.

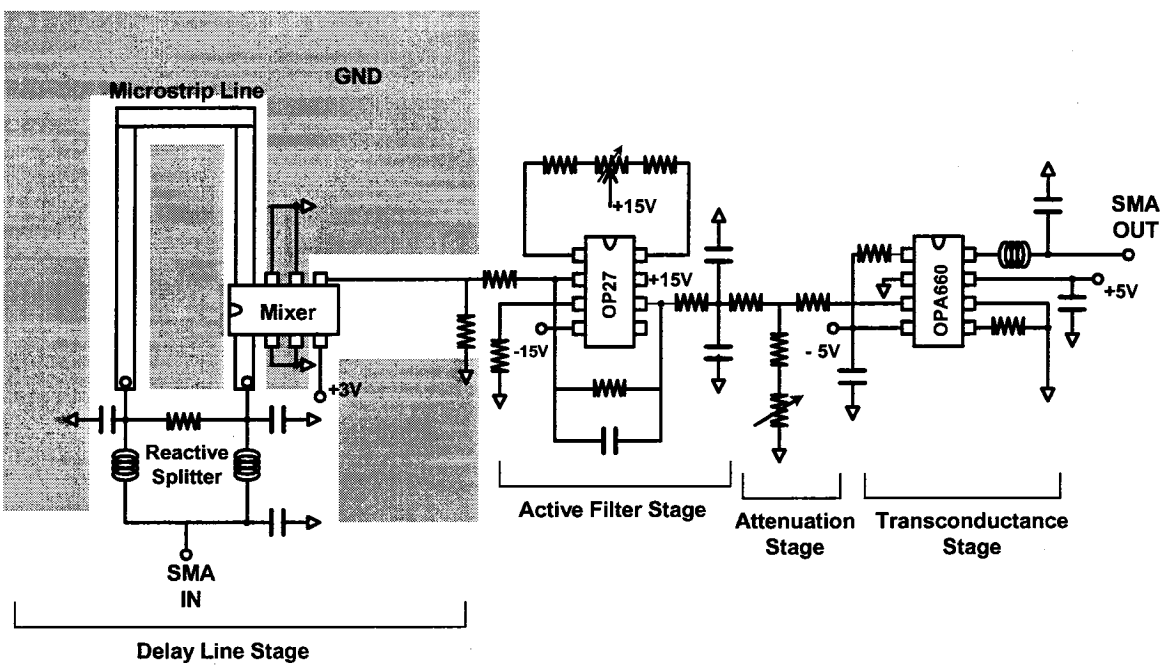

Fig. 4.11. Revision 2 layout of frequency discriminator circuit.

This schematic shows the more thorough grounding included for R2, in particular, beneath the mixer and between the microstrip lines to ensure the delay line and the mixer inputs are electrically isolated. R2 also used the Wilkinson power splitter described in Section 4.1.2.1, as well as a Hittite double-balanced mixer with a frequency range from 0.6 – 1.3 GHz. This mixer has an integrated LO amplifier, which requires power from a single +3V supply, and allows the LO input to be as low as 0 dBm.

The output signal of this design was much smoother than R1's response. Fig. 4.12 shows the mixer output obtained as the frequency input was varied from 0.55 GHz to 1.35 GHz.

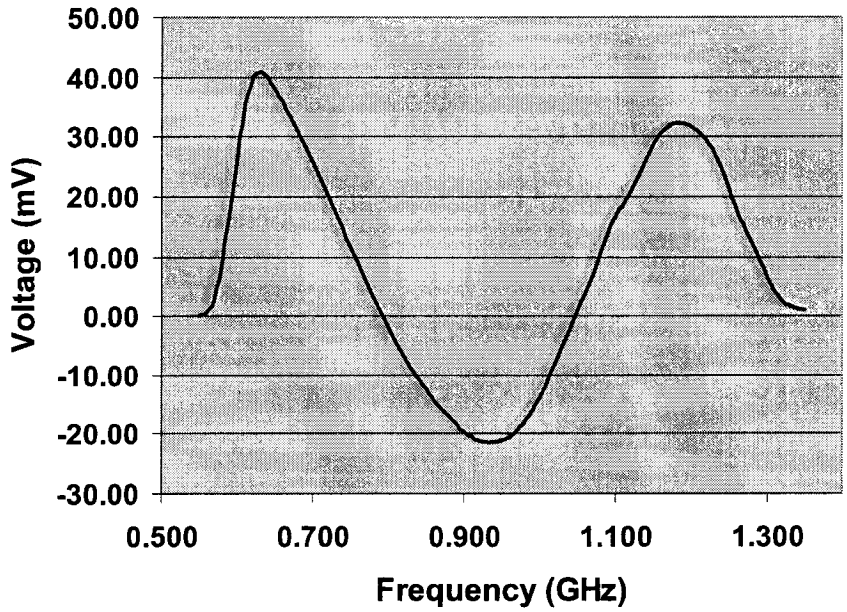

Fig. 4.12. Frequency discriminator response for R2 board layout.

The roll off at each end of the response can be attributed to approaching the frequency limits of the mixer (0.6 – 1.3 GHz). Two nulls are visible in this response; one at about 0.780 GHz and the other at 1.050 GHz. This is contrary to the designed null spacing of 1 GHz, which gives the expectation of a single null in this operating range. Simulations were performed with a Genesys-Eagleware microwave circuit design package in an attempt to explain this behaviour. Based on simulation, it is possible that interactions between the reactive networks of the power splitter and the mixer input ports, as well as small parasitic capacitances between components leads and board traces, could account for the additional crossing. The shape of the response around the 0.780 GHz null shows very linear behaviour and is a good candidate for the low-frequency locking point.

4.1.3.3 Active Low-Pass Filter

Once a suitable response was obtained from the delay line portion of the discriminator board, the op-amp was added to form an active low-pass filter whose purpose is to filter any high frequency components present in the feedback signal and provide precision amplification of the low-frequency (DC) signal level. The op-amp is an OP27 low-noise, high-speed amplifier. It is used in an inverting configuration with a theoretical gain of 56.2 kΩ/330 Ω = 45 dB and a theoretical cut-off frequency of $f_c \approx 30$ Hz.

The active filter includes an attenuation stage as well, which is simply a voltage divider network with a 2 kΩ potentiometer in the ground leg. This allows more precise control of the feedback level for the input to the TCA. The active filter output was measured at both minimum and maximum levels of attenuation to determine the DC feedback response as the frequency was varied from 0.55 GHz to 1.45 GHz.

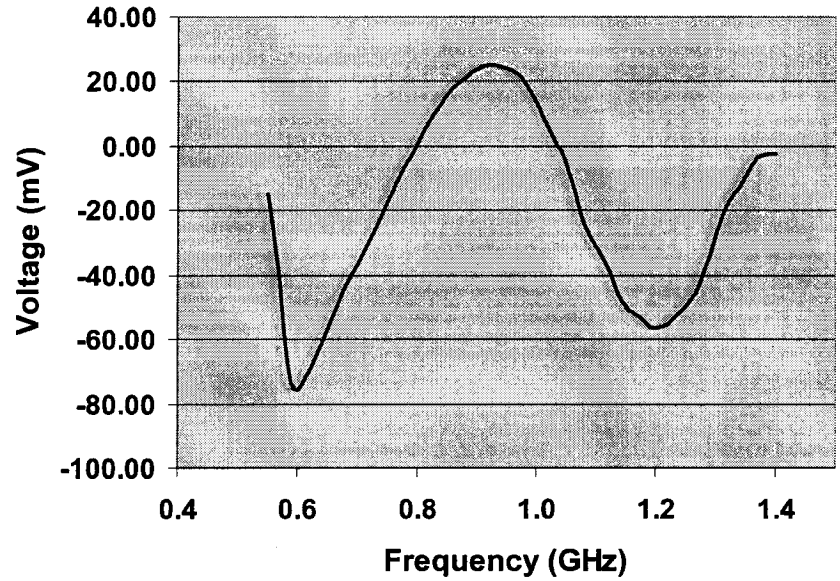

(a)

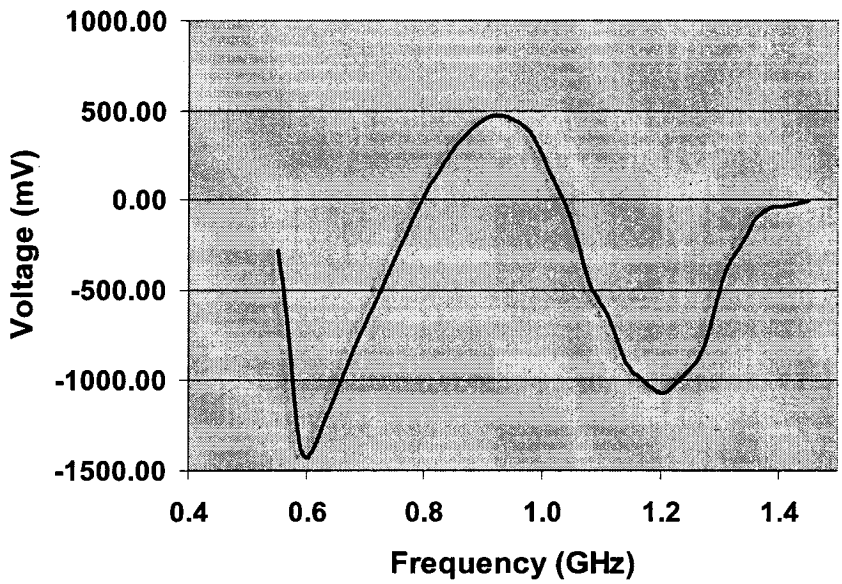

(b)

Fig. 4.13. Response of the frequency discriminator with the active filter and attenuation stage in place at (a) minimum output level; (b) maximum output level.

The amplification provided by the active filter is obvious from this figure, as is its inverting behaviour since the 780 MHz null crossing has now switched to a negative-positive transition.

Two parallel capacitors are also added after the op-amp in the active filter stage to form two low-pass passive filters with cut-offs at 1.5 kHz and 7.2 MHz. These filters further reduce any high frequency components that might still be present in the DC feedback signal.

4.1.3.4 Transconductance Amplifier

The amplified, filtered output from the active filter stage is then input to a TCA. The TCA converts the voltage signal into a current signal suitable for injection into the slave laser diode. The feedback acts to compensate for variations in the beat signal by providing a proportional current level to adjust the laser output in an opposite direction to the frequency deviation. The main drive current for the slave laser is provided by a constant-current source (ILX LDC-3724B) and is in the range of 30-80 mA.

The TCA used in this design is an OPA660, which is a bipolar, voltage-controlled current source. The OPA660 is self-biased and its transconductance level is controlled by an external resistor. This resistor can be used to calibrate the TCA response based on the gain of the other components.

4.1.3.5 Laser FM Response

Calibration of the frequency discriminator response requires the determination of the DC or low-frequency FM response of the laser diode used as the slave. This will indicate the magnitude of the feedback current required to change the output frequency of the laser diode by a fixed amount. The FM response can be determined by measuring the laser wavelength variation as a function of the control current. The data sheet for the ECLs gives this value as 1.1 pm/mA. The measured response is shown in Fig. 4.14.

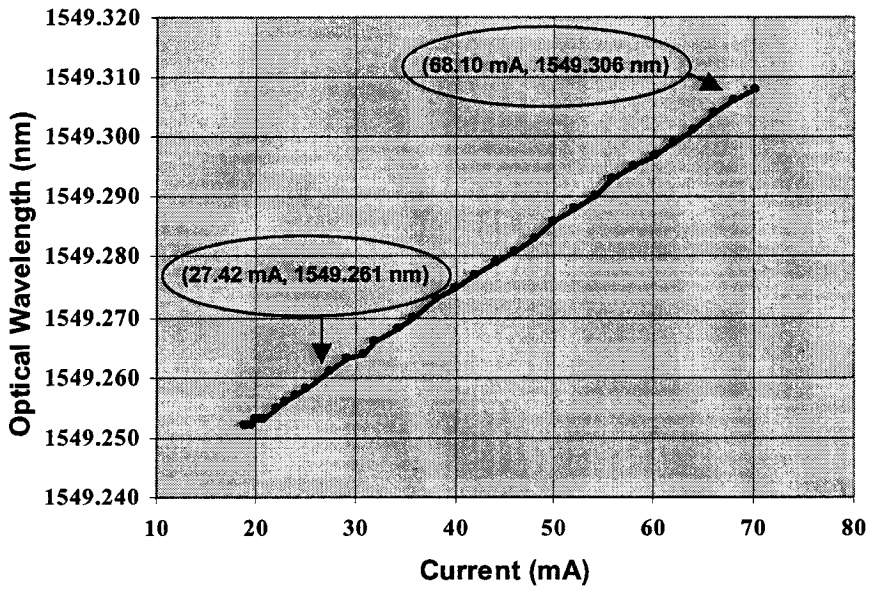

Fig. 4.14. Measured current tuning behaviour of K2 691 ECL.

The slope of this curve is calculated as

$$\frac{\Delta\lambda}{\Delta i} = \frac{1549.306 - 1549.261\,\text{nm}}{68.1 - 27.42\,\text{mA}} = 1.11\,\text{pm/mA}$$

which is in close agreement with the factory reported value.

The corresponding FM response can be determined from the relation

$$\frac{\Delta f}{\Delta i} = \frac{c}{\lambda^2}\frac{\Delta\lambda}{\Delta i}. \tag{4.11}$$

Using this expression, the frequency deviation as a function of current is calculated as $\frac{\Delta f}{\Delta i} = 138.5\,\text{MHz/mA}$. This value is then used to calibrate the TCA to provide the correct amount of transconductance for a given input voltage.

4.1.3.6 TCA Calibration

Based on the slope of the output plots of the active filter/attenuation stage, the minimum and maximum signal gain can be determined. They are calculated as $G_{\min} = 0.3567\,\text{mV/MHz}$ and $G_{\max} = 6.71\,\text{mV/MHz}$. Designing the circuit such that the

minimum input level provides the correct output current gives a transconductance value of $K_{TCA} = \frac{1}{(138.5\,\text{MHz/mA})(0.3567\,\text{mV/MHz})} = 20.2\,\text{mA/V}$.

This amount of transconductance can be provided by selecting the correct value of R_Q, the external control resistor for the TCA, based on the calibration plots provided on the data sheet; doing so gives a value of $R_Q = 2.7\ \text{k}\Omega$.

Fig. 4.15 shows the output response of the TCA as the input frequency to the circuit is varied from 0.55 GHz to 1.35 GHz.

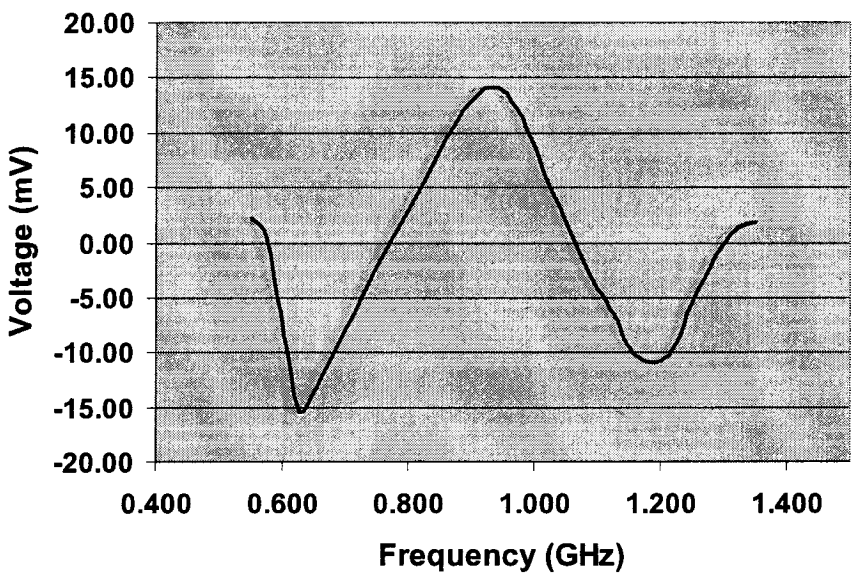

Fig. 4.15. Frequency discriminator response with TCA.

This response was obtained by measuring the voltage across a 7 Ω resistor, to emulate the input impedance of the laser diode, at the output of the frequency discriminator circuit. The DC current output of the TCA, then, is on the order of 2 mA. The response also

shows the linear, negative-positive transition around the 780 MHz null. This null is chosen as the new, low-frequency operating point for the OPLL.

4.1.3.7 Dielectric Board Layout

All components of the frequency discriminator circuit were mounted on an FR-4 dielectric board. The silkscreen of this board layout is shown in Fig. 4.16 and a picture of the actual board is shown in Fig. 4.17.

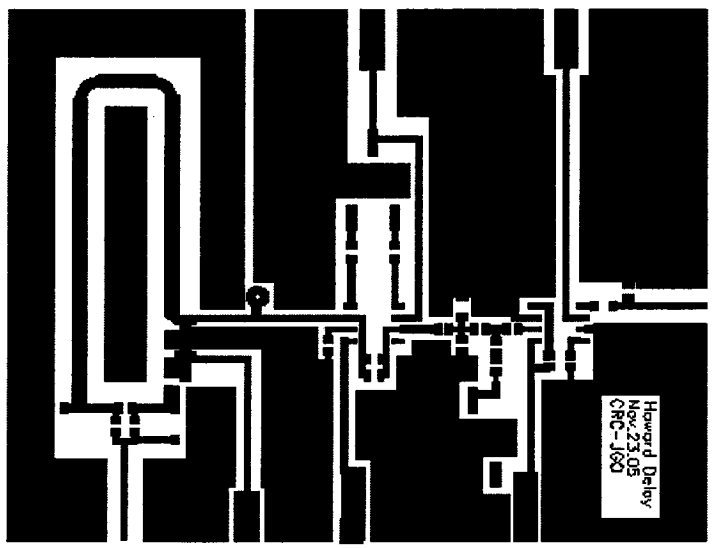

Fig. 4.16. Frequency discriminator board layout.

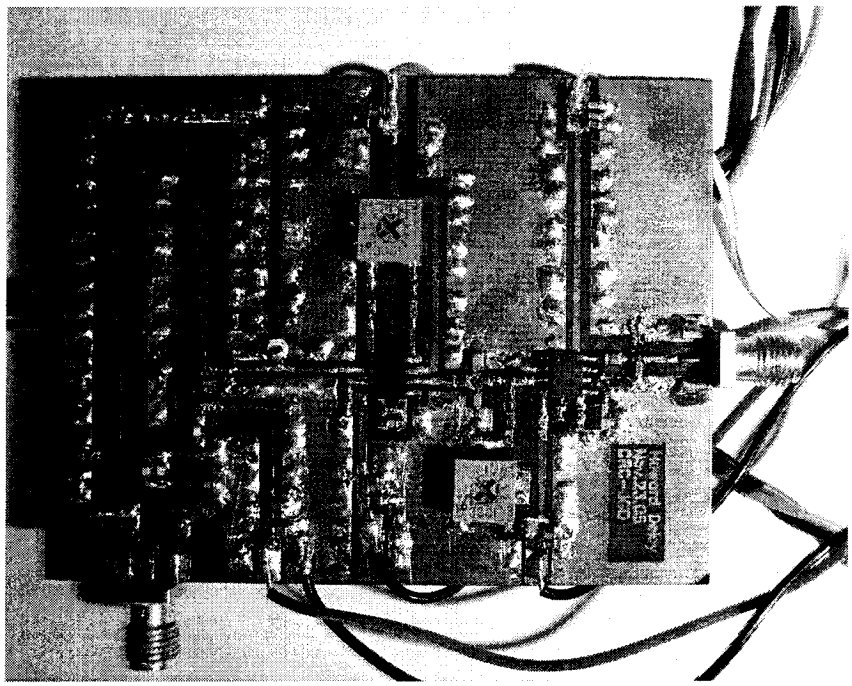

Fig. 4.17. Actual frequency discriminator board.

4.1.4 Frequency Discriminator Performance

Once the frequency discriminator circuit was completed and the calibration of the TCA finished, testing of its frequency-locking performance could be carried out. Small adjustments to the feedback levels, by tuning the on-board attenuator, were required to pinpoint the exact level necessary to frequency lock the two laser diodes. The results are shown in Fig. 4.18.

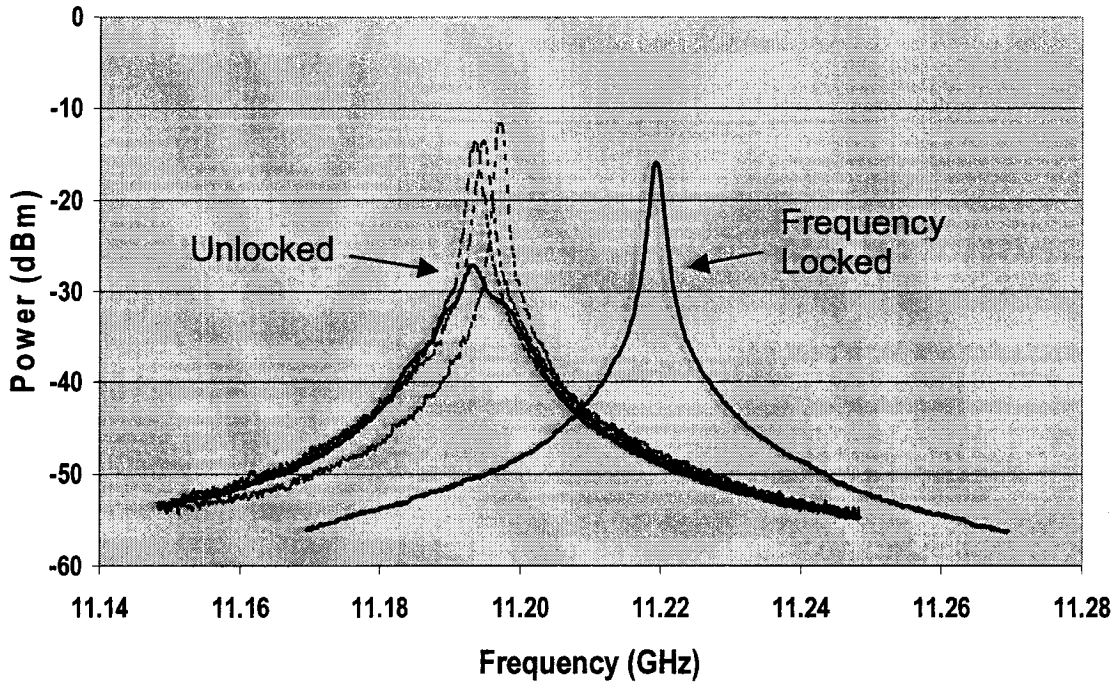

Fig. 4.18. Frequency locking result with the new integrated frequency discriminator; measurements taken every 30 seconds over an 8-minute span.

The figure shows the average of 16 traces without feedback, i.e. the unlocked state, and with feedback engaged, i.e. with a frequency lock at the 780 MHz null. The three dotted traces are individual measurements of the unlocked state. These measurements still produce a narrow linewidth signal; however, since the center frequency is drifting with time, their average produces the flat top curve shown. The improvement in signal quality and frequency stability with discriminator feedback is clear.

4.1.5 OPLL Performance with Down-Conversion Module

With the frequency discriminator re-designed and operating at a reduced frequency, the entire feedback loop can be tested with the down-conversion module in operation as discussed in Section 4.1.1.

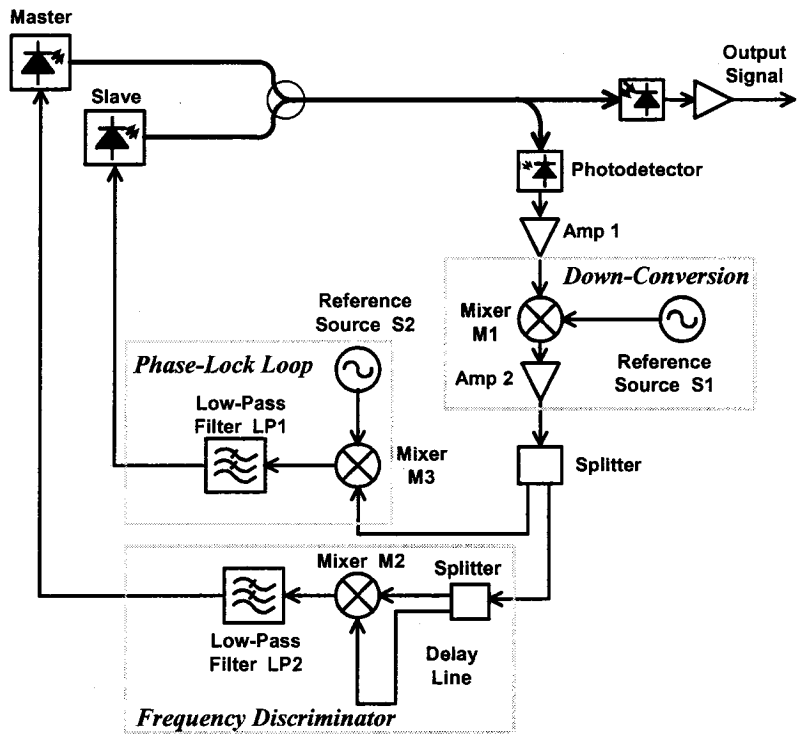

Fig. 4.3. Discriminator-aided OPLL with a frequency down-conversion module.

Referring to Fig. 4.3, which has been reproduced here for convenience, the feedback circuitry is engaged in the following sequence: first, each ECL is temperature stabilized by adjusting its thermoelectric cooler (TEC) temperature, and then the current is increased to induce lasing and set at approximately 50 mA. The temperature is adjusted slightly to bring the operating wavelengths of each ECL close to the other, such that their

beat frequency is near 11.22 GHz. A second photodetector is used to recover the signal from the output lead of the optical coupler and the beat frequency is monitored on a spectrum analyzer.

Next, the high-frequency reference source S1, is engaged at 12 GHz, and the beat signal, recovered by the feedback photodetector, is mixed down to around 780 MHz by M1 in the down-conversion module. The frequency discriminator circuit is then powered on and the down-converted signal is frequency locked to the 780 MHz operating point, which translates to a beat frequency lock at 11.22 GHz.

Once the frequency lock is established and the beat frequency is within the capture range of the phase-lock loop, the PLL circuit is powered on and the low-frequency reference source S2 is engaged at 780 MHz. The PLL circuit then attempts to narrow the linewidth of the output signal down to a value comparable to the linewidth of the reference source.

A picture of the actual discriminator-aided OPLL with the down-conversion module is shown in Fig. 4.19.

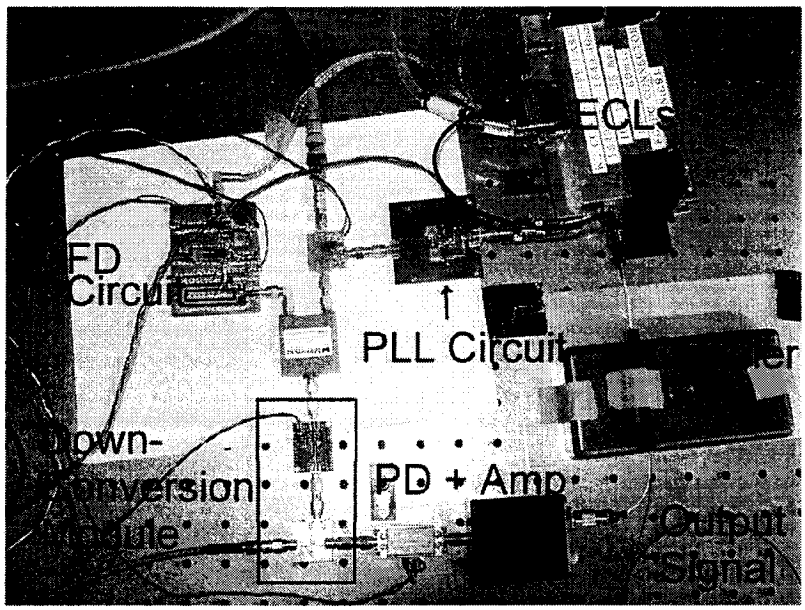

Fig. 4.19. Discriminator-aided OPLL setup with down-conversion module.

The quality of the output signal spectrum of the two heterodyned wavelengths is measured on a spectrum analyzer and the result is shown in Fig. 4.20 at several spans.

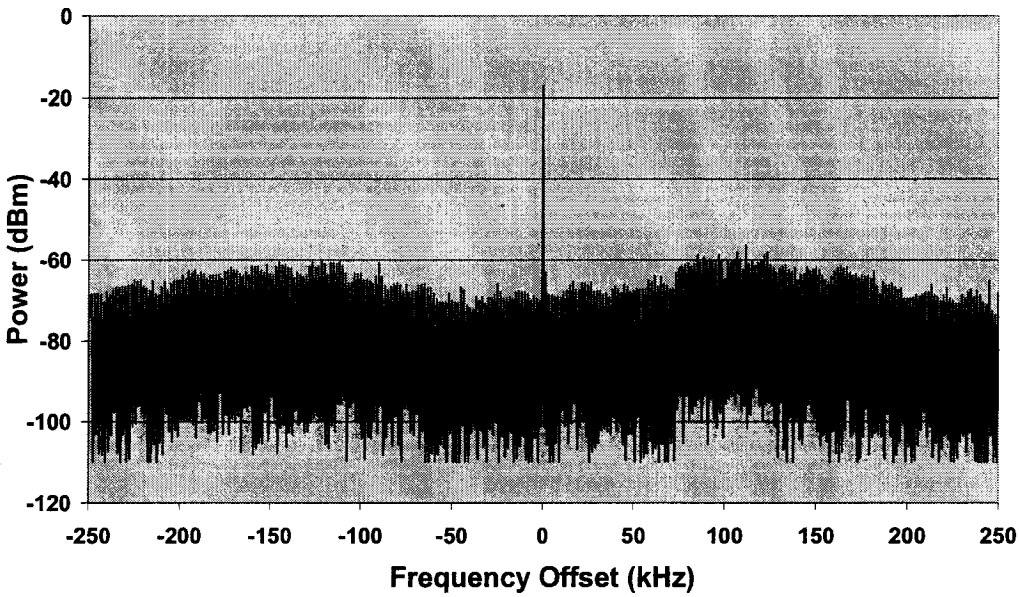

Fig. 4.20(a). Phase-locking result of OPLL with down-conversion at a span of 500 kHz.

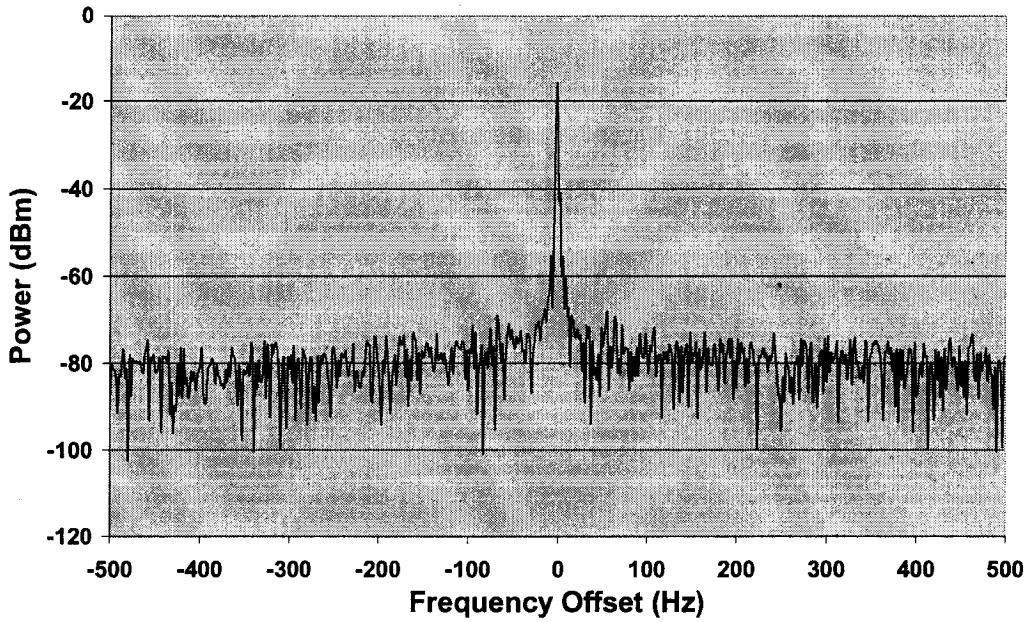

(b)

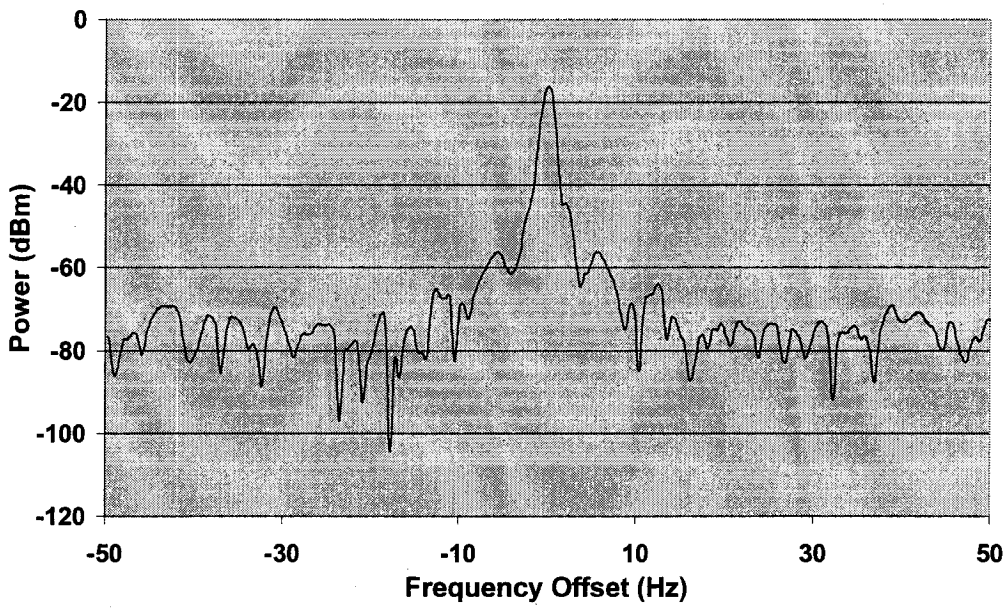

(c)

Fig. 4.20. Phase-locking results of OPLL with down-conversion at spans of (b) 1 kHz; and (c) 100 Hz.

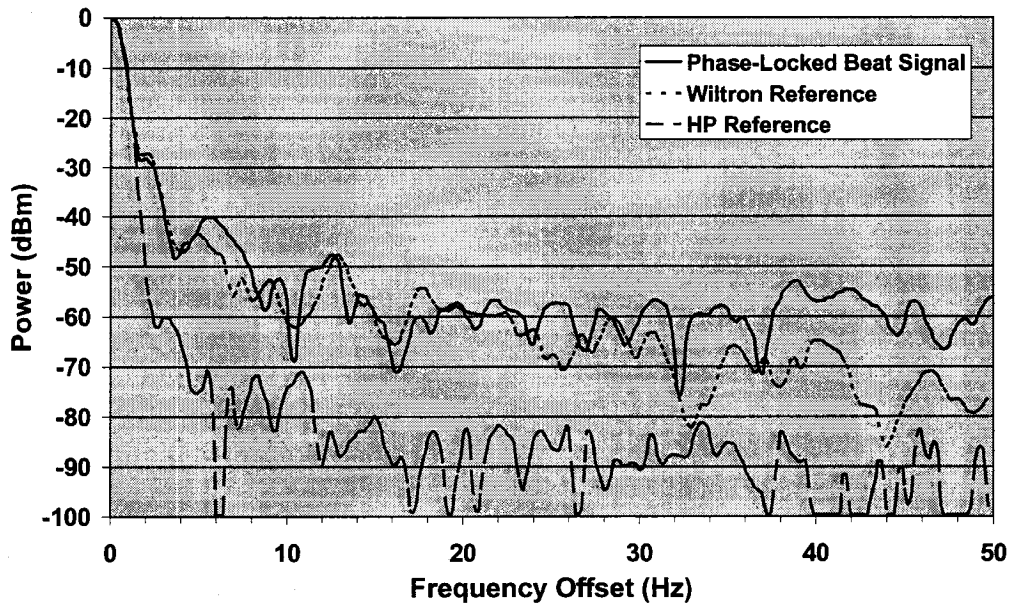

(d)

Fig. 4.20(d). Phase-locking result of OPLL with down-conversion at a span of 50 Hz (with reference source comparison). Center frequency: f_0 = 11.22 GHz.

In order to make a comparison between the beat signal and the two microwave reference sources used in the system, the spectra of all three are plotted on the same axes in Fig. 4.20 (d), where the output power has been normalized to 0 dBm. The quality of the phase-locked signal closely matches the quality of both reference sources. The 3-dB bandwidths of the signals can all be seen to be about 1 Hz (this measurement is limited by the 1 Hz resolution bandwidth of the spectrum analyzer – Agilent 8565E).

The phase noise is also measured, using an Agilent E5052A Signal Source Analyzer. The resultant phase noise is measured to be -64.7 dBc/Hz at 100 Hz offset and –72.5 dBc/Hz at 10 kHz offset [82].

The frequency stability of the microwave output signal was also recorded. The frequency value of the signal peak is extracted every 30 seconds and the trend over a 60 minute period is plotted. The result is shown in Fig. 4.21. The output signal is highly frequency stable with maximum deviation of no more than 1.5 Hz over the time period. A histogram of the stability data shows an almost Gaussian distribution about the mean during this period. Measurements over a longer time period are required to confirm this distribution.

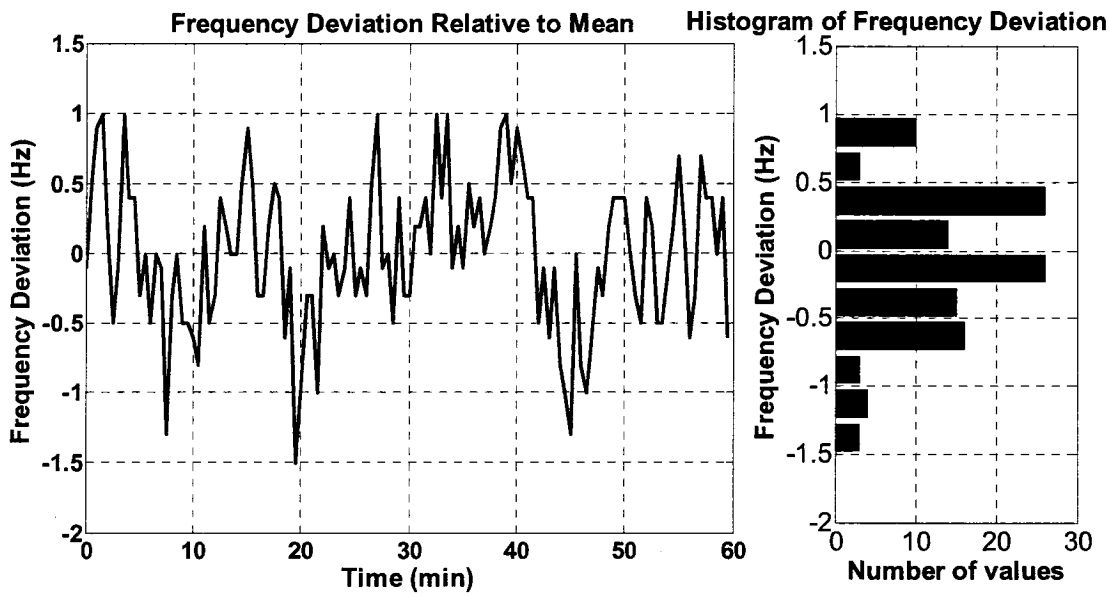

Fig. 4.21. Frequency deviation measurement of the OPLL output over a 60-minute time period. Measurements were taken every 30 seconds.

4.1.6 Illustration of Loop Delay Effect

To show the effect that loop delay can have on the operation of an OPLL, an experiment is carried out to test the system performance as increasing amounts of delay are inserted into the OPLL feedback loop. This is accomplished by placing 20 cm lengths of optical fiber between the coupler and the feedback photodetector. Using an estimate of the fiber effective refractive index of n_{eff} = 1.47, the time delay for a 20 cm length of fiber is Δt = 1 ns. The following figure shows the effect of incrementally adding up to four lengths of fiber into the feedback loop.

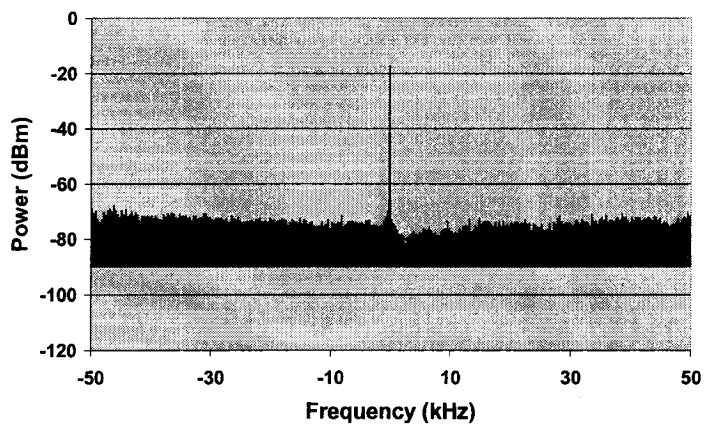

(a) 1 ns of additional delay

Fig. 4.22. OPLL output signal degradation with increasing loop delay.

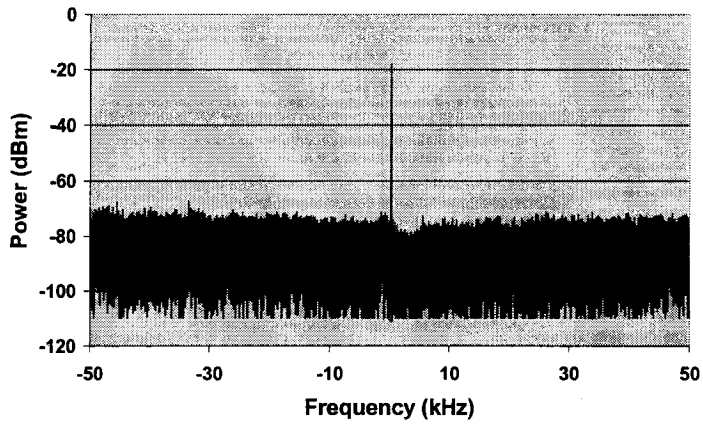

(b) 2 ns of additional delay

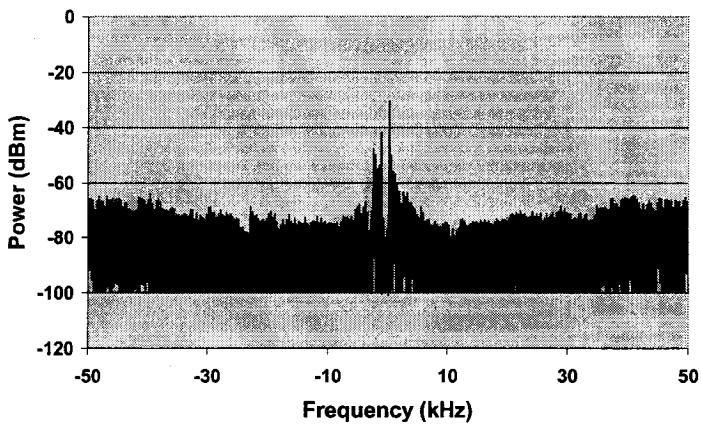

(c) 3 ns of additional delay

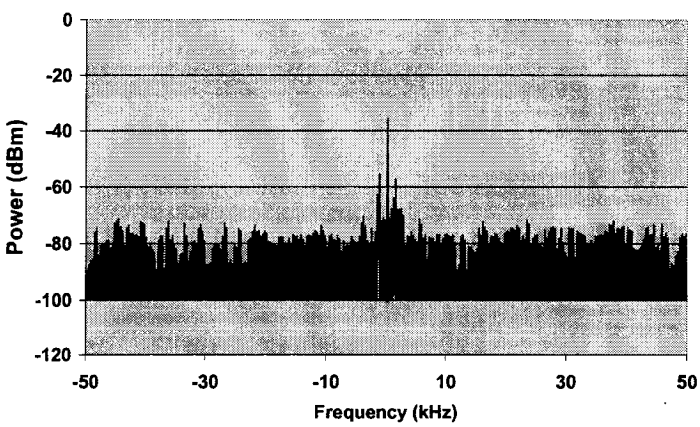

(d) 4 ns of additional delay

Fig. 4.22. OPLL output signal degradation with increasing loop delay.

The degradation of the microwave output signal, and the increase in the surrounding noise, is apparent in the previous figure. This shows the sensitivity of the OPLL to even small amounts of loop delay and emphasizes the attention that must be given to ensuring the feedback path is as short, physically and temporally, as possible.

4.2 Summary

The operation of a frequency discriminator-aided OPLL system was discussed in this chapter, along with the new frequency down-conversion module implemented in this project. An analysis of the down-conversion module's contribution to the phase noise of the system was carried out. The redesign of each frequency discriminator component and the calibration of its overall output were also discussed. The performance achieved by the discriminator-aided OPLL with the down-conversion module, in terms of 3-dB bandwidth, phase noise, and frequency stability was presented and the effects of additional loop delay on the system were analyzed.

Chapter 5

TRUE-TIME DELAY MODULE AND EXPERIMENTAL RESULTS

This chapter presents the TTD beamforming module. It describes the FBG fabrication for each individual delay line and gives the optical delay line transmission and reflection spectra. The measured time delay results are also reported, along with simulations of the generated antenna radiation patterns.

5.1 FBG-Based True-Time Delay Module

The TTD beamforming module studied in this research project was briefly introduced in Section 2.1.5. It uses delay lines consisting of discrete, uniform FBGs to achieve the variable time delay progression required to steer the antenna radiation pattern.

5.1.1 Concept

The TTD beamforming module is shown in Fig. 5.1. It is composed of four delay lines, each consisting of three FBGs, which are fed by the OPLL via an optical power splitter and circulators.

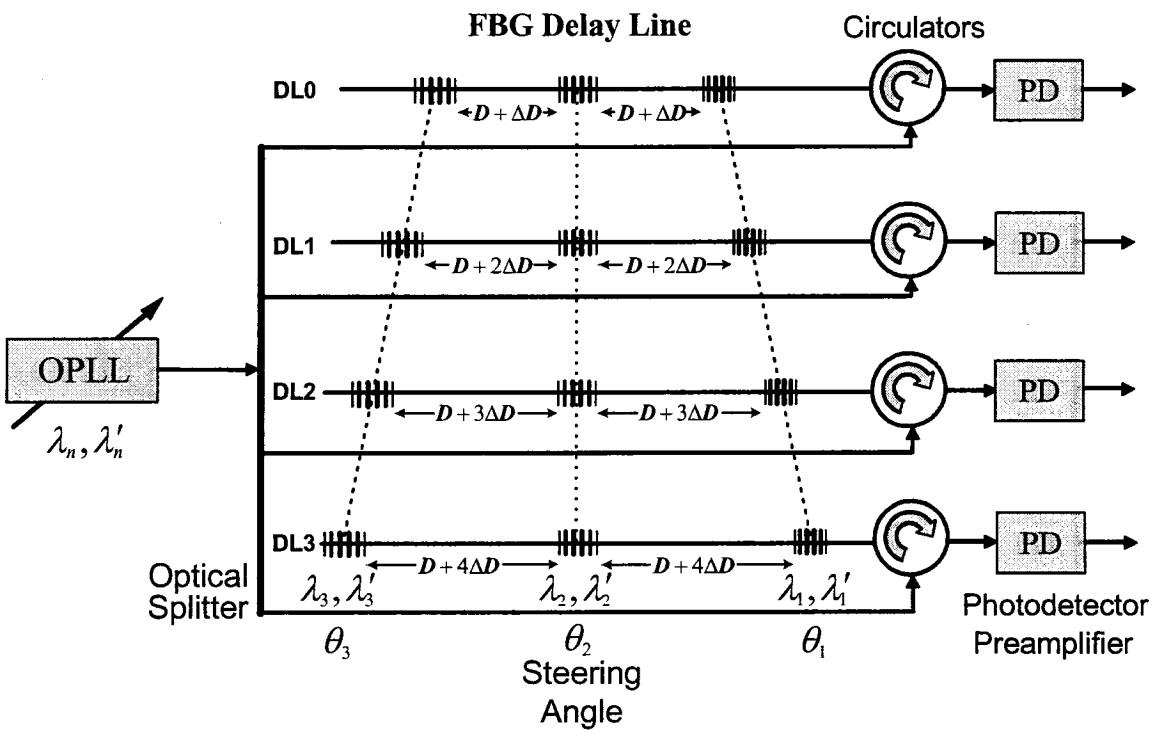

Fig. 5.1. TTD beamforming module.

The FBGs along the same dashed lines are fabricated with identical central reflection wavelengths. By tuning the two optical wavelengths of the OPLL, λ_n, λ_n', to the central reflection wavelength of the FBGs along the dashed lines, different time delay progressions are generated, leading to different radiation directions [19]. The center FBGs are all aligned such that they produce the same delay, thus, tuning the OPLL output

to this wavelength will generate zero relative time delay between the antenna elements and result in a broadside beam direction. Tuning the OPLL output to either the upper or lower wavelength FBG produces a linear time delay progression and, hence, a linear phase progression, that will steer the antenna beam to a specific angle dependent on the magnitude of the phase progression. The beamforming module, then, produces three time delay progressions, corresponding to the three discrete FBG positions on each delay line, and is able to steer the antenna radiation pattern to three different angles.

The physical parameter that controls the magnitude of the delay progression is ΔD, the incremental distance between each FBG. The first delay line, DL0, will have FBG spacings of ΔD plus, possibly, some constant value, D, common to all delay lines; the second delay line, DL1, will have spacings of $2\Delta D$ plus D, etc. This parameter determines the relative time delay of the signals and, therefore, the relative phase shift.

5.1.2 Derivation of Delay Spacing

According to phased-array antenna theory, to avoid grating lobes – secondary maxima – in the antenna radiation pattern the distance between each array element, d, must satisfy

$$d \leq \frac{\lambda_{RF}}{1+|\sin\theta_{\max}|} \tag{5.1}$$

where λ_{RF} is the free space wavelength of the microwave signal and $\theta_{\max}$ is the maximum steering angle. It is assumed that $\theta_{\max} = \pm 90°$, therefore (5.1) becomes

$$d \leq \frac{\lambda_{RF}}{2}. \tag{5.2}$$

For an operating frequency of 6.72 GHz (chosen for reasons relating to the test setup discussed later) this maximum spacing between elements is calculated as $d \leq 2.232$ cm.

The normalized array factor was derived in Section 2.1.2 as

$$|af(\Psi)| = \left| \frac{\sin(N\Psi/2)}{N\sin(\Psi/2)} \right| \tag{5.3}$$

where $\Psi = kd\cos\theta + \beta$. This expression can be used to simulate the antenna radiation pattern for a particular phase progression, β. The phase progression is determined for a given steering angle, θ, by setting $\Psi = 0$. A simulated radiation pattern is shown in Fig. 5.2.

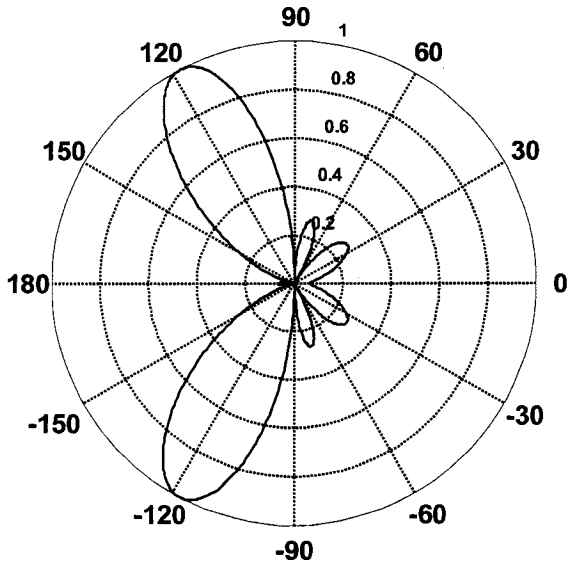

(a)

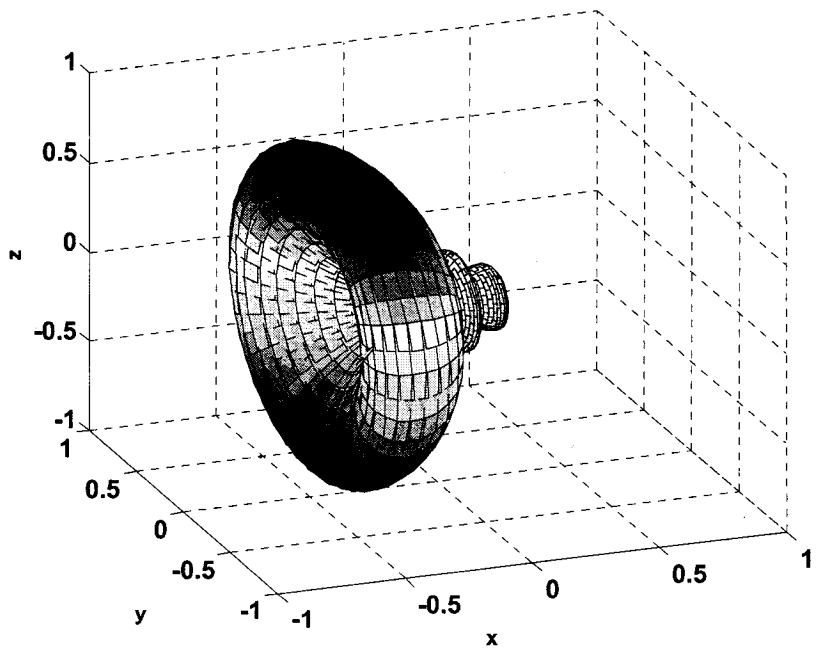

(b)

Fig. 5.2. Simulated radiation pattern for a PAA using TTD ($N = 4$, $\theta = 28°$, $d = 2.23$ cm). (a) Two-dimensional pattern; (b) Three-dimensional pattern.

These radiation patterns were simulated with $d = 2.23$ cm at a steering angle of 28° from broadside. It can be seen that this element spacing produces a beam pattern with a well-defined main-lobe and minimal grating lobes. Thus, this value is used as the element spacing in further calculations.

For an N-element linear array the incremental time delay required between each element to produce a steering angle, θ, of the radiation pattern can be expressed as follows

$$\Delta\tau = \frac{kd\sin\theta}{2\pi f_{RF}} \tag{5.4}$$

where k is the free space wave number, and θ is measured with respect to broadside.

For a ±28° steering angle the incremental time delay is calculated as $\Delta\tau = 34.89$ ps. From this time delay value, and knowledge of the effective index, n_{eff}, of the fiber, the incremental spacing required between each grating can be determined using

$$\Delta D = \frac{c\Delta\tau}{2n_{eff}}. \tag{5.5}$$

Using the parameters given above, this spacing is calculated as $\Delta D = 3.6$ mm.

The distance, D, in Fig. 5.1, is a constant spacing that exists between each FBG and is partly a function of the grating length. Theoretically, this constant spacing can be any

value as long as it is the same for each delay line. The important parameter is the difference in separation, determined by ΔD.

Based on this incremental spacing four delay lines are fabricated with a linearly increasing separation, ΔL, between each adjacent FBG. These separation values are given in Table 5.1.

Delay Line Number	Delay Spacing, ΔL (mm)
DL 0	$D + 0$
DL 1	$D + 3.6$
DL 2	$D + 7.2$
DL 3	$D + 10.8$

Table 5.1 Calculated delay line spacing.

5.1.3 FBG Delay Line Considerations

With the FBG spacing determined, several other parameters affecting delay line fabrication must be addressed. Figs. 5.3(a) and (b) show the schematic and the theoretical reflection spectrum of a single delay line.

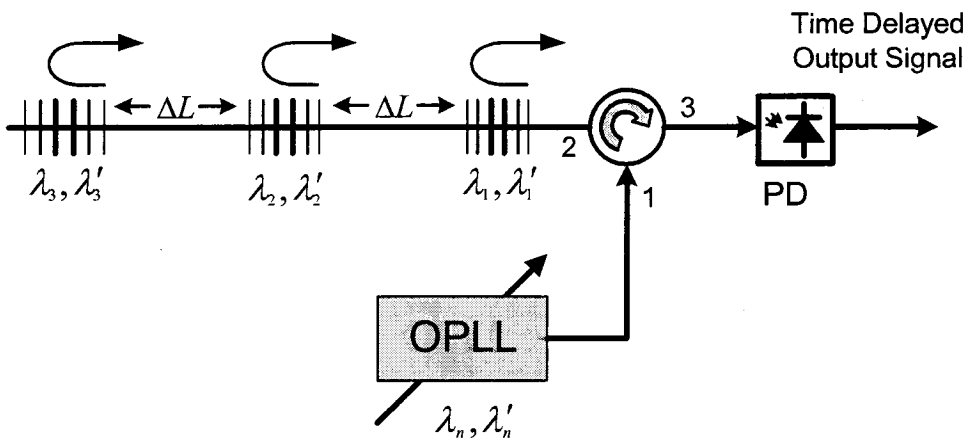

(a)

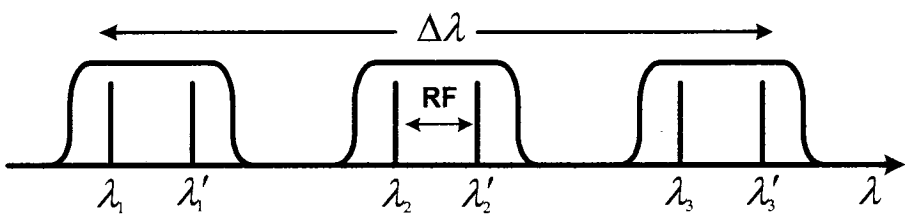

(b)

Fig. 5.3. (a) Schematic representation of a single delay line; (b) Theoretical spectral profile of a 3-FBG delay line and the interaction of the RF-spaced wavelengths with each FBG. $\Delta\lambda$ is the overall spectral width of the delay line.

In this system, the output wavelengths of the OPLL are temperature tuned such that both λ_n, λ_n', are reflected within the same grating. Thus, the FBG spectral width is an important parameter since each FBG must be able to reflect both wavelengths in order to avoid any corruption of the microwave output. The spectral width of each grating, then, imposes a limitation on the achievable microwave output frequency. In order to achieve a higher frequency the FBG spectral width must be enlarged accordingly.

Another important parameter for each FBG delay line is the overall spectral width, $\Delta\lambda$. This width determines the wavelength tuning range that must be covered by the laser diodes of the OPLL. This system uses two ECLs, which are not widely tunable. Therefore, achieving closely spaced FBGs, which do not interfere with each other, within the ECL tuning range, is very important.

5.1.4 Laser Tuning Range

Wavelength tuning is accomplished in the OPLL setup through temperature control. Varying the TEC temperature of each ECL causes a microscopic change in cavity length within each laser diode, thus, this property can be used to change the laser diodes operating wavelengths.

The two K2 Optronics ECLs have a listed temperature tuning coefficient of 16 pm/°C [84]. Based on a temperature-tuning span of 25°C, the maximum wavelength tuning range possible is 0.4 nm. If an estimate of the individual FBG spectral width is taken as approximately 0.15 nm, it is not possible to write three gratings within the tuning range of the ECLs. Further measurement of the ECL tuning responses is required to determine if their temperature tuning range can be extended. Figs. 5.4 (a) and (b) show the measured temperature tuning responses of the two ECLs, identified by their serial numbers as K2 623 and K2 691.

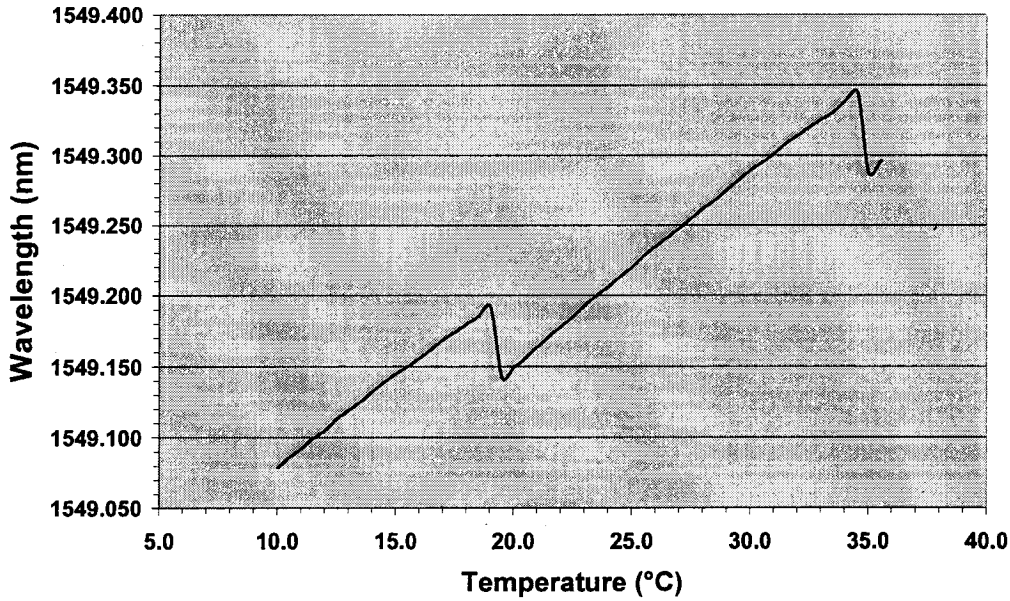

(a) K2 623

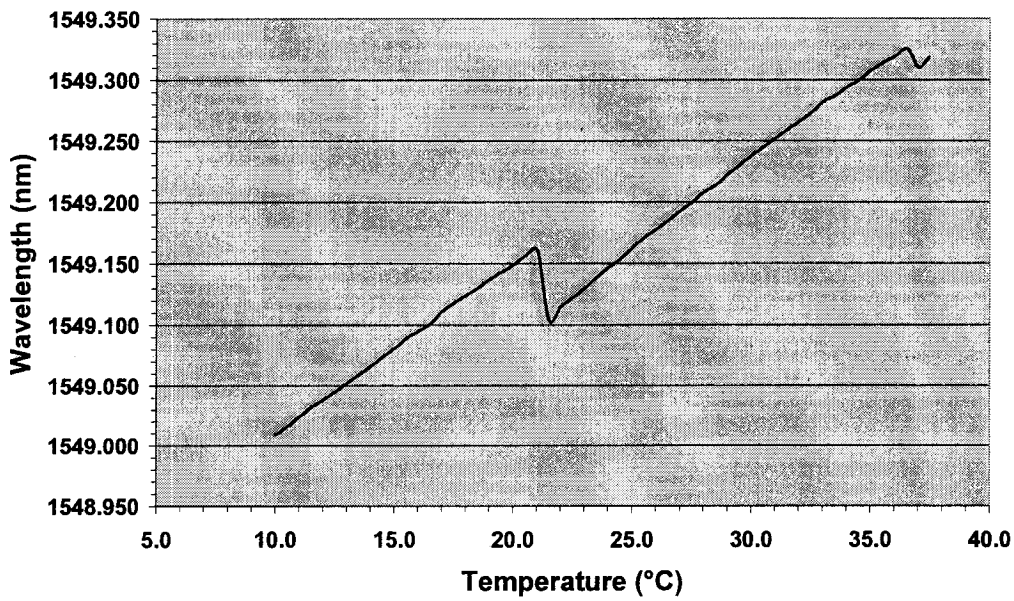

(b) K2 691

Fig. 5.4. Temperature tuning response of ECLs.

One advantageous result found from the experimental measurements, is the fact that the laser output wavelengths are not identical. Even though their tuning ranges are virtually the same, the slight offset in actual operating wavelength extends the differential between the maximum wavelength attainable by the higher-wavelength laser and the minimum wavelength attainable by the lower-wavelength laser. One clear disadvantage, however, are the mode hops that occur at certain temperatures for each ECL. Immediately after a mode hop point the output wavelength of the laser drops on the order of 50 pm. This reduces the overall ECL tuning range from even the 0.4 nm value calculated previously. However, it was found that, by combining a temperature shift with a current adjustment, the $\Delta\lambda$ tuning range could be extended up to 0.53 nm. The temperature was also pushed up to 45°C after consultation with the manufacturer determined this would be a safe procedure if limited to short periods of time.

The 0.53 nm tuning range is still quite narrow and, for this reason, every effort was made to space the FBGs as closely as possible, while avoiding detrimental overlap of their reflection spectra.

5.1.5 FBG Fabrication

A hydrogen-loading process, as discussed in Section 2.2.3, was used for the photosensitization of the fibers used to fabricate the FBG delay lines. Each fiber was

placed in a high-pressure tube at approximately 1000 psi and allowed to soak for a two week period at room-temperature.

The FBG exposure process employed was a phase mask technique, as outlined in Section 2.2.2, using a uniform, 14 cm-long phase mask with a period, Λ_{PM} = 1072.2 nm. Assuming an effective refractive index of 1.446, the center wavelength of FBGs written with this phase mask can be determined from (2.33) as $\lambda_B = (1.446)(1072.2\,\text{nm}) = 1550.40\,\text{nm}$. This is above the operating wavelength of the ECLs, and, since this was the only suitably long phase mask available, an alternative technique to lower the writing wavelength had to be used.

The technique used was to place tension on the optical fiber during the exposure process. Stretching a fiber lengthens it very slightly, while the phase mask period, obviously remains the same. Thus, when the tension is removed, the fiber relaxes back to its original length reducing the period of the induced FBG. From (2.19) it can be seen that any reduction of the FBG period proportionally reduces the reflection wavelength as well. Therefore, this technique can be used to vary the reflection wavelength of FBGs written with the same phase mask [85], [86].

A frequency-doubled 244 nm argon ion laser was used as the UV source during the exposure process. It was operated in continuous-wave mode at an output power of 90 mW. The exposure setup is shown in Fig. 5.5.

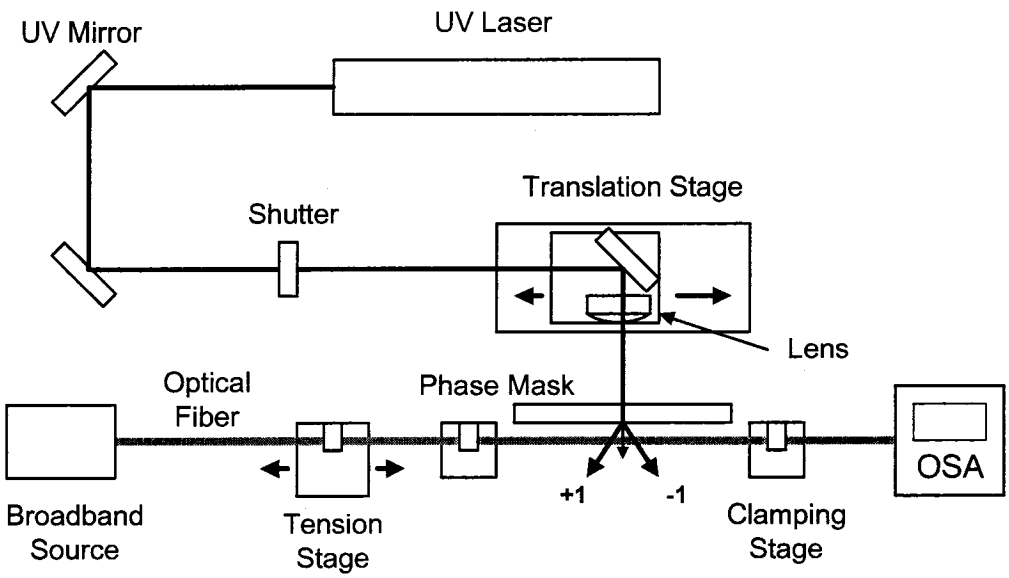

Fig. 5.5. Fiber Bragg grating exposure setup (OSA: Optical spectrum analyzer).

A lens is used just before the phase mask stage to focus the UV beam onto the fiber. A UV mirror mounted on a translation stage is used to scan the beam along the length of the phase mask and the velocity of translation is used to control the induced refractive index change. A fast scanning velocity induces a small index change and a slow scanning velocity induces a large change. Thus, by properly controlling the scanning velocity many different apodization profiles can be created.

5.1.6 FBG Delay Line Results

In order to obtain the time delay progression required for the TTD beamforming setup it is important to precisely control the spacing of the three FBGs. Therefore, it is

advantageous to write the three FBGs on one fiber using a single phase mask to cover the entire length of the delay line. In this case, the 14 cm long phase mask allows the three FBGs to be written without moving either the phase mask or the fiber during the writing process. The only adjustment necessary is a change in the applied tension to spectrally shift each FBG's central wavelength relative to the next.

Each FBG is 3 cm long and was written with a raised sine apodization profile [87]. Based on simulation, this profile gives good sidelobe suppression and allows the grating spectra to be spaced closely without interfering with each other. The transmission and reflection spectra of the four delay lines fabricated are shown in Fig. 5.6.

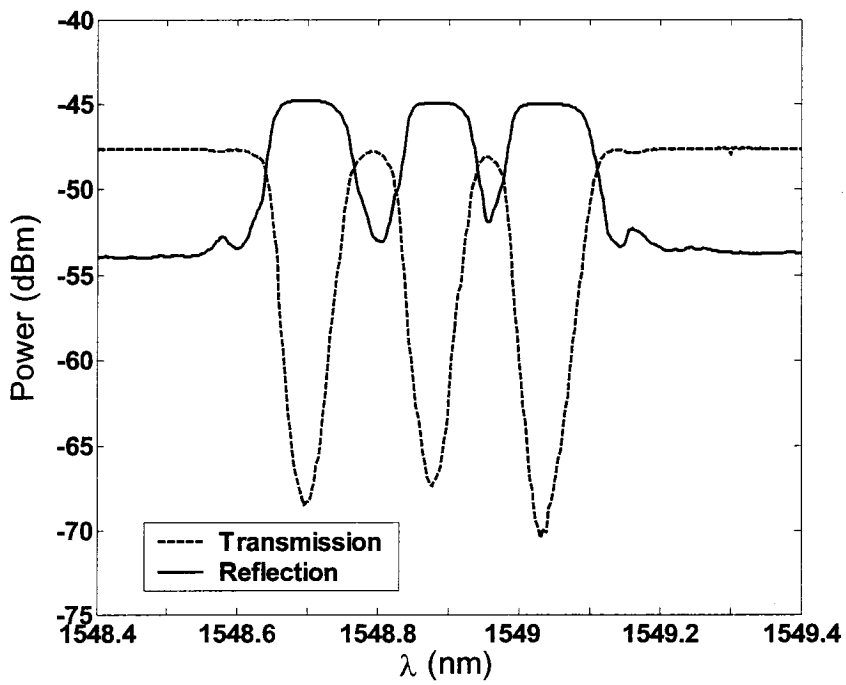

Fig. 5.6(a). Transmission and reflection spectra of FBG delay line DL0 with grating spacing of D + 0 mm.

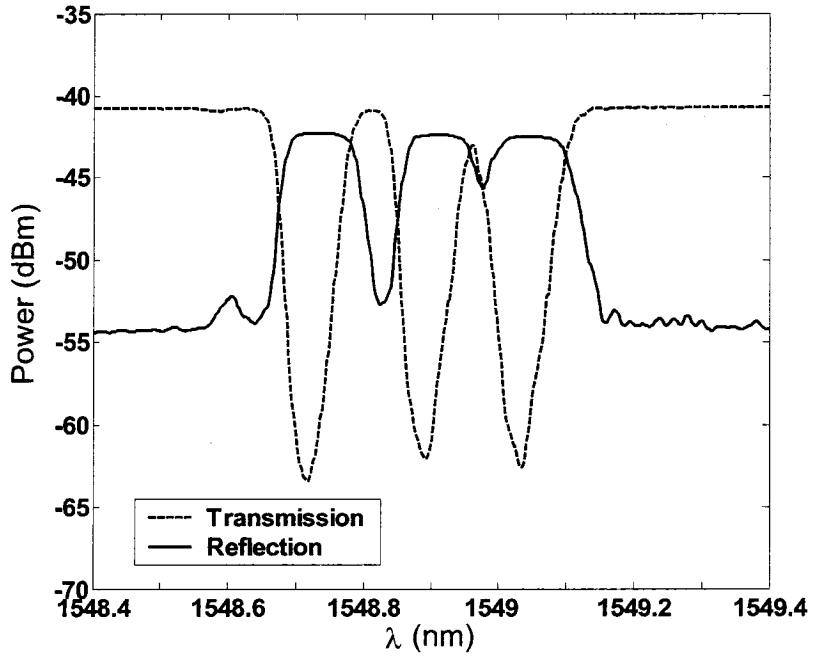

(b)

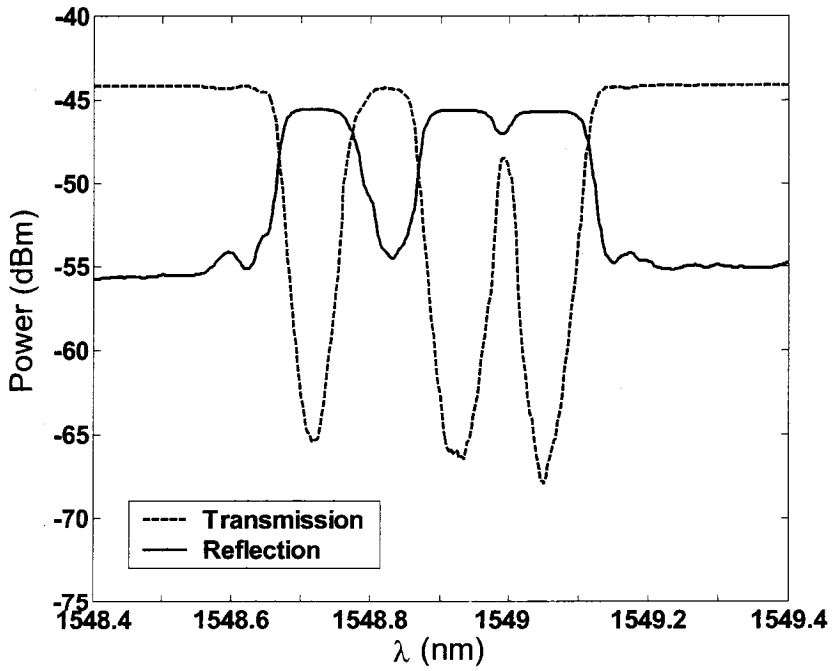

(c)

Fig. 5.6. Transmission and reflection spectra of FBG delay lines DL1 and DL2 with grating spacing of (b) D + 3.6 mm; and (c) D + 7.2 mm.

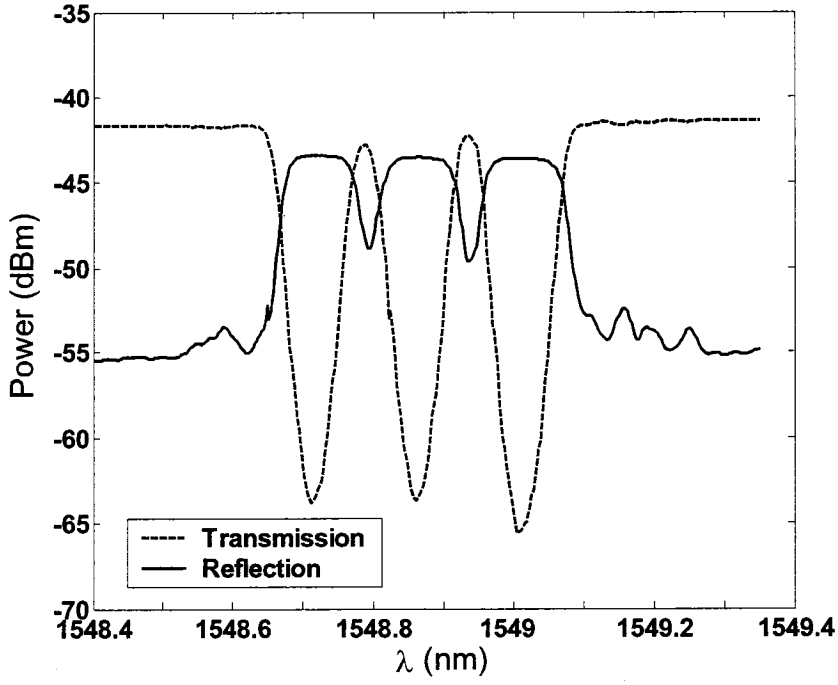

(d)

Fig. 5.6(d). Transmission and reflection spectra of FBG delay line DL3 with grating spacing of D + 10.8 mm.

The delay line spectra were recorded on an optical spectrum analyzer at a 0.01 nm resolution using a broadband source to illuminate the gratings. It can be seen that all four delay lines have similar spectral profiles with FBGs that have about 20-25 dB transmission depth and a spectral width of approximately 0.1 nm. Each grating overlaps slightly with the adjacent one, however, the overlap is not significant within the transmission bandwidth of the FBGs. Therefore, the adjacent FBG does not adversely affect the performance of its neighbour. Also, the total spectral width covered by the three FBGs in all four delay lines is well within the 0.53 nm tuning range of the ECLs.

The other important parameter discussed was the individual FBG spectral width which allows each grating to reflect both wavelengths generated by the OPLL. In this case, the 0.1 nm width is enough to accommodate a wavelength spacing corresponding to a microwave frequency of up to 12 GHz.

5.1.7 Difficulties Encountered

Several difficulties were encountered during the delay line exposure process. The first was the appearance of a very rippled grating spectrum on certain exposure attempts. An example of this effect is shown in Fig. 5.7.

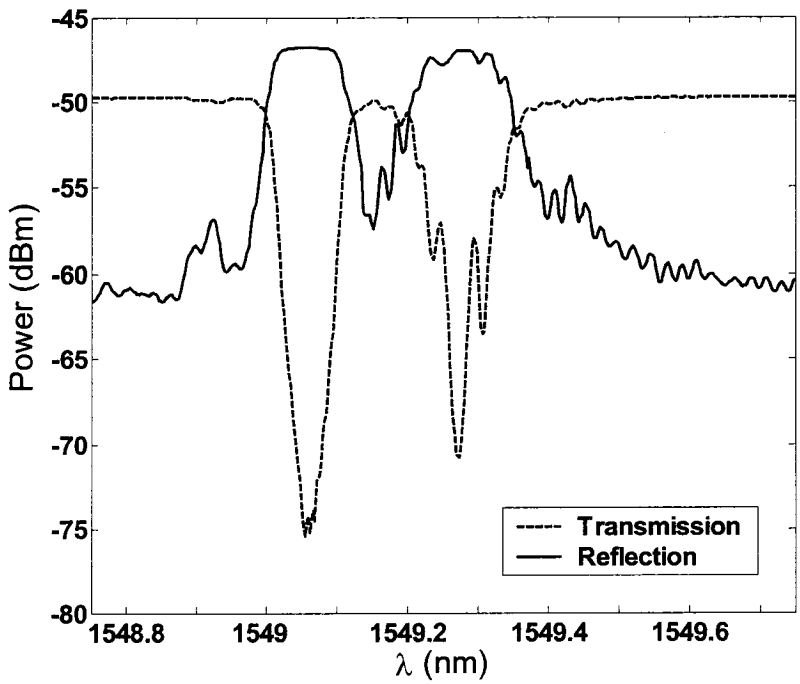

Fig. 5.7. Rippled spectrum obtained during FBG exposure process.

Different lengths and exposure times were used but the problem seemed to reappear each time, often on the second FBG in an exposure sequence but not exclusively. Attempts were made to attribute the problem to tension variations during the exposure process, to a Fabry-Perot cavity formed between adjacent FBGs or to a misalignment issue between the fiber and the phase mask. Subsequent testing of these hypotheses led to their being dismissed. The problem was resolved after the discovery of a software issue. The controller program did not reset the velocities calculated to create the apodization profile after each exposure unless changes to the parameters were made. This led to an issue when multiple gratings were written consecutively with the same settings, resulting in the rippled spectra.

A second problem was encountered with the alignment of the fiber and phase mask. Any slight misalignment of the two leads to a refractive index change that is at an angle to the fiber axis, in effect, creating a blazed grating. This effect can be seen in Fig. 5.8.

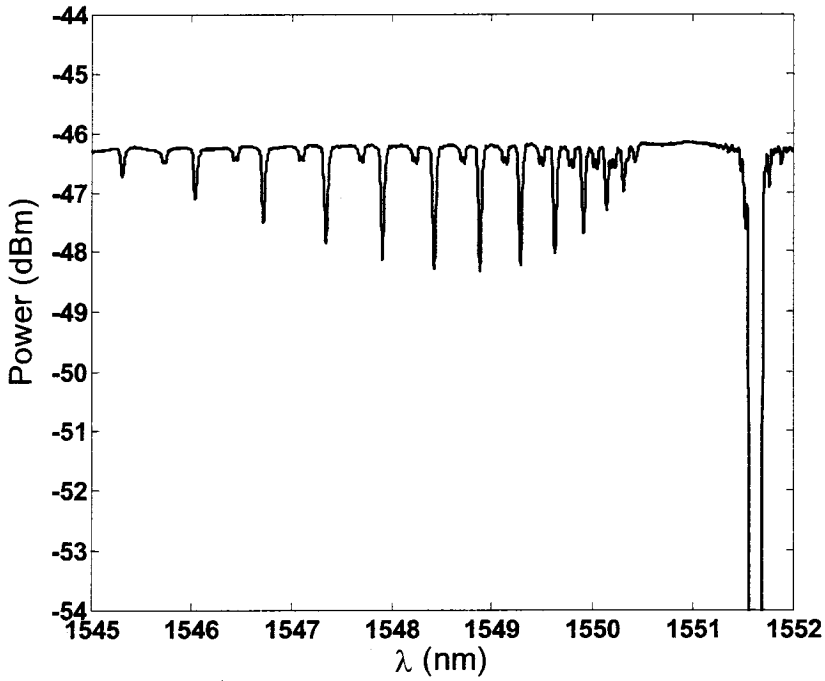

Fig. 5.8. Ripple due to blaze angle between phase mask and fiber during exposure.

The small transmission notches seen on the short wavelength side of the grating are the result of the blaze angle of the FBG in the fiber. This result agrees well with theoretical spectra of a blazed grating [31]. This effect was minimized by ensuring that the fiber and phase mask were properly aligned prior to each exposure and also, during the exposure process when it was necessary to change the tension on the fiber.

5.2 Time Delay Measurements

The goal of the measurement phase is to ensure that the OPLL will function with a TTD system, and then, to use the OPLL to measure the time delays associated with each delay line to ensure that the correct phase shift can be recovered after reflection.

In the test setup, a single fiber delay line is clamped between a translation stage and a fixed stage, and tension is applied to adjust its reflection wavelength such that the center FBG is aligned at 1549.2 nm. The OPLL is then engaged and its operating point is tuned such that the two wavelengths are reflected by the center FBG of the delay line. The reflected signal is then recovered by a PD and measured on the spectrum analyzer (SA). Fig. 5.9 shows the test setup used; however, in the first portion of the test the recovered signals are individually input to the SA, not the oscilloscope shown. This allows the quality of the signal reflected by the FBG to be analyzed.

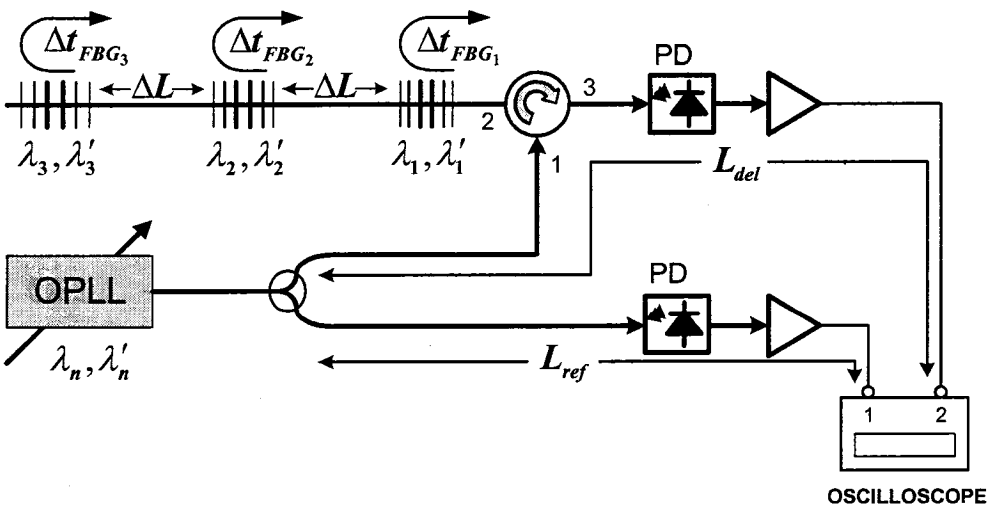

Fig. 5.9. Test setup used to measure relative time delays of each FBG delay line.

The OPLL signal is split via a Gould 3-dB coupler. The heterodyned signals, from both the reference and delay path, are recovered by two New Focus 45 GHz IR photodetectors. The amplifiers used are both broadband Agilent amplifiers (Series 83050A) with approximately 25 dB of gain. The signals are measured on a Tektronix Digital Phosphor oscilloscope (7 GHz - 20 GS/s). A picture of the actual test set-up is shown in Fig. 5.10.

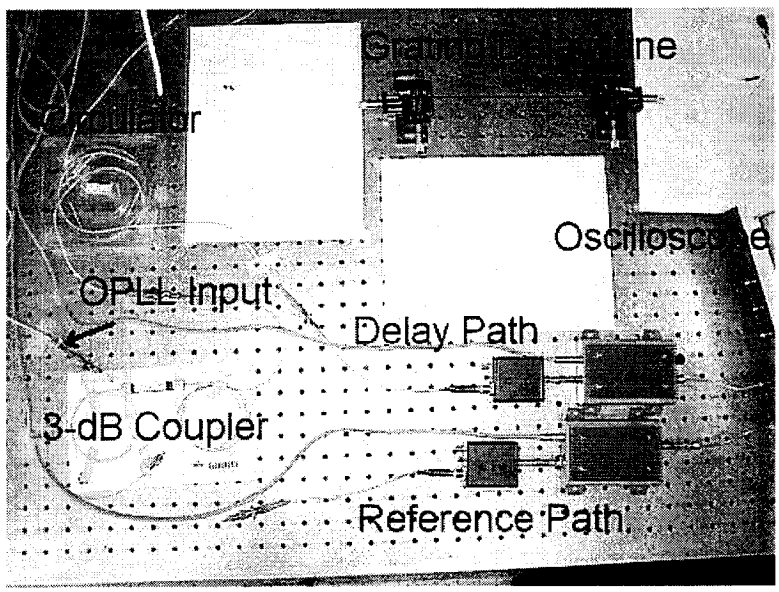

Fig. 5.10. Actual test setup used to measure time delays of each FBG delay line.

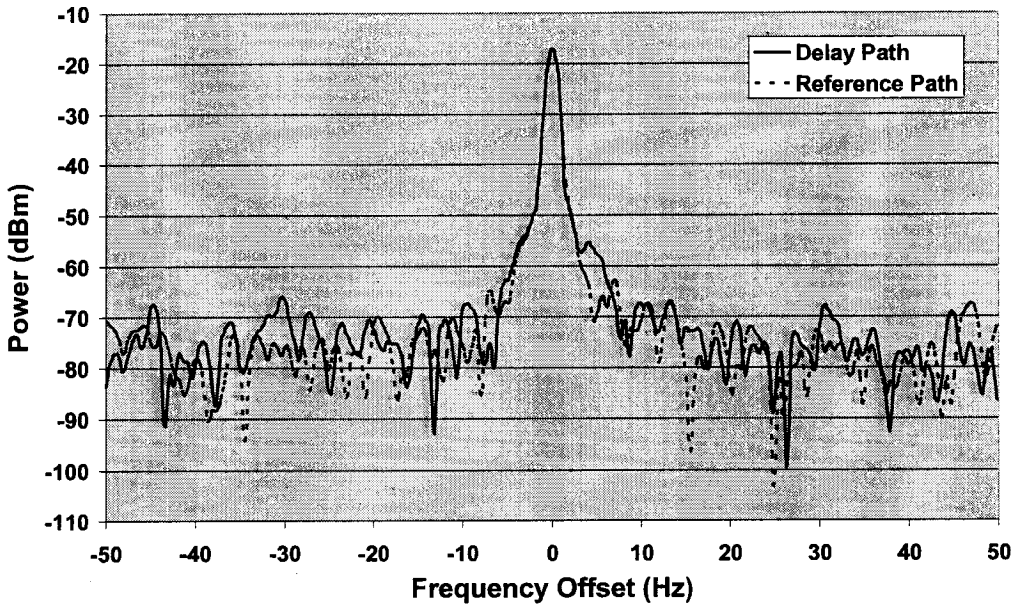

Fig. 5.11. Delay path and reference path signal comparison.

Fig. 5.11 shows the resultant signals, one from the reference path and the other from the delay path. Comparing these two signals, it can be seen that the reflected signal is very similar to the one recovered from the reference path. The 3-dB bandwidths are the same and the noise levels are comparable. This confirms that the two wavelengths generated by the OPLL can be reflected by a fiber Bragg grating without losing the phase coherence established by the loop feedback.

The time delay measurement portion of the test is done using the same setup shown in Fig. 5.9. It is carried out at 6.72 GHz since the maximum input frequency of the oscilloscope used in the measurement is 7 GHz. This is the reason that 6.72 GHz was chosen as the design point in the calculation of the incremental time delay. This frequency corresponds to a wavelength spacing of about 54 pm, and is achieved by

tuning S2 to an offset of 7.5GHz and S1 to 780 MHz. OSA displays of the wavelength alignment for two FBGs on DL1 are shown in Fig. 5.12.

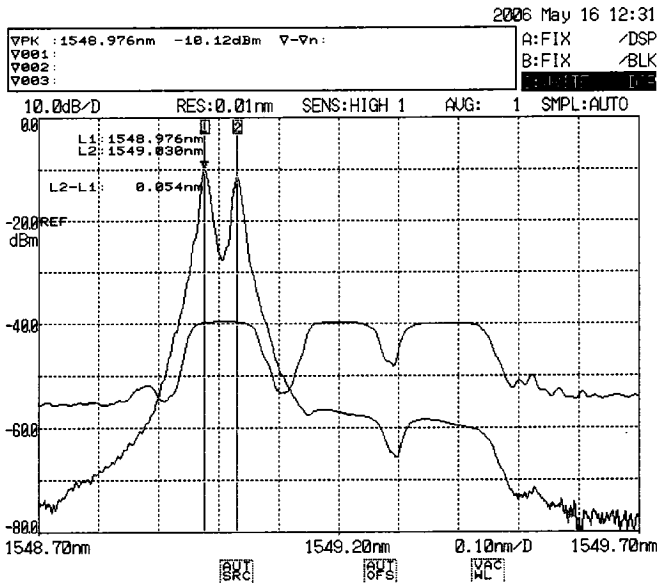

(a) Lower wavelength FBG alignment of DL1.

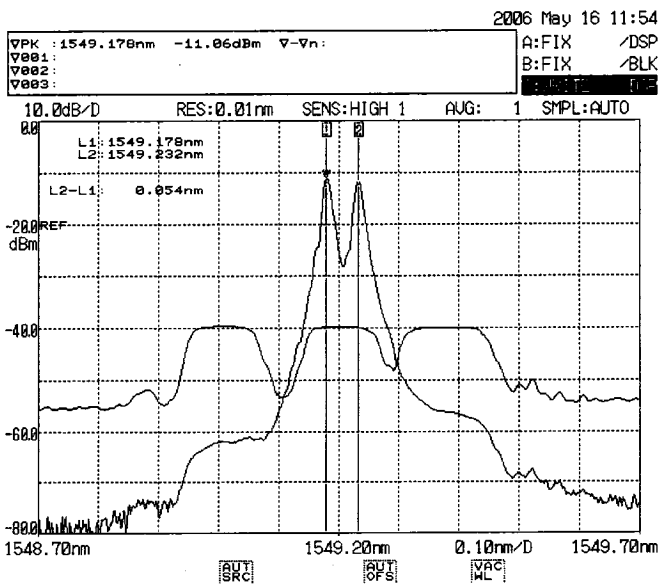

(b) Center wavelength FBG alignment of DL1.

Fig. 5.12. Delay-line FBG alignment with wavelengths of OPLL.

The time delay measurement is based on a comparison between the reference path and the delay path phases. Comparing the delay path signal to the reference path for each FBG (three separate operating wavelengths), gives three phase values which will be a function of the grating position and the path length traveled in the system. The relative phase of each upper and lower wavelength FBG, with respect to the center FBG, can be determined by subtracting the individual phases from the center FBG value. Since the setup uses an identical path for all three wavelength measurements, with the only difference being the reflection position, subtracting the phase values in this manner eliminates any effect path length difference has on the observed phase shift.

5.2.1 Measurement Derivation

The electric field for each of the two laser diodes in the OPLL can be represented as

$$e_1(t) = E_1 \cos(\omega_1 t + \phi_1) \tag{5.6a}$$
$$e_2(t) = E_2 \cos(\omega_2 t + \phi_2) \tag{5.6b}$$

where E_1 and E_2 are the amplitudes (V/m), ω_1 and ω_2 are the angular frequencies (rad/s), and ϕ_1 and ϕ_2 are the initial phase angles of the electric fields (rad).

When these two fields are beat at a square-law PD the output is

$$i_{PIN}(t) = |e_1(t) + e_2(t)|^2 = \tfrac{1}{2}\left(|E_1|^2 + |E_2|^2\right) + |E_1 E_2|\cos[(\omega_1 - \omega_2)t + \phi_1 - \phi_2] + 2\omega \text{ terms}. \quad (5.7)$$

The first term on the right-hand-side of the equation is a DC term which has no effect on the output phase and can be neglected. The 2ω high frequency terms are well out of range of the PD bandwidth and can, therefore, also be neglected. The term of interest, then, is the difference term that generates the microwave frequency.

The OPLL is tuned to one of the three reflection wavelengths of the delay line, say λ_1, λ_1', and this optical signal is split at the optical power divider. Part of the optical signal is transmitted through the reference path to the oscilloscope input port and can be written as

$$v_{ref} = k_1 |E_1 E_2| \cos(\omega_{RF} t + \omega_{RF} \Delta t_{ref} + \phi_1 - \phi_2) \quad (5.8)$$

where Δt_{ref} is the time taken to propagate along the reference path, L_{ref}; k_1 is a gain factor incorporating the reference path PD and amplifer gain; and ω_{RF} is the microwave frequency generated from the difference term, $\omega_1 - \omega_2$.

The other part of the optical signal is transmitted along the delay path, reflected by FBG_1 and input into the other oscilloscope port. This input can be written as

$$v_{del} = k_2 |E_1 E_2| \cos(\omega_{RF} t + \omega_{RF} \Delta t_{del} + \omega_{RF} \Delta t_{FBG_1} + \phi_1 - \phi_2) \quad (5.9)$$

where Δt_{del} is the time taken to propagate along the delay path, L_{del}; k_2 is a gain factor incorporating the delay path PD and amplifier gain; and Δt_{FBG_1} is the round trip delay between the circulator and FBG_1, as indicated in Fig. 5.9.

A phase difference comparison of the two input signals is done at the oscilloscope, giving

$$\phi_{FBG_1} = \omega_{RF}(\Delta t_{FBG_1} + \Delta t_{del} - \Delta t_{ref}) \tag{5.10}$$

where the initial phase terms have cancelled and the remaining phase angle is a combination of path length and the position of FBG_1. Similarly, for FBG_2 and FBG_3 we can write

$$\phi_{FBG_2} = \omega_{RF}(\Delta t_{FBG_2} + \Delta t_{del} - \Delta t_{ref}) \tag{5.11a}$$
$$\phi_{FBG_3} = \omega_{RF}(\Delta t_{FBG_3} + \Delta t_{del} - \Delta t_{ref}). \tag{5.11b}$$

Now, using the center grating (FBG_2) phase angle as the reference point and subtracting the other two phase angles from it, we obtain

$$\Delta\phi_{21} = \omega_{RF}(\Delta t_{FBG_2} - \Delta t_{FBG_1}) \tag{5.12a}$$
$$\Delta\phi_{23} = \omega_{RF}(\Delta t_{FBG_2} - \Delta t_{FBG_3}) \tag{5.12b}$$

where the contribution to the phase from path length is now cancelled. From these two phase values, and the microwave frequency, ω_{RF}, the time delays

$$\Delta t_{21} = \Delta t_{FBG_2} - \Delta t_{FBG_1} \quad (5.13a)$$

$$\Delta t_{23} = \Delta t_{FBG_2} - \Delta t_{FBG_3} \quad (5.13b)$$

can be extracted. These represent the amount of time for the round trip between adjacent FBGs on a single delay line.

All four delay lines were characterized using this experimental method giving two sets of delay values. One for the lower wavelength FBGs and one for the upper wavelength FBGs, relative to the center FBG of each delay line. The experimentally measured time delays are given in Table 5.2, along with the calculated values. The delay contributed by the constant spacing, D, has been subtracted from the measurements reported in the table, and only the amount of additional delay from the increments of ΔD is given.

	Theoretical Time Delays	Experimental Time Delays			Theoretical Time Delays
	Lower λ FBG (ps)	Lower λ FBG Δt_{21} (ps)	Center λ FBG Δt_{22} (ps)	Upper λ FBG Δt_{23} (ps)	Upper λ FBG (ps)
DL0	0	+0.58	0	-0.08	0
DL1	+34.89	+35.25	0	-34.92	-34.89
DL2	+69.78	+69.67	0	-70.50	-69.78
DL3	+104.67	+104.50	0	-105.17	-104.67

Table 5.2 Measured time delay values.

It is evident that a linear time delay progression is recovered and the experimentally measured time delays closely match the designed time delay values calculated from (5.4).

This result shows that an OPLL can be applied to a TTD beamforming system with successful recovery of the necessary time delays for beam steering [88].

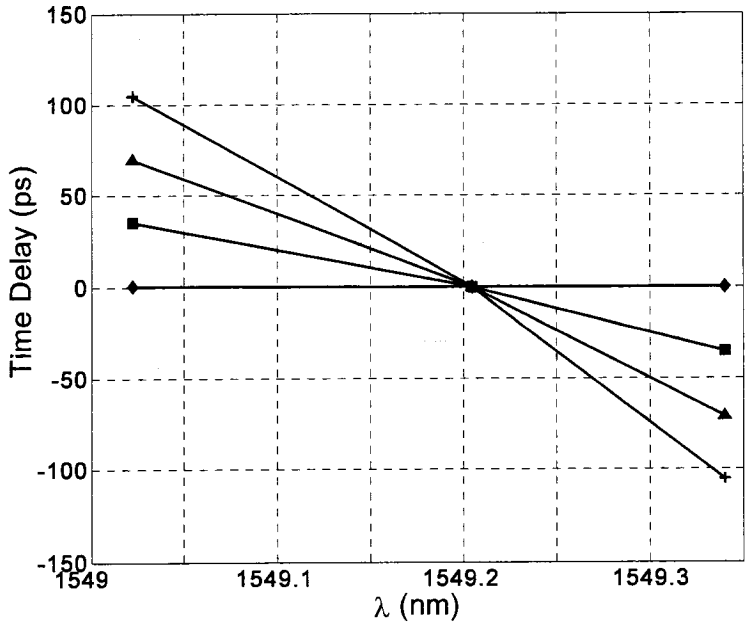

Fig. 5.13. Time delay progression of the measured delay values.

The measured time delays are plotted as a function of wavelength in Fig. 5.13. The even temporal spacing of each upper and lower FBG away from the center FBG is represented by the linearity of the individual traces. The linear time delay progression is represented by the consistent step in slope apparent from one delay line plot to the next.

5.2.2 Antenna Radiation Patterns

Simulated antenna radiation patterns can be generated from the recovered time delay progressions. The broadside pattern will be generated from the center gratings, which have zero relative time delay. This output pattern is shown in Fig. 5.14(a).

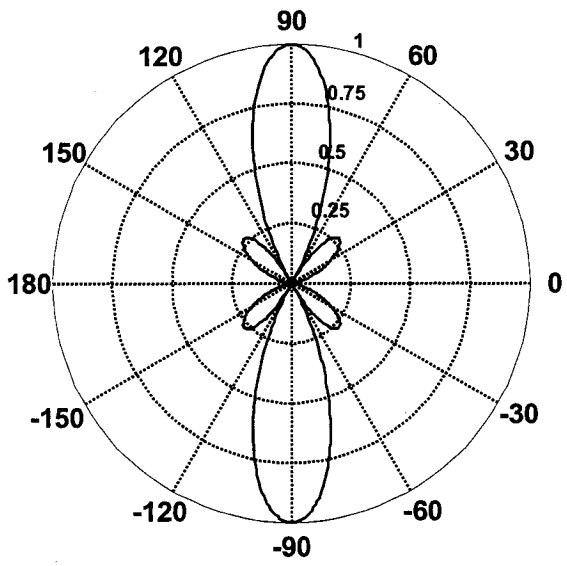

(a)

Fig. 5.14(a). Simulated radiation pattern generated from the experimentally measured time delay progression for: Center wavelength delays → broadside beam.

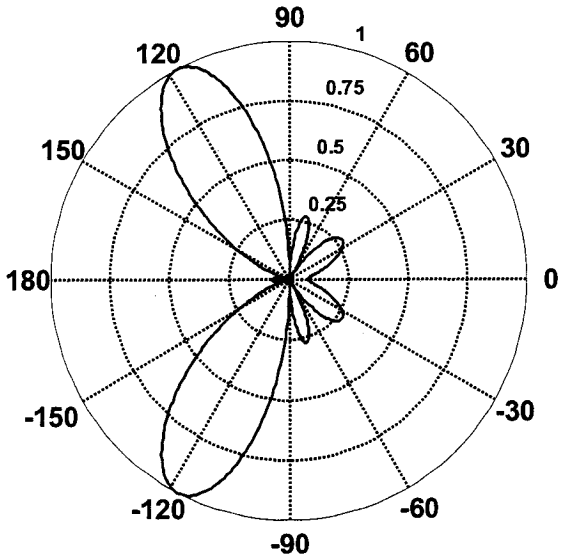

(b)

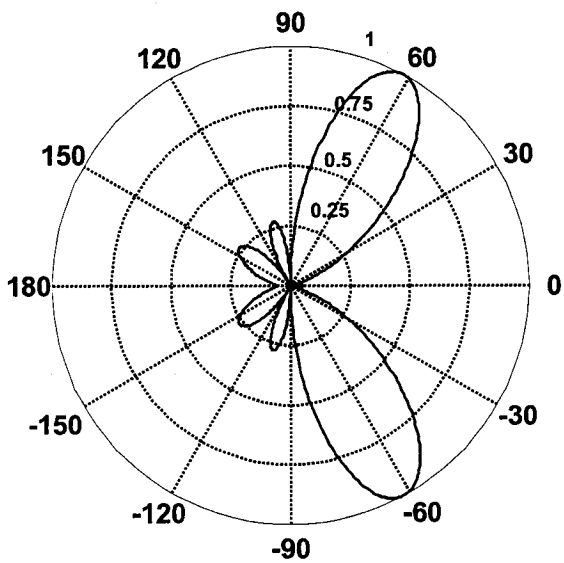

(c)

Fig. 5.14. Simulated radiation patterns generated from the experimentally measured time delay progressions for (b) Lower wavelength delays → +28° beam; and (c) Upper wavelength delays → -28° beam.

The lower and upper wavelength delay progressions generate the radiation patterns seen in Fig. 5.14 (b) and (c), respectively. The delay progression was designed to give a steering angle of approximately ±28° from broadside. It can be seen that the experimentally measured time delays do, in fact, generate the designed steering angle.

5.3 Summary

The TTD beamforming module was presented in this chapter. The incremental FBG spacing on each delay line was calculated and the FBG fabrication technique used in this project was outlined. Transmission and reflection spectra were introduced to show the quality of the FBG-based delay lines in terms of spectral width, reflection strength and spectral spacing. Some difficulties encountered throughout the project were also presented. The measurement technique used to determine the time delays associated with each delay line was introduced and the time delays generated by the application of the OPLL to the TTD system were reported. These results were then analyzed by plotting the delay versus wavelength curve and simulating the generated antenna radiation patterns. The generated time delays were found to agree well with the designed values and the simulated radiation patterns did, in fact, produce the expected ±28° steering angle.

Chapter 6

CONCLUSIONS AND FUTURE WORK

6.1 Conclusions

The main objectives of this research project were to develop an optical-heterodyne dual-wavelength source suitable for application in a photonic TTD beamforming system; to design and fabricate an FBG-based TTD beamforming module; and to measure the time delays generated by applying the optical-heterodyne source to the TTD module. Each of these objectives was successfully accomplished throughout the course of this project. The heterodyne source was implemented in the form of a discriminator-aided optical phase-lock loop. It is believed that this result marks the first time that a dual-wavelength optical phase-lock loop has been applied in this type of FBG-based TTD system.

In Chapter 2, the theory associated with phased-array antennas and fiber Bragg gratings was presented, and the benefits of using a photonic true time-delay module as the feed network for a PAA were detailed. The theoretical model for a linear PAA was presented, including the derivation of the normalized array factor for an N-element linear array. This chapter also discussed several FBG fabrication techniques, including the phase mask technique used in this project, and introduced the concept of photosensitizing a standard single-mode fiber through hydrogen-loading.

Chapter 3 introduced several techniques of optically generating microwave signals in radio-over-fiber applications and presented a theoretical overview of the concept of optical heterodyning. The theoretical operation of an OPLL was also presented along with its transfer function and operating parameters. The operation of a delay-line frequency discriminator was also introduced and the effects of laser linewidth on OPLL performance were discussed.

In Chapter 4, the operation of the frequency discriminator-aided OPLL system was discussed along with the new frequency down-conversion module implemented in this project. An analysis of this module's contribution to the phase noise of the system was carried out. The frequency discriminator redesign and calibration was also outlined and its performance was analyzed. This chapter presented the performance achieved by the discriminator-aided OPLL with down-conversion in terms of linewidth and frequency stability, and analyzed the effects of additional loop delay on the system.

The TTD beamforming module was presented in Chapter 5. The incremental FBG spacing on each delay line was calculated and the FBG fabrication technique was outlined. Transmission and reflection spectra were given to show the quality of the FBG-based delay lines in terms of spectral width, reflection strength and spectral spacing. Some difficulties encountered throughout the project were also presented. Finally, the measured time delays generated by the application of the OPLL to the TTD system were reported, along with simulations of the generated antenna radiation patterns. These results were found to agree well with the calculated values.

6.2 Future Work

This research project explored the design and fabrication of discrete FBG delay lines for application with a discriminator-aided OPLL source. This type of TTD system is capable of generating only discrete steering angles limited by the number of FBGs written on each delay line. One extension to this design would be to use a continuous TTD beamforming system that employed chirped FBGs rather than uniform FBGs. This arrangement would allow the main-lobe of the antenna to be steered through a continuous range of angles rather than simply the discrete angles achieved here. Such a system could be fabricated with a chirped phase mask in place of the uniform phase mask used in this project with the time delays being measured in much the same setup.

Another area for possible future work is with the optical source itself. The OPLL's microwave output signal can be improved in both phase noise performance and frequency tunability. One way to improve the phase noise performance is to combine the optical components in a photonic integrated circuit. This would shorten the critical loop delay for the feedback and help further suppress the laser diode phase noise. Integrating the optical components also requires the laser diodes to be specifically designed. This would allow them to be designed with a wider wavelength tuning characteristic which would give more flexibility in the design of a TTD module, as the FBGs would not have to be as closely spaced. This would, in turn, allow a wider range of steering angles to be achieved.

Being able to specifically design the laser wavelength tuning characteristic would also offer the possibility of using current tuning rather than temperature tuning to adjust the microwave frequency output. This would allow much faster sweeping of the output frequency since current-controlled wavelength tuning has a faster response time than the relatively slower temperature tuning response.

Another possible extension for the OPLL would be to modulate its output with a data signal. The data would be modulated onto one of the OPLL wavelengths, the modulated carrier would be sent through the TTD module and the data signal recovered at the output. This experiment would require further attention to the spectral width of each FBG, as now, one of the carriers has sidebands that must also be reflected by each FBG.

The variety of possibilities for further work on this system makes it a very interesting application for future research.

BIBLIOGRAPHY

[1] I. Frigyes and A. J. Seeds, "Optically generated true-time delay in phased-array antennas," *IEEE Trans. Microwave Theory Techn.*, vol. 43, no. 9, pp. 2378-2386, Sept. 1995.

[2] A. Molony, C. Edge and I. Bennion, "Fibre grating time delay element for phased array antennas," *Electron. Lett.*, vol. 31, no. 8, pp. 1485-1486, Aug. 1995.

[3] Y. Chen and R. T. Chen, "A fully packaged true-time delay module for a K-band phased array antenna system demonstration," *IEEE Photon. Technol. Lett.*, vol. 14, no. 8, pp. 1175-1177, Aug. 2002.

[4] R. A. Minasian and K. E. Alameh, "Optical-fiber grating-based beamforming network for microwave phased arrays," *IEEE Trans. Microwave Theory Techn.*, vol. 45, no. 8, pp. 1513-1517, Aug. 1997.

[5] L. Xu, R. Taylor, and S. R. Forrest, "The use of optically coherent detection techniques for true-time delay phased array and systems," *J. Lightwave Technol.*, vol. 13, no. 8, pp. 1663-1678, Aug. 1995.

[6] A. Molony, L. Zhang, J. A. R. Williams, I. Bennion, C. Edge, and J. Fells, "Fiber Bragg-grating true-time delay systems: discrete-grating array 3-b delay lines and chirped-grating 6-b delay lines," *IEEE Trans. Microwave Theory Techn.*, vol. 45, no. 8, pp. 1527–1530, Aug. 1997.

[7] W. Ng, A. A. Walston, G. L. Tangonan, J. J. Lee, I. L. Newberg, and N. Bernstein, "The first demonstration of an optically steered microwave phased array antenna using true-time-delay," *J. Lightwave Technol.*, vol. 9, no. 9, pp. 1124–1131, Sept. 1991.

[8] R. D. Esman, M. Y. Frankel, J. L. Dexter, L. Goldberg, M. G. Parent, D. Stilwell, and D. G. Cooper, "Fiber-optic prism true time-delay antenna feed," *IEEE Photon. Technol. Lett.*, vol. 5, no. 11, pp. 1347–1349, Nov. 1993.

[9] G. A. Ball, W. H. Glenn, and W. W. Morey, "Programmable fiber optic delay line," *IEEE Photon. Technol. Lett.*, vol. 6, no. 6, pp. 741–743, June 1994.

[10] D. T. K. Tong and M. C. Wu, "Programmable dispersion matrix using Bragg fiber grating for optically controlled phased array antennas," *Electron. Lett.*, vol. 32, no. 17, pp. 1532–1533, 1996.

[11] R. Benjamin and A. J. Seeds, "Optical beam forming techniques for phased array antennas," *IEE Proc.*, pt. H, vol. 139, no. 6, pp. 526-534, Dec. 1992.

[12] E. H. Monsay, K. C. Baldwin and M. J. Caccuitto, "Photonic true-time delay for high-frequency phased array systems," *IEEE Photon. Technol. Lett.*, vol. 6, no. 1, pp. 118-120, Jan. 1994.

[13] P. J. Matthews, M. Y. Frankel, and R. D. Esman, "A wide-band fiber-optic true-time-steered array receiver capable of multiple independent simultaneous beams," *IEEE Photon. Technol. Lett.*, vol. 10, no. 5, pp. 722-724, May 1998.

[14] D. N. McQuiddy, Jr., R. L. Gassner, P. Hull, J. S. Mason, and J.M. Bedinger, "Transmit/receive module technology for X-band active array radar," *Proceedings of the IEEE*, vol. 79, no. 3, pp. 308-341, Mar. 1991.

[15] S. Blais, "Design and realization of a Bragg grating prism on planar integrated optical waveguides for wideband photonic true time-delay beamforming," Master's thesis, School of Information Technology and Engineering (SITE), Univ. of Ottawa, Ottawa, ON, 2005.

[16] D. Dolfi, P. Joffre, J. Antoine, J. P. Huignard, D. Philippet, and P. Granger, "Experimental demonstration of a phased-array antenna optically controlled with phase and time delays," *Applied Optics*, vol. 35, no. 26, pp. 5293-5300, Sept. 1996.

[17] D. Dolfi, P. Joffre, J. Antoine, J. P. Huignard, D. Philippet, P. Granger, and J. Chazelas, " Photonics for phased array radars," *SPIE Optical Technology for Microwave Applications VII*, vol. 2560, pp. 158-165, Oct. 1995.

[18] D. T. K. Tong and M. C. Wu, "Multiwavelength optically controlled phased-array antennas," *IEEE Trans. Microwave Theory Techn.*, vol. 46, no. 1, pp. 108-115, Jan. 1998.

[19] H. Zmuda, R. A. Soref, P. Payson, S. Johns, and E. N. Toughlian, "Photonic beamformer for phased array antennas using a fiber grating prism," *IEEE Photon. Tech. Lett.*, vol. 9, no. 2, pp. 241-243, Feb. 1997.

[20] J. L. Corral, J. Marti, S. Regidor, J. M. Fuster, R. Laming, and M. J. Cole, "Continuously variable true time-delay optical feeder for phased-array antenna employing chirped fiber gratings," *IEEE Trans. Microwave Theory Techn.*, vol. 45, no. 8, pp. 1531-1536, Aug. 1997.

[21] J. L. Corral, J. Marti, J. M. Fuster, and R. I. Laming, "True time-delay scheme for feeding optically controlled phased-array antennas using chirped-fiber gratings," *IEEE Photon. Technol. Lett.*, vol. 9, no. 11, pp. 1529-1531, Nov. 1997.

[22] Yunqi Liu, Jianliang Yang, and Jianping Yao, "Continuous true-time-delay beamforming for phased array antenna using a tunable chirped fiber grating delay line," *IEEE Photon. Technol. Lett.*, vol. 14, no. 8, pp. 1172-1174, Aug. 2002.

[23] B. Ortega, J. L. Cruz, J. Capmany, M. V. Andrés, and D. Pastor, "Analysis of a microwave time delay line based on a perturbed uniform fiber Bragg grating operating at constant wavelength," *J. Lightwave Technol.*, vol. 18, no. 3, pp. 430-436, Mar. 2000.

[24] U. Gliese, T. N. Nielsen, S. Nørskov, and K. E. Stubkjær, "Multifunctional fiber-optic microwave links based on remote heterodyne detection," *IEEE Trans. Microwave Theory Techn.*, vol. 46, no. 5, pp. 458-468, May 1998.

[25] R. Hofstetter, H. Schmuck, and R. Heidemann, "Dispersion effects in optical millimeter-wave systems using self-heterodyne method for transport and generation," *IEEE Trans. Microwave Theory Techn.*, vol. 43, no. 9, pp. 2263-2269, Sept. 1995.

[26] E. Gill, "Engineering 7811: Antennas," Course Notes, Memorial University of Newfoundland, 2003.

[27] A. Petosa, "ELEC 5607: Antenna and Arrays," Course Notes, University of Ottawa, 2004.

[28] K. O. Hill and G. Meltz, "Fiber Bragg grating technology fundamentals and overview," *J. Lightwave Technol.*, vol. 15, no. 8, pp. 1263-1276, Aug. 1997.

[29] G. Meltz, W. W. Morey, and W. H. Glenn, "Formation of Bragg gratings in optical fibers by a transverse holographic method," *Optics Letters*, vol. 14, no. 15, pp. 823-825, Aug. 1989.

[30] T. Erdogan, "Fiber grating spectra," *J. Lightwave Technol.*, vol. 15, no. 8, pp. 1277-1294, Aug. 1997.

[31] R. Kashyap, "Fiber Bragg Gratings," Academic Press: California, USA, 1999.

[32] A. Yariv, "Coupled-mode theory for guided-wave optics," *J. Quantum Electronics*, vol. 9, no. 9, pp. 919-933, Sept. 1973.

[33] M. McCall, "On the application of coupled mode theory for modeling fiber Bragg gratings," *J. Lightwave Technol.*, vol. 18, no. 2, pp. 236-242, Feb. 2000.

[34] R. Kashyap, A. Swanton and D.J. Armes, "Simple technique for apodising chirped and unchirped fibre Bragg gratings," *Electron. Lett.*, vol. 32, no. 13, pp. 1226-1228, June 1996.

[35] J. Albert. K.O. Hill, B. Malo, S. Theriault. F. Bilodeau, D.C. Johnson and L.E. Erickson, "Apodisation of the spectral response of fibre Bragg gratings using a phase mask with variable diffraction efficiency," *Electron. Lett.*, vol. 31, no. 3, pp. 222-223, Feb. 1995.

[36] B. Malo, S. Theriault, D.C. Johnson, F. Bilodeau, J. Albert and K.O. Hill, "Apodised in-fibre Bragg grating reflectors photoimprinted using a phase mask," *Electron. Lett.*, vol. 31, no. 3, pp. 223-225, Feb. 1995.

[37] H. G. Fröhlich and R. Kashyap, "Two methods of apodisation of fibre-Bragg-gratings," Optics Communications, vol. 157, no. 1-6, pp. 273-281, Dec. 1998.

[38] V. Mizrahi and J. E. Sipe, "Optical properties of photosensitive fiber phase gratings," *J. Lightwave Technol.*, vol. 11, no. 10, pp. 1513-1517, Oct. 1993.

[39] S. J. Mihailov, C. W. Smelser, D. Grobnic, R. B. Walker, P. Lu. H. Ding, and J. Unruh, "Bragg gratings written in all-SiO_2 and Ge-doped core fibers with 800-nm femtosecond radiation and a phase mask," *J. Lightwave Technol.*, vol. 22, no. 1, pp. 94-100, Jan. 2004.

[40] K. O. Hill, B. Malo, F. Bilodeau, D. C. Johnson, and J. Albert, "Bragg gratings fabricated in monomode photosensitive optical fiber by UV exposure through a phase mask," *Applied Physics Letters*, vol. 62, no. 10, pp. 1035-1037, Mar. 1993.

[41] A. Othonos, "Fiber Bragg gratings," *Rev. Sci. Instrum.*, vol. 68, Dec. 1997.

[42] Y. Le Guennec, G. Maury, J. P. Yao, and B. Cabon, "New optical microwave up-conversion solution in radio-over-fiber networks for 60-GHz wireless applications," *J. Lightwave Technol.*, vol. 24, no. 3, pp. 1277-1282, Mar. 2006.

[43] D. Wake, M. Webster, G. Wimpenny, K. Beacham and L. Crawford, "Radio over fiber for mobile communications," *IEEE MWP '04*, pp. 157-160, 2004.

[44] D. Wake, C. R. Lima, and P. A. Davies, "Transmission of 60-GHz signals over 100 km of optical fiber using a dual-mode semiconductor laser source," *IEEE Photon. Technol. Lett.*, vol. 8, no. 4, pp. 578-580, Apr. 1996.

[45] G. Grosskopf, D. Rohde, R. Eggemann, S. Bauer, C. Bornholdt, M. Möhrle, and B. Sartorius, "Optical millimeter-wave generation and wireless data transmission using a dual-mode laser," *IEEE Photon. Technol. Lett.*, vol. 12, no. 12, pp. 1692-1694, Dec. 2000.

[46] D. Wake, C. R. Lima, and P. A. Davies, "Optical generation of millimeter-wave signals for fiber-radio systems using a dual-mode DFB semiconductor laser," *IEEE Trans. Microwave Theory Techn.*, vol. 43, no. 9, pp. 2270-2276, Sept. 1995.

[47] A. C. Bordonalli, C. Walton, and A. J. Seeds, "High-performance phase locking of wide linewidth semiconductor lasers by combined use of optical injection locking and optical phase-lock loop," *J. Lightwave Technol.*, vol. 17, no. 2, pp. 328-342, Feb. 1999.

[48] S. Kobayashi and T. Kimura, "Injection locking in AlGaAs Semiconductor Laser," *IEEE J. Quantum Electron.*, vol. QE-17, no. 5, pp. 681-689, May 1981.

[49] R. Hui, A. Mecozzi, A. D'Ottavi, and P. Spanno, "Injection locking in distributed feedback semiconductor lasers," *IEEE J. Quantum Electron.*, vol. 27, no. 6, pp. 1688–1695, June 1991.

[50] M Ogusu, K. Inagaki, and Y. Mizuguchi, "60 GHz millimeter-wave source using two-mode injection-locking of a Fabry–Perot slave laser," *IEEE Microwave and Wireless Components Lett.*, vol. 11, no. 3, pp. 101-103, March 2001.

[51] L. N. Langley, M. D. Elkin, C. Edge, M. J. Wale, U. Gliese, X. Huang, and A. J. Seeds, "Optical phase locked loop (OPLL) module for use as a 9 GHz source in phased array communications antennas," *IEEE MWP '98*, pp. 141-142, 1998.

[52] U. Gliese, T. N. Nielsen, M. Bruun, E. Lintz Christensen, K. E. Stubkjzr, S. Lindgren, and B. Broberg, "A wideband heterodyne optical phase-locked loop for generation of 3-18 GHz microwave carriers," *IEEE Photon. Technol. Lett.*, vol. 4, no. 8, pp. 936-938, Aug. 1992.

[53] L. N. Langley, M. D. Elkin, C. Edge, M. J. Wale, U. Gliese, X. Huang, and A. J. Seeds, "Packaged semiconductor laser optical phase-locked loop (OPLL) for photonic generation, processing and transmission of microwave signals," *IEEE Trans. Microwave Theory Techn.*, vol. 47, no. 7, pp. 1257-1264, July 1999.

[54] C. Walton, A. C. Bordonalli, and A. J. Seeds, "High-performance heterodyne optical injection phase-lock loop using wide linewidth semiconductor lasers," *IEEE Photon. Technol. Lett.*, vol. 10, no. 3, pp. 427-429, Mar. 1998.

[55] L. A. Johansson and A. J. Seeds, "Millimeter-wave modulated optical signal generation with high spectral purity and wide-locking bandwidth using a fiber-integrated optical injection phase-lock loop," *IEEE Photon. Technol. Lett.*, vol. 12, no. 6, pp. 690-692, June 2000.

[56] L.A. Johansson and A. J. Seeds, "36-GHz 140-Mb/s radio-over-fiber transmission using an optical injection phase-lock loop source," *IEEE Photon. Technol. Lett.*, vol. 13, no. 8, pp. 893-895, Aug. 2001.

[57] R. T. Ramos, P. Gallion, D. Erasme, A. J. Seeds and A. Bordonalli, "Optical injection locking and phase-lock loop combined systems," *Optics Letters*, vol. 19, no. 1, pp. 4-6, Jan. 1994.

[58] L.A. Johansson and A. J. Seeds, "Generation and transmission of millimeter-wave data-modulated optical signals using an optical injection phase-lock loop," *J. Lightwave Technol.*, vol. 21, no. 2, pp. 511-520, Feb. 2003.

[59] R. T. Ramos and A. J. Seeds, "Fast heterodyne optical phase-lock loop using double quantum well laser diodes," *Electron. Lett.*, vol. 28, no. 1, pp. 82-83, Jan. 1992.

[60] R. T. Ramos and A. J. Seeds, "Comparison between first-order and second-order optical phase-lock loops," *IEEE Microwave Guided Wave Lett.*, vol. 4, no. 1, pp. 6-8, Jan. 1994.

[61] M. Kourogi, C. H. Shin, and M. Ohtsu, "A 134 MHz bandwidth homodyne optical phase-locked-loop of semiconductor laser diodes," *IEEE Photon. Technol. Lett.*, vol. 3, no. 3, pp. 270-272, Mar. 1991.

[62] M. S. Goncalves and A. C. Bordonalli, "A theoretical analysis of optical phase-lock loop acquisition and tracking for WDM receiver applications," *Proc. SBMO/IEEE MTT-S Intern. 2003*, vol. 1, pp. 251-256, Sept. 2003.

[63] M. Ohtsu, M. Murata, and M. Kourogi, "FM noise reduction and subkilohertz linewidth of an AlGaAs laser by negative electrical feedback," *J. Quantum Electron.*, vol. 26, no. 2, pp. 231-241, Feb. 1990.

[64] P. G. Goetz, H. Eisele, K. Yang, K. C. Syao, O. Qasaimeh, and P. Bhattacharya, "InP-based MMIC components for an optical phase-locked loop," *IEEE Trans. Microwave Theory Techn.*, vol. 47, no. 7, pp. 1241-1250, July 1999.

[65] A. C. Davidson, F. W. Wise, and R. C. Compton, "Low phase noise 33–40-GHz signal generation using multilaser phase-locked loops," *IEEE Photon. Technol. Lett.*, vol. 10, no. 9, pp. 1304-1306, Sept. 1998.

[66] M. Z. Win, C. C. Chen, and R. A. Scholtz, "Optical phase-locked loop (OPLL) for an amplitude modulated communications link using solid-state lasers," *J. Select. Areas Communications*, vol. 13, no. 3, pp. 569-576, Apr. 1995.

[67] M. Hyodo, K. S. Abedin, N. Onodera, "Generation of millimeter-wave signals up to 70.5 GHz by heterodyning of two extended-cavity semiconductor lasers with an intracavity electro-optic crystal," *Optics Communications, Elsevier Science,* vol. 171, no. 1-3, pp. 159-169, Nov. 1999.

[68] M. Hyodo and M. Watanabe, "Optical generation of millimeter-wave signals up to 330 GHz by means of cascadingly phase locking three semiconductor lasers," *IEEE Photon. Technol. Lett.*, vol. 15, no. 3, pp. 458-460, Mar. 2003.

[69] P. G. Goetz, H. Eisele, K. C. Syao, and P. Bhattacharya, "1.55-mm optical phase-locked loop with integrated p-i-n/HBT photoreceiver in a flexible development platform," *Microwave Optic. Technol. Lett.*, vol. 15, no. 1, pp. 4-7, May 1997.

[70] M. A. Grant, W. C. Michie, and M. J. Fletcher, "The performance of optical phase-locked loops in the presence of nonnegligible loop propagation delay," *IEEE J. Lightwave Technol.*, vol. 5, no. 4, pp. 592-597, Apr. 1987.

[71] M. Hyodo and M. Watanabe, "Optical generation of millimetre-wave signals up to 110GHz by phase-locking of two external-cavity semiconductor lasers," *Electron. Lett.*, vol. 38, no. 25, pp. 1679-1680, Dec. 2002.

[72] A. Yariv, "Dynamic analysis of the semiconductor laser as a current-controlled oscillator in the optical phased-lock loop: applications," *Optics Letters*, vol. 30, no. 17, pp. 2191-2193, Sept. 2005.

[73] F. M. Gardner, "Phaselock Techniques", 3rd ed. Wiley: New Jersey, USA 2005.

[74] D. R. Stephens, "Phase-Locked Loops for Wireless Communications: Digital, Analog and Optical Implementations," 2nd ed. Kluwer Academic Publishers: Massachusetts, USA 2002.

[75] Z.F. Fan and M. Dagenais, "Optical generation of a mHz-linewidth microwave signal using semiconductor lasers and a discriminator-aided phase-locked loop," *IEEE Trans. Microwave Theory Techn.*, vol. 45, no. 8, pp. 1296-1300, Aug. 1997.

[76] Z. F. Fan, P. J. S. Heim, and M. Dagenais, "Highly coherent RF signal generation by heterodyne optical phase locking of external cavity semiconductor lasers," *IEEE Photon. Technol. Lett.*, vol. 10, no. 5, pp. 719-721, May 1998.

[77] J. S. Seregelyi and J. C. Bélisle, "A discriminator-aided, optical phase-lock loop constructed from commercial components," *Proc. SPIE Vol. 5577*, Photonics North 2004, pp. 407-412, 2004.

[78] R. T. Ramos and A. J. Seeds, "Delay, linewidth, and bandwidth limitations in optical phase-locked loop design," *Electron. Lett.*, vol. 26, no. 6, pp. 389-391, March 1990.

[79] E. Detoma, B. Tromborg, and I. Montrosset, "The complex way to laser diode spectra: example of an external cavity laser strong optical feedback," *J. Quantum Electronics*, vol. 41, no. 2, pp. 171-182, Feb. 2005.

[80] A. Godard, G. Pauliat, G. Roosen, P. Graindorge, and P. Martin, "Side-mode gain in grating-tuned extended-cavity semiconductor lasers: investigation of stable single-mode operation conditions," *J. Quantum Electronics*, vol. 38, no. 4, pp. 390-401, Apr. 2002.

[81] G. H. M. van Tartwijk and D. Lenstra, "Semiconductor lasers with optical injection and feedback," *Quantum Semiclass. Opt.*, pp. 87-143, 1995.

[82] H. Rideout, J. S. Seregelyi, S. Paquet, and J. P. Yao, "Discriminator-aided optical phase-lock loop incorporating a frequency down-conversion module," *IEEE Photon. Technol. Lett.*, vol. 18, no. 22, pp. 2344-2346, Nov. 2006.

[83] A. Bononi, P. Ghiggino, and G. Picchi, "Analysis of the automatic frequency control in heterodyne optical receivers," *IEEE J. Lightwave Technol.*, vol. 10, no. 6, pp. 794-803, June 1992.

[84] K2 Optronics, www.k2optronics.com.

[85] N. Sayers, S. Granieri, and A. Siahmakoun, "Fabrication of multiple fiber-Bragg gratings on one SMF using a single phase-mask," *Proc. SPIE Vol. 5970 Photonic Applications in Devices and Communication Systems*, 59701J, 2005.

[86] Qin Zhang, D. A. Brown, L. Reinhart, T. F. Morse, J. Q. Wang, and Gang Xiao, "Tuning Bragg wavelength by writing gratings on prestrained fibers," *IEEE Photon. Technol. Lett.*, vol. 6, no. 7, pp. 839-841, July 1994.

[87] K. Ennser, M. N. Zervas, and R. I. Laming, "Optimization of apodized linearly chirped fiber gratings for optical communications," *IEEE J. Quantum Electron.*, vol. 34, no. 5, pp. 770-778, May 1998.

[88] H. R. Rideout, J. S. Seregelyi, and J. P. Yao, "A true-time delay beamforming system incorporating a wavelength tunable optical phase-lock loop," *IEEE J. Lightwave Technol.*, submitted for publication, Sept. 2006.